ENHANCED MULTIFUNCTIONAL PROPERTIES OF CFRP COMPOSITES FOR LIGHTNING STRIKE PROTECTION

ANCHALEE DUONGTHIPTHEWA

PhD

The Hong Kong Polytechnic University

2021

The Hong Kong Polytechnic University

Department of Mechanical Engineering

Enhanced Multifunctional Properties of CFRP Composites for Lightning Strike Protection

Anchalee Duongthipthewa

A thesis submitted in partial fulfillment of the requirements for
the degree of Doctor of Philosophy

May 2020

CERTIFICATE OF ORIGINALITY

I hereby declare that this thesis is my own work and that, to the best of my knowledge and belief, it reproduces no material previously published or written, nor material that has been accepted for the award of any other degree or diploma, except where due acknowledgment has been made in the text

Anchalee Duongthipthewa

Department of mechanical engineering
The Hong Kong Polytechnic University
Hong Kong, P.R. China

ABSTRACT

Lightning is one of nature's most unpredictable and destructive forces and poses a serious risk to commercial aircraft, which statistically encounter a lightning strike every 1,000 – 10,000 flight hours or approximately once per year. The damage of lightning strikes displays as burnt paint, damaged fiber, removal composite layer in aircraft structures, and degraded or even malfunction of avionic equipment performances. This can severely hinder the airline's operation results in costly delays and service interruptions that are the primary concerns in aircraft structures. Metal sheets are used as primary material in aircraft structures due to their excellent electrical and thermal conductivities, which allow electrical current to travel on the exterior aircraft skin and instantly exit through other extremity points. However, recent developments in aircraft design involving non-metallic skins and lightweight structural concepts have used carbon fiber reinforced polymers (CFRP), which have high orthotropic electrical resistivity and therefore increase aircraft vulnerability to the effects of lightning strikes. A considerable damage could be observed in the low electrical conductivity materials as they have absorbed high electrical energy during lightning strike due to the increase of Joule heating. To develop a new generation of highly conductive carbon composites that address these shortcomings, carbon nanotubes (CNTs) were grown on nickel-coated carbon fiber using chemical vapor deposition (CVD) method at low-temperature growth to create a fuzzy fiber (FF). An additional conductive filler, graphene nanoplatelets (GNPs), was then dispersed on the fuzzy fiber surface to form synergistic physical interactions between two different low-dimensional carbon-based nanostructures. Specimens were fabricated by integrating the FF layer with and without GNPs to the outermost ply of the CFRP composite using vacuum-assisted resin transfer molding (VARTM) method or wet lay-up process with the autoclaved curing. The results reveal a synergistic enhancement in both functional conductivity and mechanical properties. The electrical conductivity of composites with the inclusion of GNPs resulted in approximately 40%, 300%, and 190% enhancement in the fiber, surface, and through-thickness direction compared to the fuzzy fiber composites. Mechanical properties, including flexural, impact, and interlaminar shear stress properties were further enhanced. These results reveal that the presence of GNPs creates more electron transfer pathways, and also promotes a synergistic effect in physical interactions. Altogether, these enhancements provide avenues for future high-performance conductive carbon fiber composites in aircraft structures.

Then, a three-dimensional thermal-electrical coupled model based on COMSOL was created to characterize the thermal damage propagation modes in woven CFRP composite with and without an LSP system. FF serving as a carbon-based protection layer was attached to the outermost ply of the CFRP composite to fabricate a fuzzy fiber reinforced polymer (FFRP) composite. CFRP and FFRP composites with temperature-dependent properties were inspected to predict lightning-induced damage resulting from a 20- and 40-kA peak current for 100 μs. The predicted area of thermal damage and the appearance of the composite surface agreed fairly well with post-lightning damage observed from experiments, thus demonstrating the credibility of the numerical model. LSP characteristics were evaluated for a range of CFRP composite properties in the outermost layer by enhancing the functional conductivity of the top layer in the in-plane and out-of-plane directions. The irreversible thermal damage region in the in-plane and thickness directions was dramatically mitigated by enhanced electrical conductivity, whereas a slight reduction of matrix decomposition damage was observed by varying the thermal conductivity. Due to the increased functional conductivity and integration of the lightweight FF carbon-based protection layer into the uppermost composite layer, the depth and area of damage can be limited by decreasing the thermal damage penetration through the underlying composites. These results reveal that a highly conductive FF layer may serve as a lightweight and effective anti-lightning strike layer for protecting the underlying composite.

PUBLICATIONS ARISING FROM THE THESIS

Journal papers

Duongthipthewa A., Su Y., and Zhou L.*, Electrical conductivity and mechanical property improvement by low-temperature carbon nanotube growth on carbon fiber fabric with nanofiller incorporation, **Composites Part B: Engineering**. 2020:107581.

Duongthipthewa A., Lu M., Du K., Ye L., and Zhou L.*, Experimental and Numerical Simulation of Lightning Damage Development on Composites with/without a Carbon-Based Protection Layer. – **Composite Structures**, 2020, accepted.

Duongthipthewa A. and Zhou L.*, Modeling lightning-induced damage development in CFRP composites with/without metal or carbon-based protection layer. – **Submitted to Composites Part B: Engineering**

Conference proceedings

Duongthipthewa A., Su Y., and Zhou L.*, "Carbon Fiber Composites with Multi-Nanofillers for Lightning Strike Protection", The 21st International Conference on Composite Materials (ICCM-21), Xi'an, China, 2017.

Duongthipthewa A., Su Y., and Zhou L.*, "Enhanced Multi-Functional Properties of Carbon Fiber Composites against Lightning Strike", The 7th East Asia Mechanical and Aerospace Engineering (EAMAE) Workshop, Sapporo, Japan, 2017.

Duongthipthewa A., Su Y., Zhou L.*, “Improved Structural and Functional Properties of Carbon Fiber Composites for Lightning Strike Protection”, The 18th European conference on composite materials (ECCM18), Athens, Greece, 2018.

Duongthipthewa A. and Zhou L.*, “Enhanced Functional and Mechanical Properties of Carbon Fiber Composites for Lightning Strike Protection”, Strategic Partnership Forum, Tainan, Taiwan, 2018.

Duongthipthewa A. and Zhou L.*, “Multifunctional Composites with Modified Carbon Fibers for Lightning Strike Protection”, The 22nd International Conference on Composite Materials (ICCM-22) Melbourne, Australia, 2019.

ACKNOWLEDGMENTS

I sincerely thanks my supervisor, Prof. Zhou Limin who provide great facilities and vital guidance throughout the year and support from the initial to the final stage enabled me to research and develop this thesis.

I am very grateful for the support received from the Hong Kong Polytechnic University (grants G-YBLF, 1-ZVJD, and 1-ZVGH) and the Hong Kong Research Grants Council via a Hong Kong Ph.D. Fellowship Fund (grant: 1-904Z) for offering me the opportunity to further my study in the Doctor of Philosophy in Engineering program. I would like to express my appreciation to the Department of Mechanical Engineering (ME) for adequate materials and laboratory equipment provided that greatly facilitate my research work.

Sincere thanks to Mr. Su Yiyin, who provided me with his great help. I also would like to thanks Dr. Hardy Lui, Dr. Terence Wong, Dr. Wei Lu, Dr. Chan Ngai Yui, and Ms. Ho Wing Man for their assistance and advice gave throughout my experiment in the laboratory.

Last but not least, I would like to greatest gratitude to my parents (Mr. Somsak and Mrs. Rutsamee Duongthipthewa) and my sister (Ms. Onjira Duongthipthewa) for their endless love, encouragement and numerous support that keep me forward to accomplish this study throughout all these years.

Lastly, I offer my regards and blessing to all of those who supported me in any respect during the completion of the project.

TABLE OF CONTENTS

LIST OF FIGURES

LIST OF TABLES

ABBREVIATIONS

Ar	Argon
ASTM	American Society for Testing and Materials
C	Carbon
CB	Complete break
CF	Carbon fiber
CFRP	Carbon fiber reinforced polymer
CH_4	Methane
CNTs	Carbon nanotubes
Co	Cobalt
CO	Carbon monoxide
CO_2	Carbon dioxide
Cu	Copper
CVD	Chemical vapor deposition
DCM	Dichloromethane
DGEBA	Diglycidyl ether of bisphenol-A
DWNTs	Double-wall carbon nanotubes
E	Electric
EM	Electromagnetic
EMA	Effective medium approach

EMF	Electromagnetic field
EMI	Electromagnetic interference
EMI SE	Electromagnetic interference shielding effectiveness
Fe	Iron
FEA	Finite element analysis
FESEM	Field emission scanning electron microscopy
FF	Fuzzy fiber
FFRP	Fuzzy fiber reinforced polymer
GNPs	Graphene nanoplatelets
GO	Graphene oxide
H_2	Hydrogen
H_2SO_4	Sulfuric acid
He	Helium
HB	Hinge break
HNO_3	Nitric acid
IPA	Isopropyl alcohol
$KMnO_4$	Potassium permanganate
LA	Longitudinal Mode
LCM	Liquid composite molding
LSP	Lightning strike protection
MFP	Mean free path
MWNTs	Multi-walled carbon nanotubes

N_2	Nitrogen
NB	Non-break
NH_3	Ammonia
Ni	Nickel
PAN	Polyacrylonitrile
PEEK	Polyetheretherketone
Pt	Platinum
PB	Partial break
PMMA	Poly(Methyl methacrylate)
RTM	Resin transfer molding
RGO	Reduce graphene oxide
SWNTs	Single-walled carbon nanotubes
TA	In-plane transverse mode
TEM	Transmission electron microscopy
TGA	Thermogravimetric analysis
TiO_2	Titania
UTS	Ultimate tensile strength
VARTM	Vacuum-assisted resin transfer molding
ZA	Out-of-plane transverse mode

NOMENCLATURES

b	Specimen width
C_p	Specific heat
D	Diffusion coefficient
d_{MW}	Mass density of MWNTs
d_{out}	Outer diameter
e	Permanent increase in depth of penetration due to major load F_1 measured in units of 0.002 mm
E	A constant depending on the form of indenter: 130 units for steel ball indenter
E'	Elastic modulus
E''	Loss modulus
E_B	Flexural modulus
f	Volume fraction of the fillers
f_c	Percolation threshold
E	Electrical field intensity
F_0	Preliminary minor load
F_1	Additional major load
h	Specimen thickness
$\bar{h}_{\omega}$	Heat capacity

H_I	Magnetic field intensity of the incident wave
H_T	Magnetic field intensity of the transmitted wave
I_0	Current constant
$\mathrm{I_D}$	Intensity of defect
$\mathrm{I_G}$	Intensity of graphite
J	Electrical current density (current per unit area)
k	Thermal conductivity
K_e	Electronic contribution
K_{zz}	Diagonal of the thermal conductivity tensor
L	Span length
L_o	Lorenz number
m	The slope of *the* tangent gradient of the initial straight line of the load-deflection curve
M_m	Maximum moisture absorption
n	Number of walls
ρ	Density
P	Maximum Load (N)
P_I	Power of Incident
P_T	Power of Transmitted Wave
$\rho(\omega)$	Phonon Density Of States
P_{ec}	Electrical energy
q	Heat flux per unity area

r	Heat generated within the body
r_c	Internal volumetric current source per unit volume
t	Time duration
t_1	Front time
t_2	Tail time
T	Temperature
U	Internal energy
V_{MW}	Volume of a CNT
W_{MW}	Weight of MWNTs
W	Impact Energy (J)
α	A reciprocal value of wave tail time constant
β	A reciprocal value of wavefront time constant
σ	Electrical conductivity
σ_f	Flexural strength
π	Pi
τ	Phonon relaxation time
φ	Electrical potential

CHAPTER 1

GENERAL INTRODUCTION

1.1 Background of composite materials and nanomaterials in aircraft structures

The invention of advanced composite materials has introduced a new era in aerospace industries. Carbon fiber reinforced polymer (CFRP) composites have been extensively used as primary structures in various industrial applications such as in infrastructure and the automotive and aerospace industries, due to outstanding properties such as high strength and stiffness at low weight, greater resistance to corrosion, and lower maintenance cost [1,2]. One significant factor of laminates is the diversity of structural properties that can be specifically customized to specific applications. The major constituents of composite fabrication are fiber reinforcements and polymer matrix. They typically combine polymer with fibrous reinforcing dispersed in the matrix phase. The fiber reinforcements provide high strength, while the matrix carries the fiber reinforcement into their positions and protects fibers from brittleness or breakage [3]. Material strength and resistance in the same cross-sectional area of composite have superior compressibility combined with tensile strength providing great versatility suitable for numerous applications. The volume fraction of carbon fiber can tailor the strength and rigidity in composite to offer the specific property for different applications, especially in aircraft structure such as fan blades in jet engine, and control surfaces in the airframe. The future composite market trend of commercial aircrafts has been growing because of fuel efficiency improvement, weight reduction, safety performance enhancement, and other performance benefits over traditional materials as shown in Figure 1-1 and Figure 1-2.

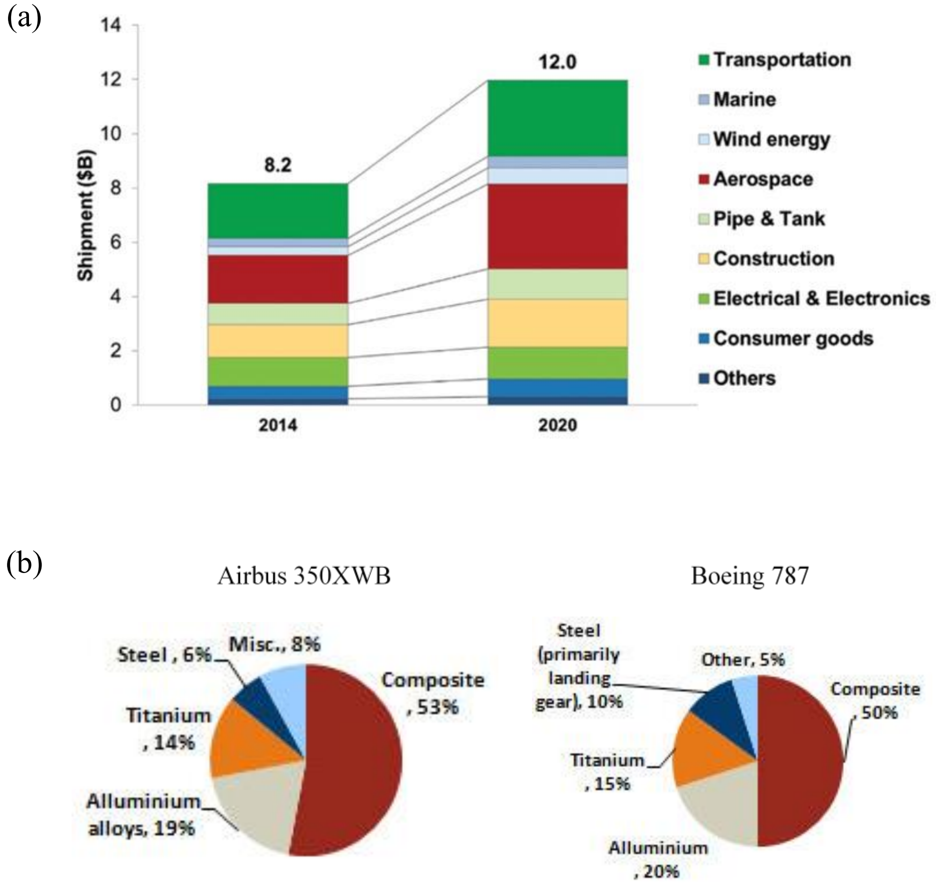

Figure 1-1. Trend of using composite materials in aircraft of the (a) US composite market forecast by application segment [4] and (b) proportion of composite [5].

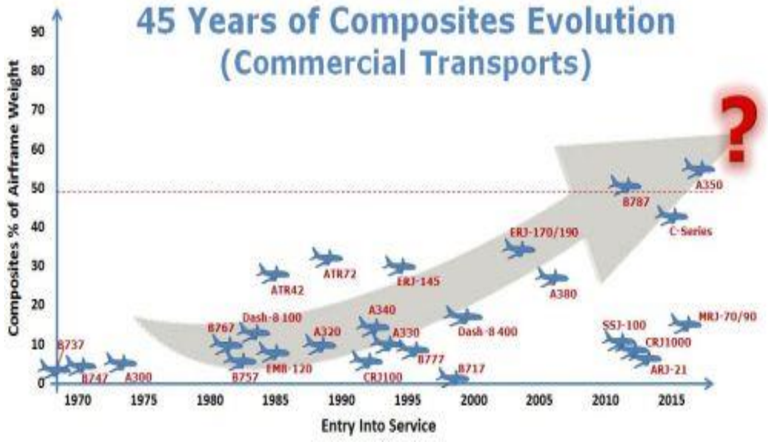

Figure 1-2. The evolution of composites in aircraft [6].

The replacement of traditional metal materials with composites, on the other hand, has shown some major challenges due to the lack of functional conductivity. The in-plane electrical conductivity in the composite is higher than their out-of-plane characteristics as the interface between lamellae is relatively rich in matrix polymer, but their applications are still limited. Increasing their electrical conductivity together with structural properties presents a real challenge because both efficient electron transfer in isolating bulk matrix and load transfer between fibers and matrix are required. Conductive carbon fiber composites that feature this combination of properties can further extend their applications in electromagnetic shielding, structure health monitoring, and lightning strike protection [7-9].

Lightning is commonly triggered in the atmosphere due to the heavily charged particles in the clouds that each commercial aircraft is generally struck more than once a year. The lightning strike can induce severe damage to aircraft structures such as burnt paint, damaged fiber, removal composite layer, jammed sensitive navigation, and degraded or even malfunction of avionic equipment performances due to the electromagnetic (EM) waves. Due to the high functional conductivity, a conductive metallic mesh or foil bonded at the surface of the component, made of aluminum or copper, is used to mitigate lightning damage and protect the underlying load bearing CFRP composite. This metallic mesh acts as a lightning strike protection (LSP) layer that can discharge lightning current away from critical regions, shield against EM waves, and also improve heat management in the critical heat buildup regions. However, an initial ideal of lightweight property has to be sacrificed.

Due to recent advancements in nanotechnology, there is now an opportunity for significant improvement in material and functional properties through the use of nanomaterials [10]. One of the impacts is the possibility of introducing composite materials into new applications. Carbon nanotubes (CNTs) and graphene nanoplatelets (GNPs) have excellent mechanical, electrical, and magnetic properties that offer strengths at least 100 times that of steel at a much lighter weight [11-14]. The strong carbon bonding, C-C of both carbon-based nanomaterials offer property improvement such as excellent strength and modulus, high functional conductivities, and high electromagnetic interference shielding effectiveness (EMI SE) compared to metals. Due to the high aspect ratio of CNTs and GNPs, they can form physical networks throughout the structure creating conductive pathways. They could also generate strong mechanical interfacial interlocking properties between fillers and matrix [15,16]. However, the challenge of fabricating nanopolymers with different geometric aspect ratios and filler concentration, dispersion quality, and matrix-filler interfacial interaction can influence the sufficiency and effectiveness of electron transport and heat transfer mechanisms. Hence, growing CNTs on fiber surfaces can overcome the fundamental problem of non-uniform dispersion, agglomeration of CNTs, and the increase of matrix viscosity in the direct mixing method. Other challenges such as nanotube alignment, CNT graphitization, morphology control, and poor matrix infusion capability during the infusion process [17-21] should be considered carefully. The quality of CNTs depends on many parameters such as growth duration and thickness of catalyst [22], feed gas composition [23], feed gas flow rate, carrier gas, catalyst precursor composition, and growth temperature [24].

Reducing the process temperature of CNT growth or combining a small percentage of exclusive GNP structure can improve electrical conductivity and also retain mechanical stiffness [25,26]. Indeed, GNPs have extraordinary physicochemical properties and great potential to improve polymer matrix phase properties at very small amounts. These performance improvements include matrix-dominated properties such as flexural and interlaminar shear strength. Enhancing these properties is nontrivial considering that their failure can lead to a catastrophic breakdown in the composite structure due to weak fiber-matrix interfaces and the brittleness of polymer matrix [27].

1.2 Motivation

The usage of composite materials in primary structures has been increasing in aircraft industries over these three decades. CFRP composites have a great mechanical performance with lightweight compared to traditional metal materials. However, functional properties including thermal and electrical conductivities in both the in-plane and out-of-plane directions are a primary concern in LSP applications due to the aircraft safety consideration. In the United States, a commercial aircraft is struck by lightning strikes more than once per year. Lightning can cause severe damages to aircraft structure when it flies through a densely charged area in the clouds. In 1967, the last confirmed commercial plane crash ascribed to lightning results in a catastrophic explosion of fuel tanks [28]. Due to advanced technology, the use of electronic equipment has dramatically expanded causing many unwanted signals. These internal sources of electromagnetic interference (EMI) are dangerous to avionics because EMI could interfere and degrade the performance of electronic devices in aircraft. High power EMI of external sources such as lightning can potentially disrupt aircraft navigation, communication systems, and the loss of aircraft and life. This is because lightning can cause differences in electrical potential and magnetic fields in the aircraft structure inducing transient voltages. These can damage or destroy onboard electronics that have not been protected by an electromagnetic field (EMF).

Several studies have been explored on CFRP composite with and without a metallic LSP layer. These metal meshes or foils are the state-of-the-art material structure placing on the outermost ply of the composite structure. They are satisfactory for electrical and thermal conductivity advancement, however, significant weight increasing, higher galvanic corrosion risk, and problematic repair and maintenance are considerable challenges.

Table 1-1. Mechanical and functional properties of nanomaterials at room temperature [29-37].

Material	Tensile Strength (GPa)	Thermal Conductivity (W/mK)	Electrical Conductivity (S/m)
Nanosized Steel	1.8	5-6	1.35 x 106
SWNT	50-500	3,000-6,000	1x10^{5}-1x10^{6}
MWNT	10-150		5x10^{4}-1x10^{6}
Graphene	120-140	4,840-5,300	1x10^{5}-1x10^{8}
Plastic (HDPE)	0.018-0.02	0.46-0.52	Insulator
Natural rubber	0.020-0.03	0.13-0.142	Insulator
Kevlar	3.6	0.04	Insulator
Silver	0.11-0.34	427	63.0 x 10^{6}
Copper	0.22	401	59.6 x 10^{6}
Aluminum	0.09	237	37.8 x 10^{6}

The evolution of composites, which has become the substitute material for traditional materials, has once again opened up new LSP systems. Due to the current innovation and unique features of nano-materials, many researchers have developed directions of cognitive and applied works on nanocomposite materials. The advantages of nano-filler in the composite are the improvement in mechanical and multi-functional properties introducing composite materials into new applications. The tensile strength and functional conductivities of various nano-additives can be observed in Table 1-1. The reinforced nano-fillers in CFRP composite has anticipated improving the structural property, mechanical property, and functional conductivity in CFRP composites. The incorporation of GNPs on the CNTs grown on carbon fiber surfaces could increase functional conductivity and mechanical properties together with a lightweight structure. These promising nanomaterials can be used in the composite to establish the next generation of carbon-based anti-lightning systems for aircraft structure.

1.3 Problem statement

Conventional CFRP composites have excellent mechanical properties and lightweight but have relatively lack of functional properties caused by the encapsulating insulating polymer matrix in the thickness direction. The CFRP composite is inherently orthotropic materials. The mechanical and functional properties in the in-plane direction are much higher than those in the thickness direction. Even though the functional properties along the in-plane direction are much better than those of the out-of-plane direction, it still limits to numerous applications. The impact of lightning and EMI, therefore, are the major concerns in a new generation of composite aircraft structures. The last confirmed commercial aircraft crashed by lightning in the United States resulted in a catastrophic fuel tank explosion in 1967. Many researchers have been thenceforth studied on the effect of lightning-induced damage in aircraft to improve protection techniques and to verify the safety of their designs. In order to stand with the high lightning current, aluminum or copper mesh is currently used as the LSP system on the upper surface of the CFRP composite. These metallic layers introduce manufacturing and repair difficulties faced by many challenges such as weight increase, galvanic corrosion, and weakening the structures. Based on the aforementioned reasons, an alternative carbon-based LSP layer is developed to enable the removal of metal mesh or foil out of composite encountering lightning strike issues.

1.4 Research objectives

The objective of this study is to design an optimized conductive LSP system on a composite aircraft structure that is able to stand for lightning impact. A metallic mesh or foil is located on the outermost layer of the composite structure to challenge with lightning strikes. This method of bonding metal mesh brings an additional weight that counterbalances the initial idea of employing composites to reduce the weight of aircraft. Besides, galvanic corrosions are another issue that can occur in composite structures due to the flow of electrons in the presence of an electrolyte. This work demonstrates the potential solutions of carbon-based LSP layer integrated at the surface of composite components that could meet regulations and guidelines yet remain lightweight. To fabricate carbon-based LSP layer, CNTs were directly grown on the carbon fiber fabric, followed by GNPs incorporation on the CNTs grown carbon fiber.

CNTs and GNPs, which have excellent mechanical and functional properties, are used as nano-reinforcements in this study. They do not only provide a comprehensive solution to lightning strikes but also to the EMI effect. The EM wave signals can be reflected outright minimized entry points rather than absorbing and dissipating the signal through the skin of composite and grounding the aircraft. Considering the recent limited knowledge of

CNT and GNP implementation, the objectives of this thesis are listed as follows, focusing on the improvement of multi-functional conductivities and mechanical properties to fabricate the conductive carbon-based LSP systems.

- To obtain engineering knowledge about the effect of different parameters for growing CNTs on carbon fiber fabric using floating catalyst chemical vapor deposition (CVD) method at the low-temperature environment

- To demonstrate the effect of CNT and GNP nanofillers in mechanical and functional properties, including flexural properties, inter-laminar shear strength, impact toughness, electrical conductivity, and thermal conductivity

- To investigate matrix decomposition under different LSP functional property effects by improving functional conductivities in the outermost ply of composites

- To understand the thermal damage response on a woven CFRP composite with and without an LSP system using experimental and numerical analysis

- To create a new generation of conductive LSP layer mitigating thermal damage of the underlying CFRP composite serves as an effective lightweight anti-lightning strike structure for metallic meshes or foils replacement

1.5 Outline of the thesis structure

Chapter 1 provides general information on composite materials, lightning strike effects on composite aircraft structures, and brief information on nanomaterials. The problem statement and objective of the study are clarified.

Chapter 2 explains more particular information regarding the entire research. The principle of lightning strikes, LSP systems, composite materials, and nanocomposites are explained. In more detail, the CFRP composite fabrication process and synthesis method of CNTs on carbon fiber fabric are drawn from various published works.

Chapter 3 consists of information regarding the materials used in the synthesis process of CNTs. The parametric study of CNTs grown on the carbon fiber surface, including carbon sources, catalysts, thickness of nickel (Ni) film, carbon source enhancer, temperature, carrier gas flow rate, and sample position are inspected to acquire the optimum CNT growth. Then, the morphological characterization and quality of CNTs are investigated using Scanning Electron Microscopy (SEM), Transmission Electron Microscopy (TEM), Thermogravimetric analysis (TGA), and Raman spectroscopy.

Chapter 4 presents the preparation process of a modified GNPs/epoxy and CFRP composite fabrication technique (Vacuum-Assisted Resin Transfer Molding (VARTM) and wet lay-up method). The characterization of composites is demonstrated using TGA so the fiber volume fraction of CFRP and FFRP composites can be calculated.

Chapter 5 reports the finding of mechanical and functional properties in this study. The effect of the integrated FF layer with and without GNPs in the outermost ply of CFRP composite in terms of mechanical properties, electrical conductivity, and thermal conductivity is investigated to access the properties of the LSP system.

Chapter 6 displays the lightning-induced damage response of unprotected and FFRP composites in both experimental and numerical analysis. The matrix decomposition under different LSP functional property effects in the outermost ply of CFRP composites is investigated to better understand the thermal damage mechanism.

Chapter 7 concludes the remarkable information on the synthesis method of CNTs, fabricating process, mechanical and functional properties, and lightning-induced damage mechanism on composite with and without LSP systems using experimental and numerical analysis together with some suggestions for future research.

CHAPTER 2

LITERATURE REVIEW

2.1 Lightning strikes

A lightning strike, which is one of the most powerful forces by nature, is a secondary effect of electrification of the thundercloud system. According to the Royal Canadian Air Force publication, an aircraft is generally struck by lightning every 1,000 to 3,000 flight hours on average. It is equivalent to one lightning strike for each commercial aircraft annually [38]. Each strike has a great electrical spark with a maximum current flow of 200 kA. Immediate heating of the air results in thunder producing a high temperature in its. Due to the current transportation on the external aircraft skin, the temperature may suddenly increase up to around 20,000 °C, which is about three times higher than the temperature on the surface of the Sun.

2.1.1 Principles of lightning strike protection (LSP)

An LSP system is a structure designed to mitigate lightning-induced damage and to protect the composite structure underneath. Lightning flashes are generated from cloud charged particles in the charge center, especially in cumulonimbus clouds, and also other atmospheric conditions. The cloud charges are constructed wherever there is adequate upward motion, instability in the vertical, and moisture in order to generate a deep cloud that reaches up to freezing and melting levels. Most positively charged particles are accumulated in the top of cumulonimbus clouds, while the base of cumulonimbus clouds primarily contains negative-charged and some positive-charged particles. Electrical fields can be created by both positive and negative charged particles in the cumulonimbus cloud forming electrical charges. The electric fields radiated by the lightning flashes would present in the ionosphere

There are four types of current flow, which are cloud to ground, cloud to cloud, intracloud, and ground to cloud. A flash of cloud to ground originates in the cloud and propagates to the ground with numerous individual strokes separated by a tenth of a second. A cloud-to-cloud strike is not promptly visible from the ground, however, diffusely illuminates the cloud because it flashes between opposite polarities in different clouds. It can also be from the cloud through an aircraft operating in the vicinity that is called intracloud discharge. Intra-cloud strike flashes between opposite polarities within a cloud. It is one of the most critical cases because most of the aircraft will be experienced these subsequent lightning strikes inside the cloud. The positive current of the return stroke, on the other hand, travels from the ground to the cloud. Lightning usually strikes at the nose, wingtip, and other extremities of the aircraft. The lightning current always flows through the most conductive pathway and the shortest route conceivable in its electrical circuit and exit from another extremity. Aircraft can be triggered by lightning strikes when they have flown through a heavily charged location in the cloud. The electrical discharge then moves along the aircraft which is being swept along for a short distance displayed the Hang-on phenomenon. This phenomenon occurs when a high current flows through an attachment point of composite structures. This is because lightning flash is originally at the aircraft and extends away in the opposite direction. Most of the small or private aircraft have less statistically struck by lightning because they normally avoid unacceptable weather.

Aircraft with improper protection could confront severe suffering consequences because high electrical current always travels toward the lowest resistance part of the composite structure. Thus, the bonding with low electrical connection resistance in aircraft components and the main airframe is needed providing sufficient protection to be able to withstand high lightning current. There are three different categories to separate lightning flash which are [39]:

1. Return stroke with maximum currents up to 200 kA and duration on the order of tens of microseconds.

2. Intermediate currents up to 10 kA or more and duration on the order of milliseconds.

3. Continuing currents up to 1 kA and duration on the order of hundreds of milliseconds.

Return stroke surges with peak currents mostly produce indirect effects and explosives, while, intermediate current (component B) and continuing current (component C) are originally liable for direct damage such as skin burning. Currents are also associated with subsequent return strokes that are characterized by rapid rates of change. According to the SAE Report AE4L-97-4 [40,41], the current waveforms with a severe lightning strike situation can be observed in Figure 2-1.

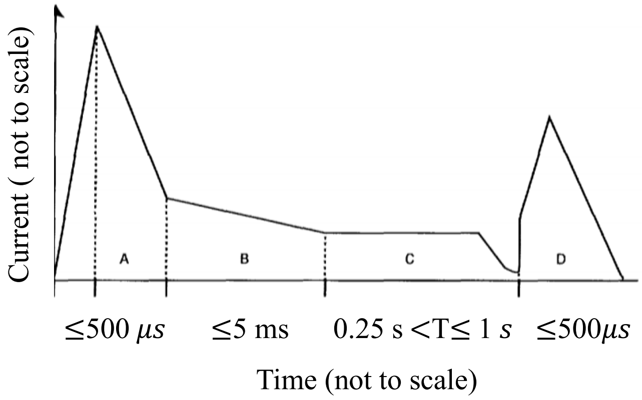

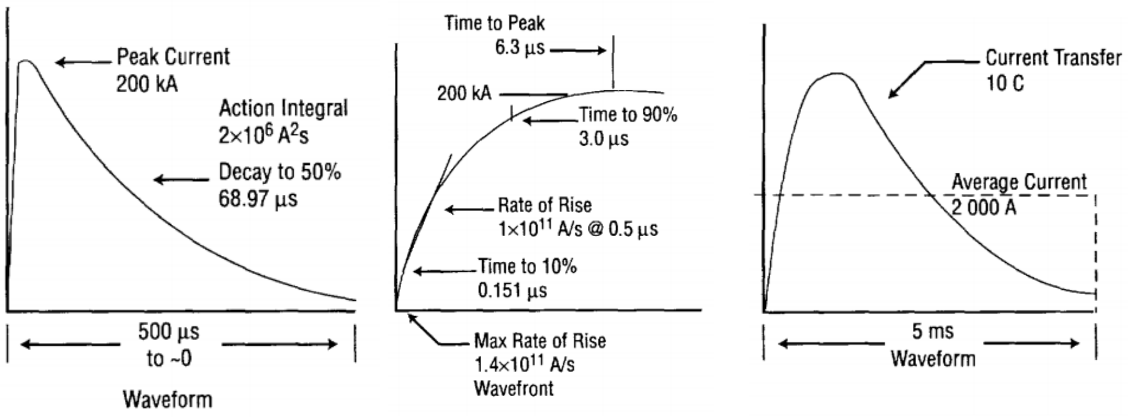

Component A **Component B**

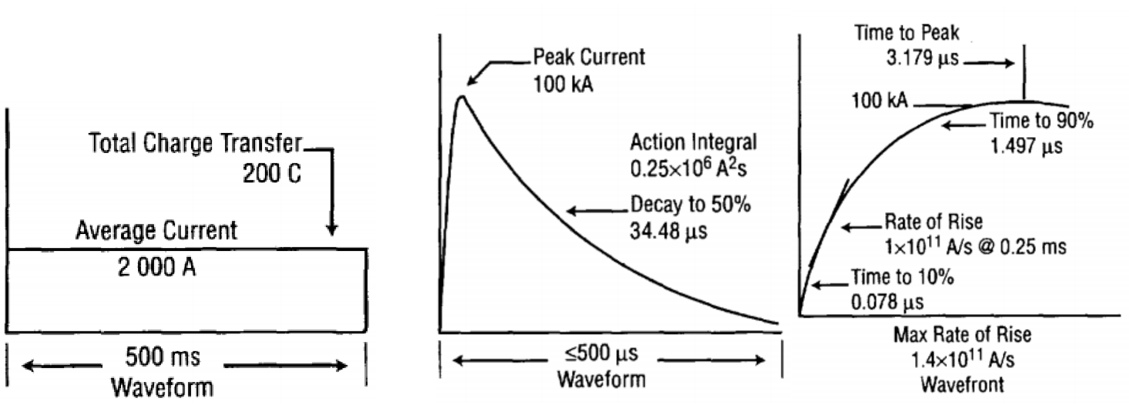

Component C **Component D**

Figure 2-1. Current waveform with a severe direct lightning strike.

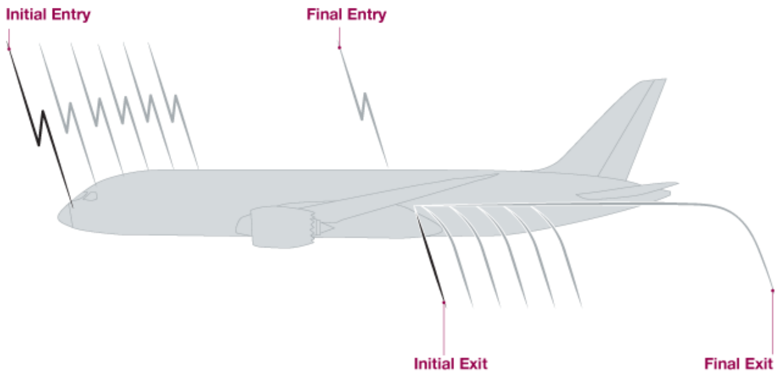

Figure 2-2. Location of lighting traces on an aircraft.

A lightning strike is initially attached to an aircraft extremity at one location and exits from another spot, as shown in Figure 2-2. Both entrance and exit points in the aircraft can be damaged by a lightning strike. Damages like pits, small holes, burn marks, and discolored skin can be observed in the metallic aircraft structures. These small holes can be grouped in one region or separated in a large region because the entry spot will shift when the charge re-attaches to different spots aft of the initial location results in multiple burn areas. On the other hand, lighting-induced damage can also be presented in the form of paint burnt, damaged fibers, and removal layer in the composite aircraft structures in the aircraft with improper protection systems.

2.1.2 Aircraft lightning strike damages

Figure 2-3 shows lightning-induced damages on composite structures. Pitting, burnt sign around fasteners, decomposition, resistive heating, and missing aircraft component at the extremities like a vertical stabilizer horizontal stabilizer edges, and wingtips are classified as the direct damage. Moreover, the high-intensity current can also damage aircraft avionic systems, generators, power feeders, and electrically controlled mechanisms. Due to the effect of the magnetic field and electrical potential differences, transient voltage spikes can be affected. A bonding strap from high electromagnetic forces shows as an indication of damage. Once high lightning current flow in the aircraft structure, many aircraft components made of ferromagnetic materials can cause magnetization.

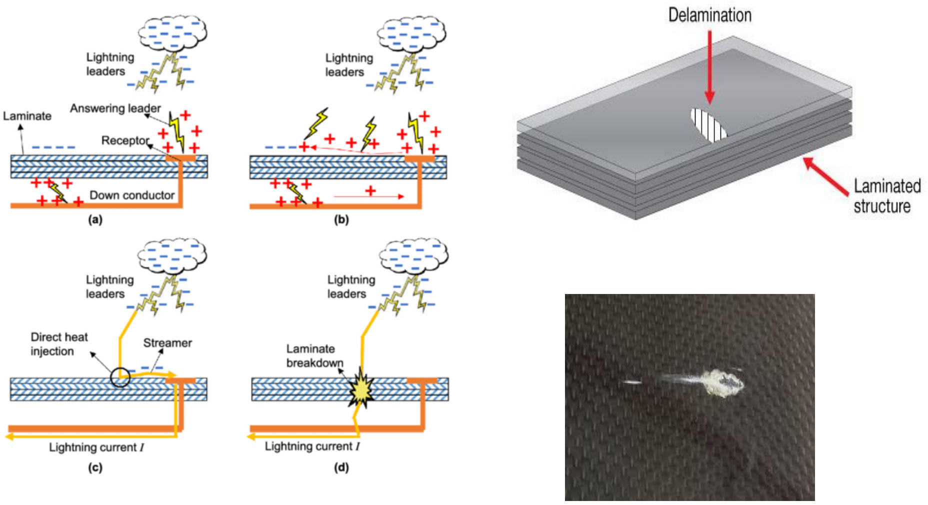

Figure 2-3. Lightning-induced damages [42].

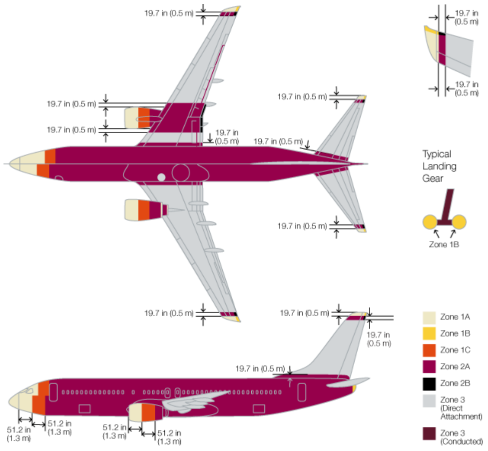

Figure 2-4. Aircraft lightning strike zones.

All aircraft surfaces can be classified into zones to illustrate the frequency and intensity of lightning strike impact. The varied sensitivity and vulnerability in each zone demonstrate different lightning damages in aircraft structures. The aircraft lightning zones and definition can be observed in Figure 2-4 and Table 2-1.

Table 2-1. Definition of aircraft lightning zones.

Zone Designation	**Description**	**Definition**
1A	First and return stroke zone (Initial attach)	All aircraft surface areas where are attached by the first return stroke during lightning strike with a low expectation of flash hang on.
1B	First return stroke zone with a long hang on (Discharge Region)	All aircraft surface areas where are attached by the first return stroke during lightning strike with a high expectation of flash hang on.
1C	Transition zone for the first return stroke	All aircraft surface areas where are attached by the first return stroke of reduced amplitude during lightning strike with a low expectation of flash hang on.
2A	Swept stroke zone	All aircraft surface areas where are swept by subsequent return stroke with a low expectation of flash hang on.
2B	Swept stroke zone with long hang on (Discharge Region)	All aircraft surface areas where are swept by subsequent return stroke with a high expectation of flash hang on.
3	Current conduct region with a low possibility of lightning strike attachment	Surfaces where are not included in Zone 1A, 1B, 1C, 2A, or 2B.

Zone 1 represents a zone that prone to be affected by the initial lightning attachment (entrance and exit points). Zone 2 indicates the moving, swept, or attachment components. Zone 3 shows areas where mostly experience conducted currents with any actual attachment of lightning strikes. The external components that prone to be attached are radome, nacelles, elevators, horizontal stabilizer tips, wingtips, vertical fin tips, ends of the leading edge flaps, trailing edge flap track fairings, landing gear, and air data sensors.

2.1.3 LSP systems

Metals were used as a primary material in aircraft structures for a long time because of their excellent electrical and thermal conductivities that can reduce severe damage to aircraft structural components. It is also permitted high-frequency electromagnetic waves through aircraft structures without any interference at the same time. However, the increased usage of CFRP composite materials in aircraft structure enhances aircraft vulnerability to the effects of lightning strikes because of the low electrical and thermal conductivity, especially in the thickness direction. Carbon fibers are conductive entities, while the polymer acts as an insulator in the composite. Polymer matrix in the composite can be vaporized at a high energy density concentration area due to the low functional conductivity. They do possess entry and exit locations with current propagation like metals, but their composite conductivity is not homogenous as metal materials. It also has a problem with inter-ply and intra-ply arcing. This inter-ply arcing is occurred when current travels from ply-to-ply fibers. Even though composites have many great structural property benefits, they do not protect the interior inside the aircraft as efficiently as metals.

The metal aircraft structures can increase reliance on the digital flight control electronics against analog and mechanical systems. Hence, the lightning impact has become a considerable challenge due to the lack of functional conductivities in CFRP composite materials. The enhance of electrical and thermal conductivities on the exterior of aircraft structures can improve the energy spike diffusion rate by increase conductive paths for electron transportation.

The function of the LSP systems is to conduct instantaneously the electric charge away from the lightning attachment region mitigating thermal damage in the composite underneath from the effect of Joule heating and heat conduction. Thus, metallic meshes or foils are used as LSP systems bounding on the uppermost ply of composite aircraft structure as shown in Figure 2-5. The metallic LSP layer increases conductive paths solving the spurious signals-induced issue, thus reducing electronic processing equipment interference. The metal LSP systems are primarily made of copper and aluminum. Aluminum is one of the best choices for LSP applications due to its lightweight, however, the galvanic corrosion risk in contact with carbon fiber is a serious concern. An isolation ply of fiberglass and copper mesh can solve the galvanic corrosion issues but also adds weight to the structure. Therefore, other LSP systems are considered to challenge weight addition and galvanic corrosion problems that can degrade composites.

Many studies have been explored new multifunctional approaches, including conductive paint and low resistance laminates. A nickel-coated carbon fiber composite is another material to counteract the parasitic weight, eliminate galvanic corrosion problems, and shorten the manufacturing steps [43]. At the current stage, nanoscience has prospered and increased the significance of nanotechnology as miniaturization becomes more considerable in many fields such as aerospace and automobile, computing, MEMs and sensors, biomedical materials. Nanomaterials can be applied in many applications, which depend on their structural features and mechanical properties. Hence, scientists and engineers are required to improve material properties to suit each application. Innovative nano-materials are introduced in the composite to enhance mechanical and functional properties. However, the dispersion quality of nano-reinforcements can affect the interfacial interaction of filler-matrix or filler-filler. Homogeneous fillers distribution with high mass or volume fraction of nano-reinforcement can improve adhesion interaction between fillers and matrix producing a strong hybrid polymer composite, results in better material performances [44].

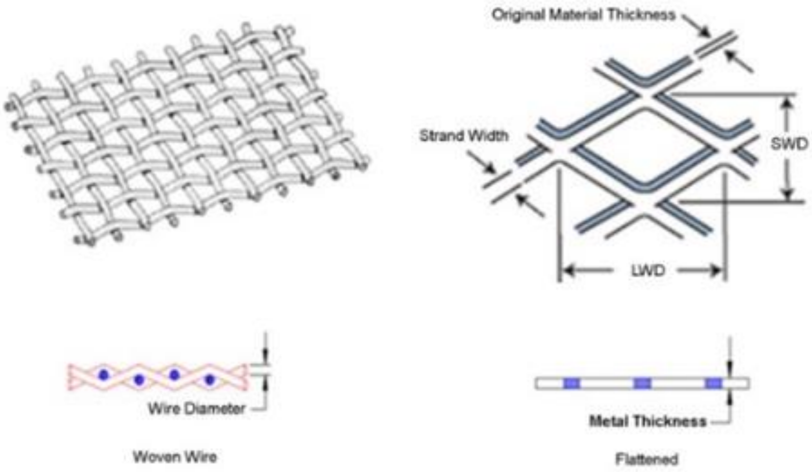

Figure 2-5. Metal mesh integrated on the uppermost ply of the composite.

2.2 Composite materials

In the 1960s, advanced composites are discovered in the form of reinforced carbon fiber and resin matrix composite [45]. Composite consists of at least two independent constituents with notably different mechanical properties that remain separate and distinct within their finished structures. The composite is composed of constituent materials that include reinforcement and matrix providing favorable properties to its use and minimizing weaker ones. There are practically limitless in material types (metals, ceramics, or polymers with fiber, whisker, or particle reinforcement) and manufacturing methods (laminated, suspended, vapor-deposited, or clad).

Innovative composite materials have been implemented into many applications such as advanced aircraft components, high-performance automobile body structures, and the reinforcement of concrete structures. Fiber-reinforced and sandwich composites consist of two or more organic or inorganic components. Strong and stiff fiber reinforcements are some sort of backbone formation, while matrices can keep all the reinforcements into their positions. The physical and mechanical properties in composites can be tailored by the volume fraction and orientation of fibers in order to acquire desired properties for specific applications. Composite materials in the primary aircraft structures such as fuselage, wings, landing gear, and the engine provide lighter weight results in drag reduction and fuel savings. Graphite and carbon fibers are different, however, the terms are generally used interchangeably. Both graphite and carbon fibers are based on hexagonal graphene layer networks that show in carbon. Graphite is made of stacking of graphene layers into three-dimensional order. Graphite fiber fabrication is expensive due to the lengthened processing time and high-temperature process to form the molecular order. Carbon fiber fabric frequently present as only 2D order within the layer with weak plane and molecular disorder form. The stiffness and strength of carbon fibers are approximately 3 to 10 times higher than those of glass fibers. They also have high corrosion resistance and chemical stability. Carbon fibers, which are available in both dry fabric and prepreg, can be constructed from a variety of precursors including polyacrylonitrile (PAN) based, pitch-based, or rayon based materials [46]. The aerospace-grade graphite composite materials are incomparably providing a spectacular composition of strength and modulus, high strength-weight ratio, and rigidity compare to those of other composite materials as shown in Table 2-2. Due to the CFRP composite properties, they have been considered as a great material revolution for sports equipment, automobile, marine, and aerospace applications to replace traditional metallic materials in many weight critical applications [3].

The lack of functional property and high-cost are the major disadvantages in CFRP composites. Functional conductivities in CFRP composite are relatively poor compare to conventional metal alloy structures that are vulnerable to lightning strike damage. The poor functional property, especially in the thickness direction, is due to a consequence of the encapsulating insulating polymer matrix that can limit the applications. Thus, an LSP layer is an essential system in composite aircraft structure against the high lightning current. When lightning strikes on an aircraft, high electric charges will travel on the aircraft surface and discharge back to the air, much like a Faraday Cage. Due to the excellent electrical conductivity and low density, aluminum is primarily used as an LSP layer. Lightning-induced damage can be mitigated by the increase of functional conductivity allowing the current to travel only on the aircraft skin from the attachment point to some other locations without interruption or diversion to the interior inside the aircraft. However, the use of aluminum in composite aircraft structures could cause galvanic corrosion issues. Another metal material like copper can relieve the threat of galvanic corrosion but it is three times as heavy as aluminum. Hence, carbon-based LSP systems are developed to enhance both mechanical properties and functional conductivities.

Table 2-2. The comparison of mechanical properties between composites and metals [47].

Properties	**Graphite Composite (aerospace grade)**	**Graphite Composite (commercial grade)**	**Fiberglass Composite**	**Aluminum 6061 T-6**	**Steel, Mild**
Cost $/Kg	$45-$550+	$10-$45	$3-$7	$7	$0.7
Strength (MPa)	620–1380	245-620	138-240	240	415
Stiffness (GPa)	70 - 345	55-70	7- 10	70	205
Density (g/mm^3)	0.00138	0.00138	0.00152	0.00277	0.00830
Specific Strength	0.5-1x10^6	1.8-4.5x10^5	0.9-1.6x10^5	8.7x10^4	5.0x10^4
Specific Stiffness	0.5-2.5x10^5	4.0-5.1x10^4	4.6-6.6x10^3	2.53x10^4	2.47x10^4
CTE (1/°C)	-1.8-1.8x10^{-6}	1.8-3.6x10^{-6}	1.1-1.4x10^{-5}	2.3x10^{-5}	1.3x10^{-5}

2.2.1 The strength of composite materials

Lightweight, high performance and reliability, and low maintenance cost are the major factors of developed advanced composite materials for aircraft structures, as shown in Table 2-3. A concept of load sharing between fiber and matrix is one of the basic mechanical behavior in composite material. Most forces are carried by fiber reinforcements and the remnant of forces are absorbed by matrix polymer. Laminates have higher strength and stiffness than those of metals as shown in Figure 2-6, although metals are isotropic behaviors [48]. Composites have great efficiency to resist external loads along fiber direction because the strength and stiffness along the longitudinal direction are much stronger than those in the transverse direction as shown in Figure 2-7 [49].

Table 2-3. Factors of developed material for aircraft structures [50].

Pushing Factors	**Advantages**
Light Weight Structure	Better maneuverability, increase payload, and longer flight range
Advanced Performance	Better aerodynamic form, high-temperature capability, and damage tolerance
Reduced Cost	Less fabrication and assembly costs, result in a great fly-to-buy ratio
Less Through-Life Support Cost	Great fatigue and corrosion resistance, and diminished mechanical damage

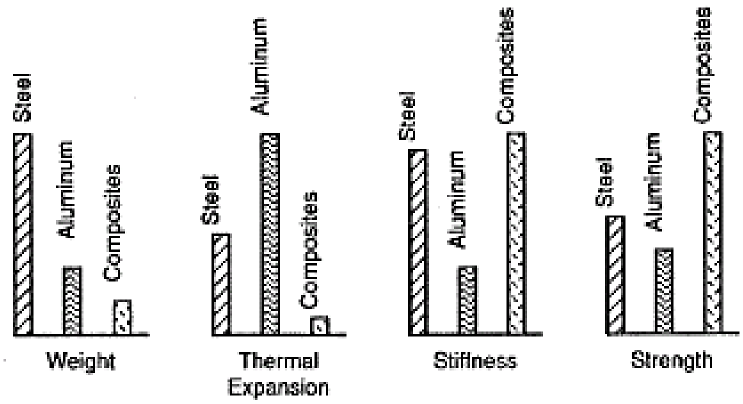

Figure 2-6. Property comparison between composites and metals.

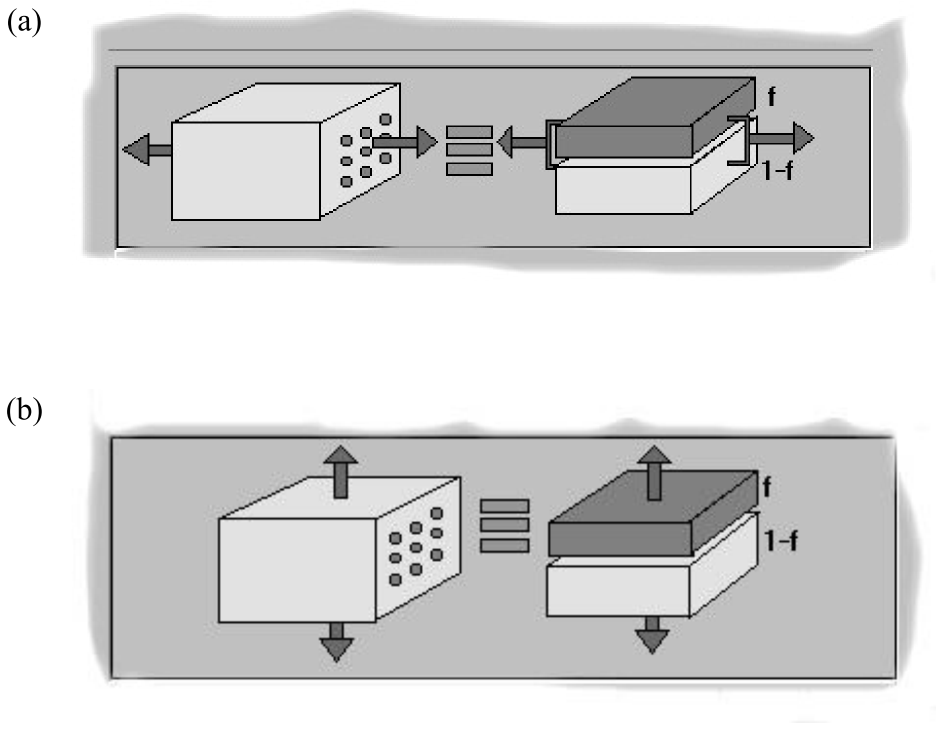

Figure 2-7. External loading in different directions on composite material of (a) longitudinal direction and (b) Transverse direction.

The unidirectional fiber composites show the maximum strength to weight ratio. However, the strength will be mitigated by 50% in all directions when fibers are placed perpendicular to the panel [48]. Fibers, which have excellent mechanical and functional properties, are the reinforcing agents that allow the stiffness and strength of the structural change due to the different fiber angular orientations. A low density is a beneficial parameter in composites, thus are generally applied in weight-sensitive applications. There are four types of textile architecture, which are discrete, continuous, plane geometry, and spatial geometry as shown in Figure 2-8.

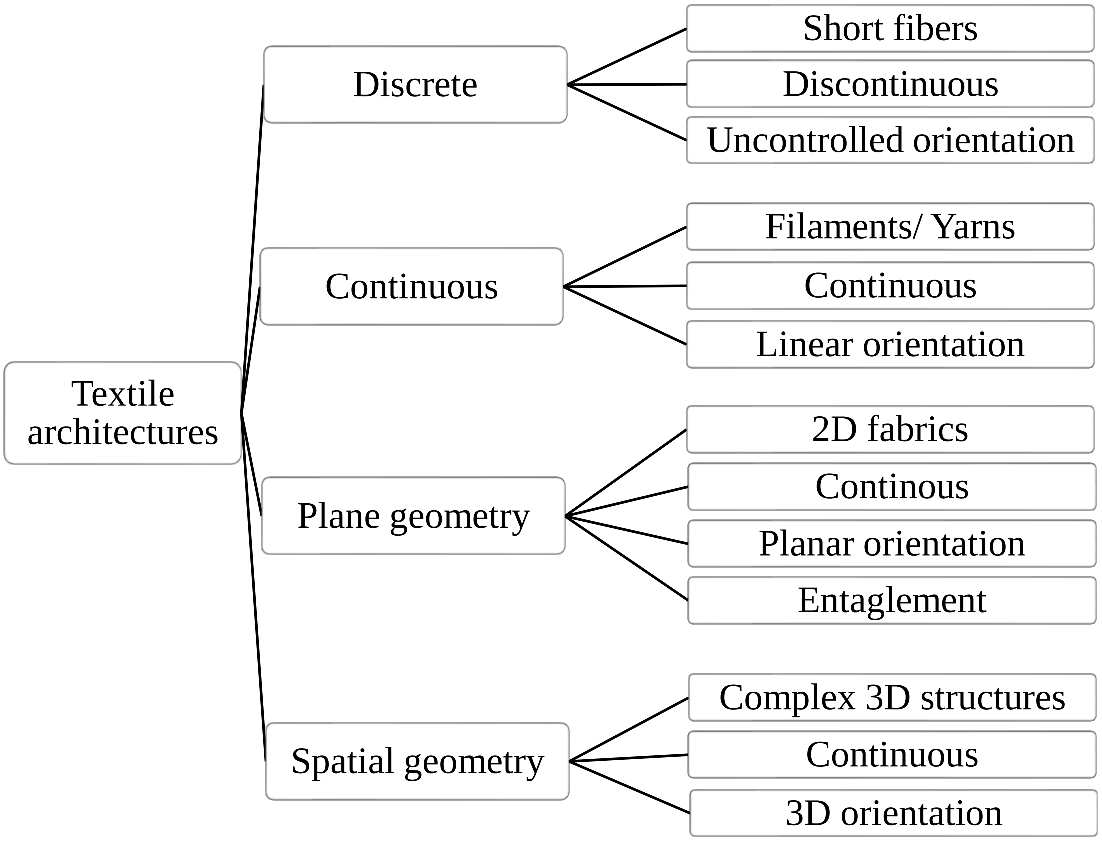

Figure 2-8. Classification of complex textile architectures as reinforcement.

Carbon fiber is a super-strong material with a lightweight structure that is thinner than human hair. It is approximately 5-10 μm in diameters with the majority of carbon atoms composition. There are numerous physical structures such as diamond and graphite, characterized by the crystalline or amorphous formations of bonded carbon atoms. The crystal alignment, which is a criterion of the carbon atom orientation, is affected by the degree of crystallinity providing incredibly strong fiber with a high strength-to-volume ratio. carbon fibers generally have the properties of high stiffness, excellent tensile strength, lightweight, chemical resistance, and superior temperature tolerance. The ultimate strength, modulus, and failure strain of carbon fibers are 3.5 GPa, 230 GPa, and 1.5%, respectively, thus offer a great opportunity to aerospace, luxury automobiles, civil engineering, military, and sporting equipment. Fabrics consist of at less two threads or yarns that are intertwined orthogonally to each other. The threads or yarns that lie along 0° to fiber direction or along the length of the fabric, are called the warp, whilst another yarns that interlace with fabric making 90° to the fiber direction, are known as weft [51]. Several weave patterns provide diverse abilities to crimp and drape. Crimp, which expresses the number of weaves per unit length, shows the fiber waviness, while drape is the ability of fiber fabric to conform to complex surfaces [52]. Thus, the crimp-ability can directly affect the drape-ability, in-plane permeability, and mechanical properties [53]. Table 2-4 shows types of a weave pattern, including plain weave, twill weave, satin weave, and basket weave.

Table 2-4. Comparison of properties in different weave styles [54].

Properties	Plain 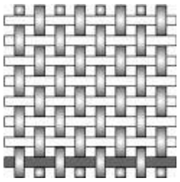	Twill 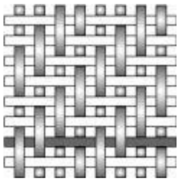	Satin 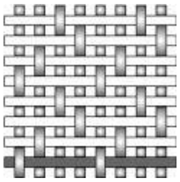	Basket 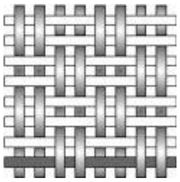
Good Stability	Good	Acceptable	Poor	Poor
Good drape	Poor	Good	Excellent	Acceptable
Low crimp	Poor	Acceptable	Excellent	Poor
Low porosity	Acceptable	Good	Excellent	Poor
Smoothness	Poor	Acceptable	Excellent	Poor
Balance	Good	Good	Poor	Good
Symmetrical	Excellent	Acceptable	Very poor	Acceptable

2.2.2 Composite fabrications

Fiber-reinforced composites can be fabricated by wet lay-up, spray lay-up, vacuum bag molding, autoclave curing, compression molding, or liquid composite molding [55]. Each technique provides different specific characteristics that are suitable for different applications. The cost-effectiveness and the rate of production depend on the types of composite material fabrication. Due to the dramatic market growth of the aerospace and automotive industries, many researchers have developed on the optimization of the production process. Prepreg, vacuum bag molding, autoclave, compression molding, and liquid composite molding are popular for composite manufacturing.

Hand lay-up process

Hand lay-up method is the simplest and versatile technique to fabricate composites due to simple infrastructural requirements, low volumes, and simple processing steps but it is mainly used thermosetting polymer [56]. Glass or carbon fibers are manually placed on the open mold after release agent is sprayed on the mold so composites can be easily taken out from the mold. Epoxy is mixed with a curing agent (hardener) with an appropriate proportion. The prepared matrix is then poured and brushed over the fibers. Another fiber ply is laid on the top of the previous fiber surface and then apply pressure on the fiber surface to remove air bubbles and excess polymer resin by a roller. The lay-up process is repeated layer upon layer until the desired structures are acquired. A thin plastic sheet is then placed on the sample to obtain a good surface finish. The mat specimen is normally cured at room temperature using the catalyst to harden the composites by resin itself or at a specific temperature in the oven.

Vacuum bag molding and autoclave molding

Another relatively low-cost fabrication technique is the vacuum bag molding method, which is used to consolidate the hand lay-up process or pre-impregnated lay-up. A vacuum is used to eliminate excess matrix resin and air bubbles by reducing pressure inside the bag and increasing external vacuum pressure. This process can manufacture complex shapes, large composites, and more advanced composites such as aircraft structural parts.

Prepregs are fabricated to desire structures from precut plies, followed by a non-adhering film of polyvinyl alcohol or nylon is located over the lay-up and sealed. Then, prepreg can be consolidated into a solid part by a vacuum at room or elevated temperature. Prepregs can also be consolidated using the vacuum bagging process and autoclave molding but a high processing cost is applied [57]. The autoclave is used to remove excess resin, improve fiber wet-out, and to reduce void contents improving the quality of composites with high reinforcement concentration and great adhesion between layers. Figure 2-9 shows the vacuum bagging molding process and autoclave.

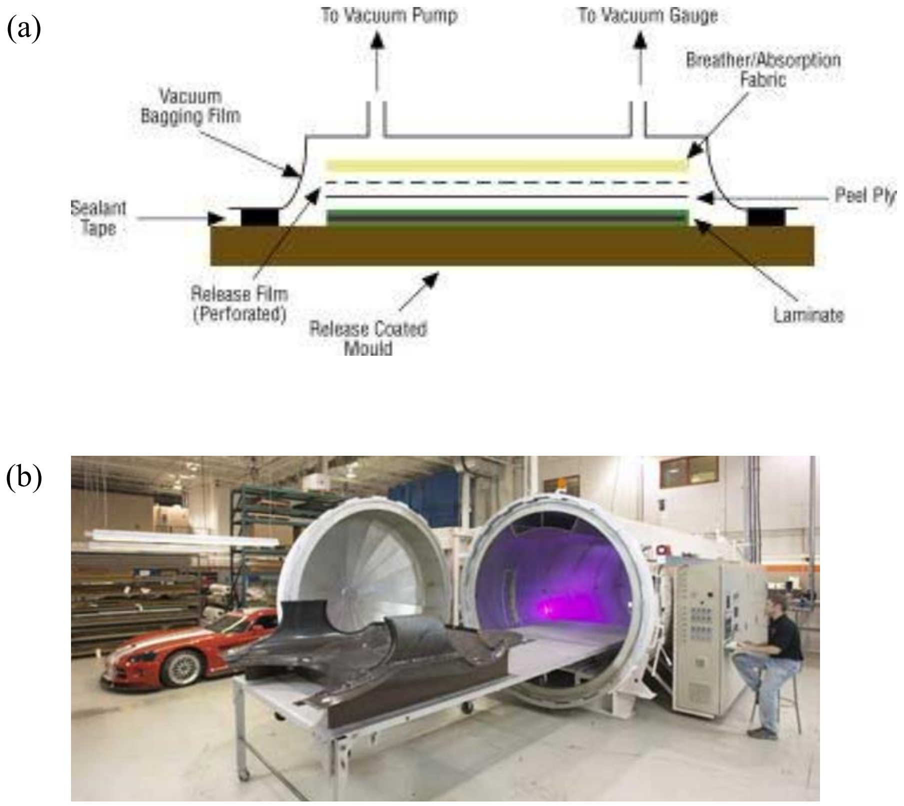

Figure 2-9. Fabrication process (a) vacuum bagging process and (b) autoclave molding.

Liquid composite molding (LCM)

Resin transfer molding (RTM) and vacuum-assisted resin transfer molding (VARTM) are two famous methods in the LCM technique. These two methods are the major manufacturing processes providing high-quality control and high-performance composites with advanced structural geometry. This method is one of the cost-effective processes to fabricate fiber reinforced composites without autoclave curing with less cost and time production.

RTM method uses a low-pressure closed system to fabricate intermediate volume production quantities. The prepared fibers are placed at the bottom of the mold. Resin is then pumped into the mold replacing air through strategically located vents and impregnating the reinforcements. The composite starts to cure when resin injection is stopped. A composite sample is then removed from the mold after the curing process is finished. Unsaturated polyesters, vinyl esters, epoxies, and phenolics are the common matrix resins. This technique provides uniform thickness, two-sides finished surfaces, and high quality finished parts with low tooling cost, simple mold clamping requirements, and rapid time processing that can apply for automotive body parts and containers. The RTM method can provide medium volume productions as shown in Figure 2-10.

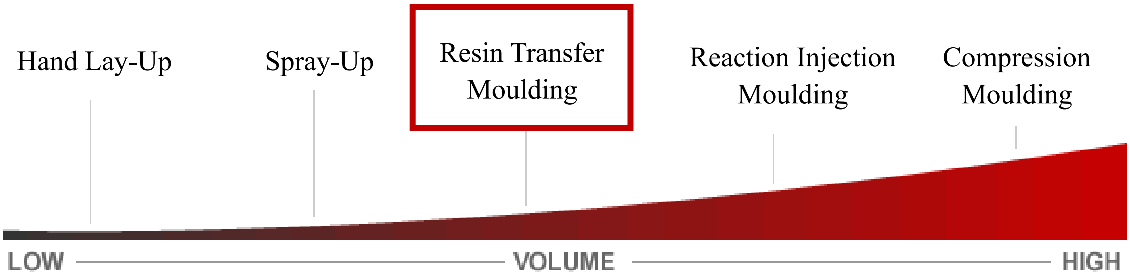

Figure 2-10. Summary of volume production with different manufacturing processes [58].

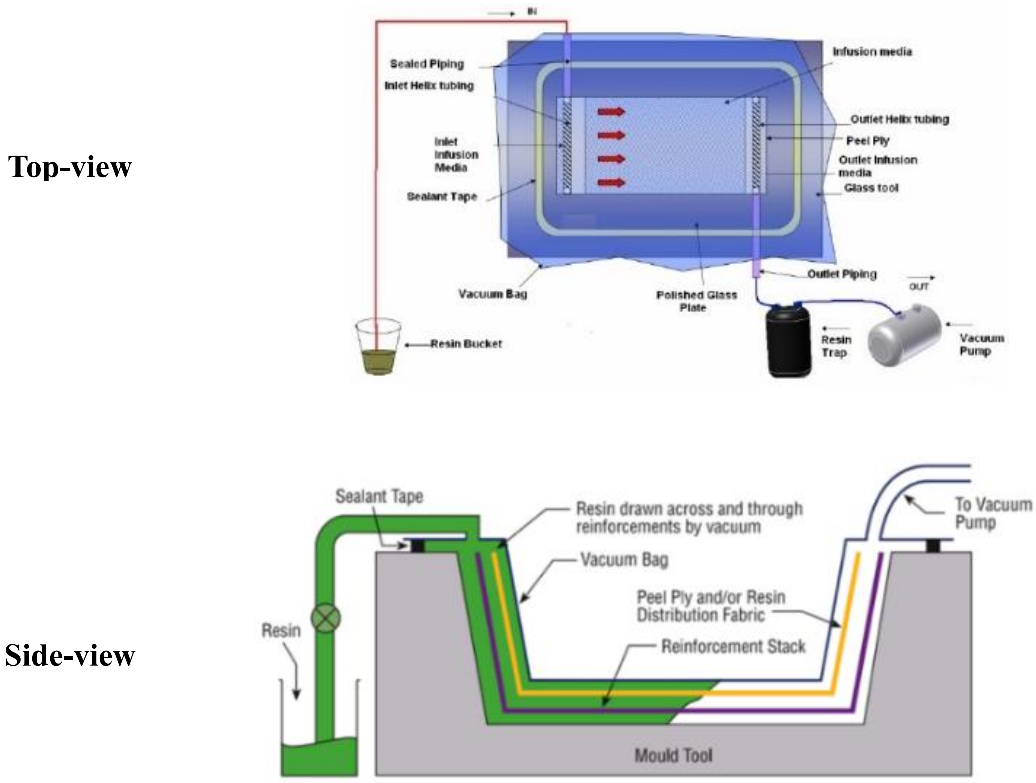

Figure 2-11. Top- and side-view of Vacuum-Assisted Resin Transfer Molding (VARTM).

A VARTM method is a modified RTM technique version. Figure 2-11 displays the set-up of the VARTM technique in the front and side views. Fibers are located on top of the peel ply, followed by another peel ply to facilitate the separation between composite and vacuum bagging. A spiral mesh is then placed on the top of the peel ply to guild resin to flow over fibers evenly. Two spiral tubes are laid at both the entrance and exit sides of the composite and then seal the mold with vacuum bagging. Resin is infused into the fiber composite by vacuum pressure as a top mold to impregnate at room temperature. Once the pressure inside the mold is lower than the room pressure, epoxy is infused into the fibers and starts to cure in the desired shape. Degassing resin is required to reduce air bubbles, voids, and dry spots in the composite results in an improvement in mechanical and physical properties. Hence, this method offers a high fiber volume fraction with superior strength and lightweight composite material structures with low-cost tooling machines. The VARTM is an inherently cost-effective process without any highly sophisticated equipment and large space fabrication requirement, while it is quite difficult to control dimensional tolerances, thickness and surface qualities, void contents over the curing process, and low-volume molding process [59] as shown in Table 2-5. Therefore, this method is extensively applied in many industrial applications.

Table 2-5. Summary of composites manufacturing processes.

Methods	Hand Lay-Up	Spray Lay-Up	Vacuum Bag and Autoclave	RTM	VARTM
Cost	Low	Low	Moderate to High	Moderate	Low
Surface Quality	Normal	Normal	Good	Good	Normal
Part Thickness	Non-Uniform	Non-Uniform	Uniform	Uniform	Non-Uniform
Void Content	Normal	Normal	Less to Least	Less	Normal
Health and Safety	Unsafe	Unsafe	Safe	Safe	Safe
Application	Aircraft Components, Automotive Parts, Boat Hulls	Automobiles, Large Structural Panels	Aircraft Components	Automotive Body Parts, Containers	Transportation, Marine, Infrastructure, Aerospace Application

2.3 Nanomaterials

The use of CFRP composite materials has been drastically replaced over conventional metallic materials due to excellent mechanical properties, lightweight, high resistance to environmental degradation. However, the major drawbacks of employing carbon fiber composites in structural applications are the lack of functional conductivities and low interlaminar toughness. Even though the in-plane functional conductivity in composites is much higher than their thickness direction due to a consequence of the insulating polymer, it is still limited to many applications. Thus, CFRP composites are susceptible to premature or unexpected failure caused by lightning strikes. Due to the advanced nanotechnologies and nanomaterials, researchers can provide many new ideas to fulfill the industrial specification and application requirements. The concept of nanotechnology to understand and to control matters in the nano-scale presenting new properties that bring great benefits to many companies and industries. Carbon-based nanomaterials have excellent mechanical and functional properties such as the high modulus-to-weight ratio. Thus, the integration of nano-reinforcements into the polymer can improve composite performances.

2.3.1 Graphite

Graphite is one of the common well-known crystalline carbon structures. The structure of graphite is stable under standard conditions. It consists of several stacked layers of hexagonal carbon sheets, which are called graphene or graphene sheets. Each layer of graphene is loosely bound together by van der Waals interactions [60] so layers of graphite can easily be sheared off providing great value in the dry lubricant industrial application. It can also use as conductive fillers, battery electrodes, and nuclear fission reactors.

Graphene consists of many hexagonal rings that each carbon atom is bonded to three other carbon atoms by covalent bonds creating thin parallel plates [61]. Three sp^2 shared with three neighboring carbon atoms are bonded in the in-plane direction of graphite forming the layer of honeycomb networks in planar structures. The strong in-plane bonding and weaker inter-planer bonding of graphite are the covalent bonds and van der Waals forces, respectively. Graphite sheet can separate into graphene due to the weak out-of-plane bonding. Hence, the graphite properties in the in-plane direction have higher than those in the out-of-plane direction. Benjamin Collins Brodie attempted to oxidize graphite with nitric acid and potassium chlorate results in graphic acid in 1859. However, this graphitic oxide cannot be dispersed in acid, but easily disperse in water. This graphite oxide production is slow and hazardous due to the concentration of sulfuric and nitric acid. Then, Hummers' method is a method that improves the production rate of graphite oxide using a mixture of concentrated sulfuric acid (H_2SO_4) and potassium permanganate ($KMnO_4$) [62]. This method is a fast, safe, and efficient technique to produce quality graphite oxide.

2.3.2 Graphene

Graphene is one of the ideal nano-materials since its invention. A honeycomb network layer of a planar structure, which is also called monolayer graphene, is formed by sharing sp^2 electrons with their three neighboring carbon atoms. The tightly bond sp^2 hybridized orbitals form an in-plane σ bond with three other carbon atoms in the triangular planar structure of graphene [63], as shown in Figure 2-12. These covalent carbon-carbon bonds are close to the sp^3 hybridized carbon-carbon bonds in a diamond, thus graphene shows similar mechanical and thermal properties as the diamond. The remaining fourth valence electron in the $2p_z$ orbital is normal to the planar structure forming an out-of-plane half-filled π bond that provides unique electronic properties. A tight-binding model is applied to calculate the graphene electron band structure. The Dirac cone and electronic bands of graphene can be observed in Figure 2-13. A π energy (bonding) and $\pi*$ energy (anti-bonding) locate on the lower-half and upper-half in the energy dispersion curve, respectively. When the Fermi energy is in the middle of the band showing the zero-energy reference, the Fermi surface is defined by the Dirac point (K and K′). When the Fermi level shifts from the point of degeneracy band, a small overlap in graphite defines as semi-metal. The electron energy is linearly dependent on the wave vector close to the crossing points. According to the Dirac equation describe relativistic fermions, the linear dispersion at low energies does the electrons and holes in graphene imitating relativistic particles with zero effective mass [64].

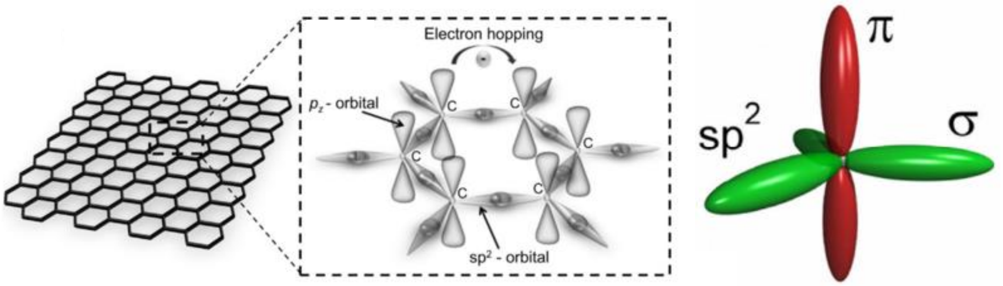

Figure 2-12. sp^2 and p-orbitals of carbon atoms in graphene [65,66].

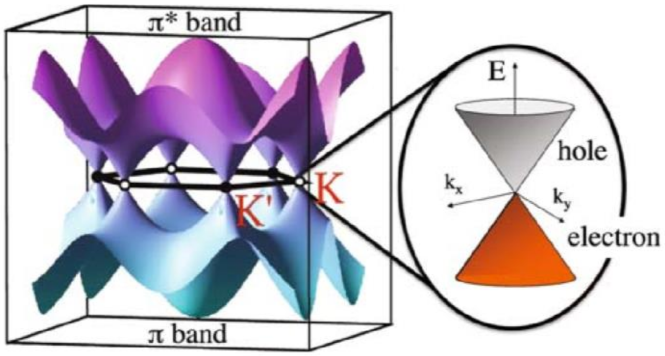

Figure 2-13. Graphene π and π∗ electronic bands and the Dirac cone [67].

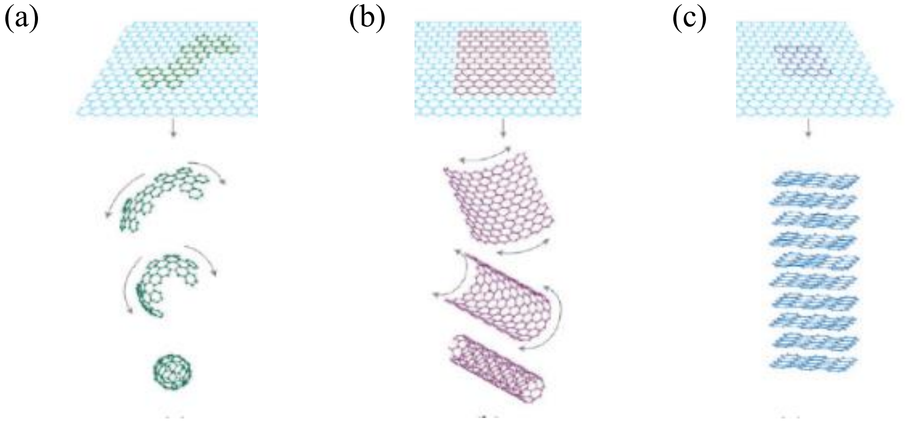

Figure 2-14. Graphene fundamental structures of (a) 0D buckyball, (b) 1D carbon nanotube, and (c) 3D graphite.

A single layer of carbon atoms arranged in a honeycomb lattice can be wrapped up into 0D buckyball or fullerene, rolled into 1D CNT, or stacked into 3D graphite [68] which can be seen in Figure 2-14. A high aspect ratio of graphene has remarkable mechanical, electrical, thermal, electronic, and optical properties. The cost-effectiveness of graphene is truly ideal for improving the properties of polymer composites because the large quantity of graphene production is less expensive than the production of CNTs. There are several methods to manufacture graphenes such as graphene oxidation chemical reduction, microwave CVD, and graphene oxide thermal exfoliation [69,70]. Graphene has a larger contact surface area leading to better reinforcing in polymer composites. Homogenous dispersion of graphene into a polymer matrix is a key challenge due to the high van der Waals intermolecular forces among their particles and large surface area causing a greater degree of aggregation. Then, chemical surface modification of graphene is used to create a strong covalent bonding between graphene and polymer matrix in order to enlarge polarity and to improve load transfer efficiency. Many researchers have demonstrated the successful results of increasing the solubility and interfacial bonding [69,71] by applying chemical functionalization of amine-function groups on the graphene-based by the modified Hummer and Offeman's method [62].

2.3.3 Graphene nanoplatelets (GNPs)

Graphene nanoplatelets (GNPs), which are made of a few stacks of the graphene layer, display as a potential candidate to boost material properties. They have extraordinary physicochemical properties and great potential to improve polymer matrix phase properties at very small amounts. The enhancement of matrix-dominated properties such as the flexural and interlaminar shear strength is nontrivial considering that their failure can lead to a catastrophic breakdown of composite structures due to weak fiber-matrix interfaces and the brittleness of many polymer matrices [27]. It has been reported that mechanical properties were improved due to the inclusion of graphite nanoplatelets in fiber-reinforced composites [13]. The integration of GNP paper in the multilayer laminated composites not only improved mechanical properties, but also resulted in an enhancement of electrical and thermal conductivities, providing multifunctional materials that can be used in many applications [14]. For instance, it was shown that the addition of 0.7 wt.% graphene oxide in PVA resulted in 76% and 62% increase in tensile strength and Young's modulus, respectively [72]. The reinforcing effect of 4% graphite in epoxy resin increased the glass temperature value from 155 to 175°C [73]. Only 0.2 wt% of graphene integration improved the fatigue life and prevented the delamination/bucking of fibers providing high potential for safety, reliability, and cost-effectiveness materials [74]. The bending strength increased 102% with the incorporation of 0.5 wt% graphenes to carbon/epoxy composites, which changed the failure mechanism from intra-laminar failure to combinational mode of inter- and intra-laminar failures [75].

2.3.4 Carbon nanotubes (CNTs)

Carbon nanotubes (CNTs) were first discovered by Sumio Iijima in 1991 opened up a new era in material science. CNTs have excellent mechanical, electrical, and magnetic properties offering at least 100 times stronger than steel with much lighter weight. The structure of CNT consists of enrolled cylindrical graphene rolled up into a seamless tube structure with a nanometer scale in diameter. Thus, it is composed of sp^2-bonded carbon atoms arranged in a honeycomb (hexagonal) pattern. CNTs have three different unique geometries, namely, zig-zag (n,0), armchair (n,n), and chiral (n,m). These three structures can be classified by the wrapping graphene sheet into a tube that can be observed in Figure

2-15. Three types of 1D CNTs are single-walled carbon nanotubes (SWNTs), double-walled carbon nanotubes (DWNTs), and multi-walled carbon nanotubes (MWNTs). SWNTs are the simplest structures of the carbon nano-structures composing of a single graphene sheet rolled into a cylinder. The tensile strength and modulus of SWNTs are approximately 100 GPa and 1 TPa, respectively, which are affected by the arrangement of carbon atoms and defectiveness in the carbon network. MWNTs consist of two or more SWNTs nested inside one another. They are strong, light-weight, and offer either metallic or semi-conductive properties. The tubular structure of CNT also enables ballistic electron and phonon transport providing spectacular current-carrying and heat-conducting capacity [76]. SWNTs conduct nearly 2 trillion electrons per second through approximately 3 nm nanotube molecule diameter that is about 10^9 A/cm^2. On the other hand, copper conducts about 2 million electrons per second through an approximate 3 mm cross-sectional area of wire [77]. Another interesting property of CNTs is the joining of a junction or gap between two gradual differences in physical structures together can function as an electronic device. The varieties of electronic behavior depend on the connection between two tubes structure. Due to advanced technology, high-quality carbon nanotubes can synthesize a large quantity, which has a high degree of purity and fewer defects. Due to the extraordinary physical and chemical properties of CNTs, they can be applied to nanosensors. These nano-sensors could behave like semiconducting materials in microelectronic circuits, or detect small changes in electric current, or register chemical reactivity, or changes in air pressure or temperature.

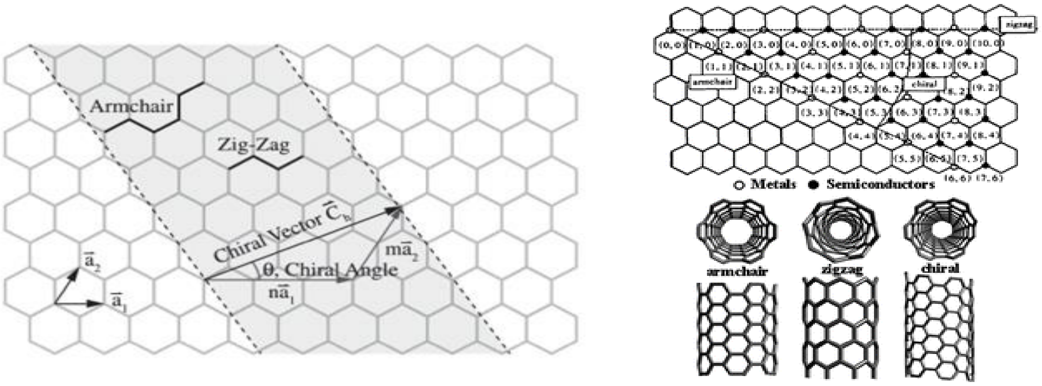

Figure 2-15. Schematic diagram of a rolling graphene layer into different types of CNT [78,79].

2.3.4.1 Synthesis of CNTs

Three primary CNT synthesis methods are arc discharge, laser ablation, and CVD, which will be discussed in detail below.

Arc Discharge

An arc discharge, which was the first CNT synthesis methods, was explored by Iijima in 1991 at the NEC Laboratory in Japan. A synthesis technique relies upon the vaporization of carbon applying direct-current arc voltage across two graphite electrodes in the presence of one or more different catalysts under vacuum or inert gas atmosphere. The space between two graphite electrodes is less than 1 mm that generates a necessary electric arc from carbon vaporization. A driving potential of about 30 V from a direct current (50-120 A) generates high-temperature plasma (> 3,000 °C) between the two electrodes. The vaporize of carbon is generated on the anode electrode and then instantaneously condenses on the cathode electrode to synthesize CNTs and other carbonaceous by-products in the inter-electrode plasma region. There are two predominant methods, which are drilling and uniform dispersion method, to introduce catalyst into the reaction. A hole is drilled at the end of the anode graphite electrode and then fills with a metal catalyst and graphite powder in the drilling method. Types of SWNTs, MWNTs, or a mixture of both CNTs depend on the catalyst. The different shapes of MWNTs produced in different ambient gases can be observed in Figure 2-16.

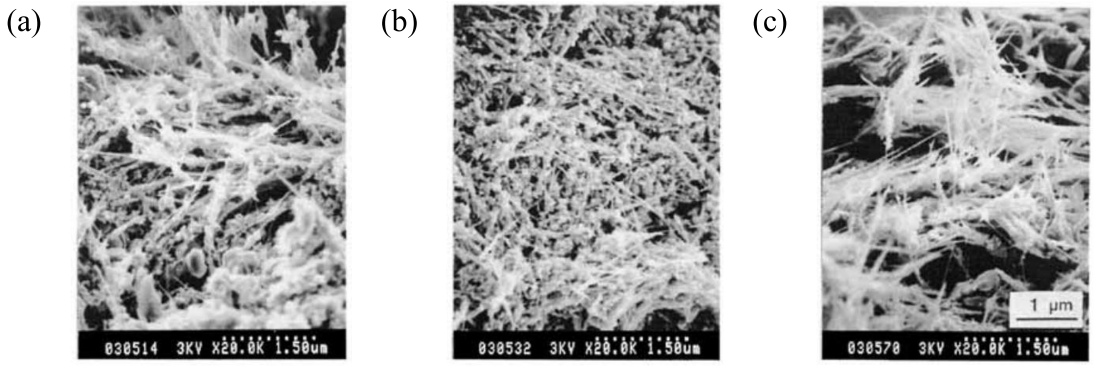

Figure 2-16. SEM images of MWNTs produced by arc discharge at different ambient gases of (a) helium (He), (b) argon (Ar), and (c) methane (CH_4) [80].

Laser Ablation

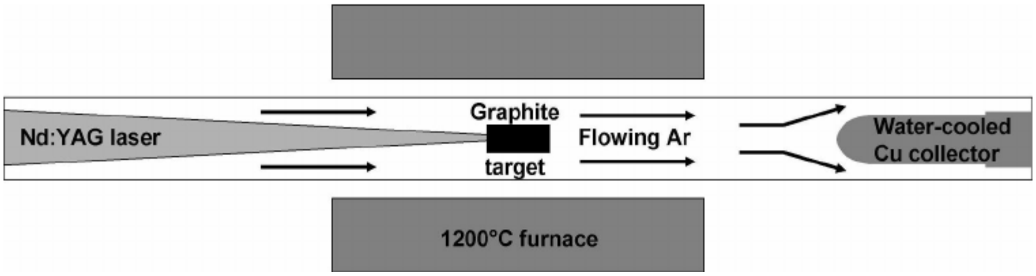

Figure 2-17. Schematic of the laser ablation apparatus for the CNT synthesis [81].

CNTs were first synthesized using a double-pulsed laser oven process at Rice University in 1996. The laser ablation technique utilizes a high power laser to vaporize carbon from the graphite target at high temperatures. A coated graphite target with metal catalysts is placed inside a furnace at around 1,200 °C under an argon atmosphere, followed by heat treatment in a vacuum at 1,000 °C to remove the C_{60} and other fullerenes as shown in Figure 2-17. The intensity laser is then directed onto the pellet in either a pulsed or continuous fashion causing the vaporization of metal and graphite. Argon gas acts as a carrier gas that carries the vapors from a high-temperature chamber into a cooled collector positioned downstream. CNTs are then self-assemble from carbon vapors and condense on the walls of the flow tube. The pressure and argon flow rate are typically 500 Torr and 1 cm^3/s, respectively. The types and sizes of CNT are different due to the varieties of CNT growth parameters, including processing temperature and catalyst composition. Both MWNTs and SWNTs can be produced with this technique as shown in Figure 2-18. This method provides higher purity (>70wt% purity) of CNTs than those produced in the arc discharge technique [82]. Even though arc-discharge and laser vaporization can synthesize high quality of CNTs, the inherent design in these systems and their energy intensiveness pose a limitation to large-scale production. Firstly, vacuum conditions are required to prevent the interference of mixed with unwanted ion formation at the high temperature so it is difficult and expensive to scale up the CNT production to the industrial level using these approaches. Secondly, graphite targets and electrodes require continuous replacement as the synthesis proceeds, hence this technique is very difficult to be continuously operated. The produced CNTs are difficult to purify, manipulate, and assemble to construct nanotube-device architectures for practical applications [83].

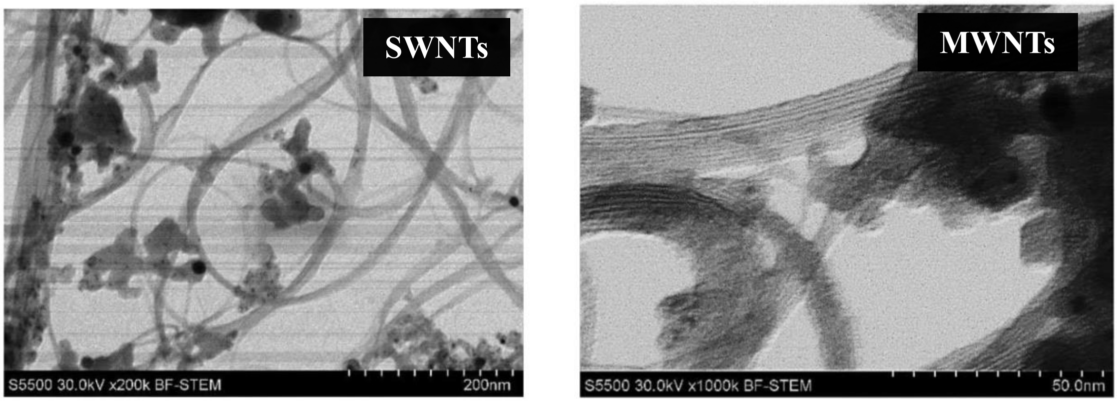

Figure 2-18. TEM images of SWNT and MWNT synthesis by laser ablation [84].

Chemical Vapor Deposition (CVD)

Chemical Vapor Deposition (CVD) method offers more accessible control of CNT production and can also scale-up the quantity to the industrial scale. This method can be considered as a thermal dehydrogenation reaction using some supported catalysts such as iron (Fe), cobalt (Co), or nickel (Ni) to decompose a hydrocarbon feed into carbon and hydrogen. Types of catalysts are the major concerns in CNT formation because they provide different ability to decompose carbon-containing molecules and solubility. In the pretreatment step, a metal thin film-deposited substrate is placed into the furnace and heated to the desired annealing temperature. This catalyst film undergoes heat-induced surface diffusion and collides with each other to form nanoparticles. Then, carbon source, either in the gaseous, liquid, or solid phase, is introduced into a reactor in a growth chamber in the processing temperature range of 750-1200 °C. The hydrocarbons within the carbon source are transformed into pure carbon molecules. These carbon molecules are diffused onto the substrate by carrier gases such as hydrogen (H_2), nitrogen (N_2), or ammonia (NH_3) and then deposited over or under the catalyst nanoparticles on the substrate surface to form CNTs. Figure 2-19 illustrates the schematic diagram of the experimental setup for the CVD system. It is a useful method to synthesize and to control CNT structure due to its versatility and flexibility in adjustable parameters, including carbon precursors and catalyst options. CNTs can be grown on the substrate with the same morphology as its specific catalyst pattern. The quality of CNTs depends on many factors such as growth time duration and catalyst thickness [22], feed gas composition [23], feed gas flow rate, carrier gas, catalyst precursor composition, and processing temperature [24].

There are 2 different modes of CNT growth, which are tip-growth and base-growth mode as shown in Figure 2-20. Hydrocarbon vapor decomposes into carbon and hydrogen when comes in contact with hot metal nanoparticles. Hydrocarbon decomposition has released some heat to the metal's exposed zones, which is called the exothermic process. On the other hand, carbon crystallization has absorbed some heat from the metal precipitation zone, which is called the endothermic process. The interaction of catalyst-substrate plays a determinant role in this CNT growth mechanism. A weak catalyst-substrate interaction leads to the "tip-growth model". Hydrocarbon decomposes on the top surface of metal and carbon diffuses down through metal, where has an acute contact angle with the substrate. CNT precipitates out across the metal bottom and lifts the metal catalyst upward. CNTs continue to grow longer on the surface of the metal, are still open for fresh hydrocarbon decomposition because the concentration gradient exists in the metal allowing carbon diffusion. The growth of CNT is stopped when the metal particle is fully covered with excess carbon. Initial hydrocarbon decomposition and carbon diffusion take place similar to the tip-growth case, on the contrary, CNT precipitation fails to shove metal away from the substrate. This is the result of the strong interaction between catalyst and substrate and an obtuse contact angle between metal and substrate. The precipitation is, then, compelled to emerge out from the peak of metal, where is the farthest and slightest interaction with the wafer. The catalytic particles are stuck on the substrate and lift CNTs upward, which is known as the "base-growth model" [85,86].

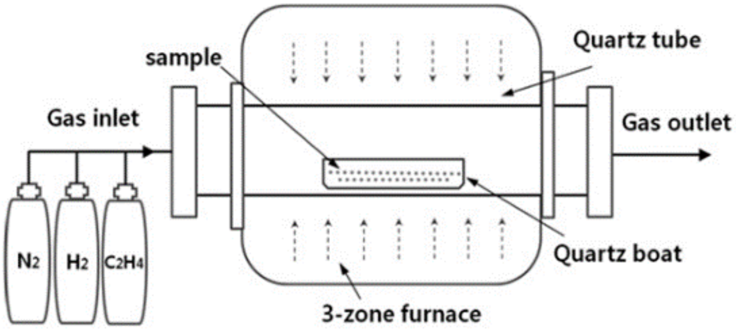

Figure 2-19. Schematic of the CVD apparatus for the CNTs grown [87].

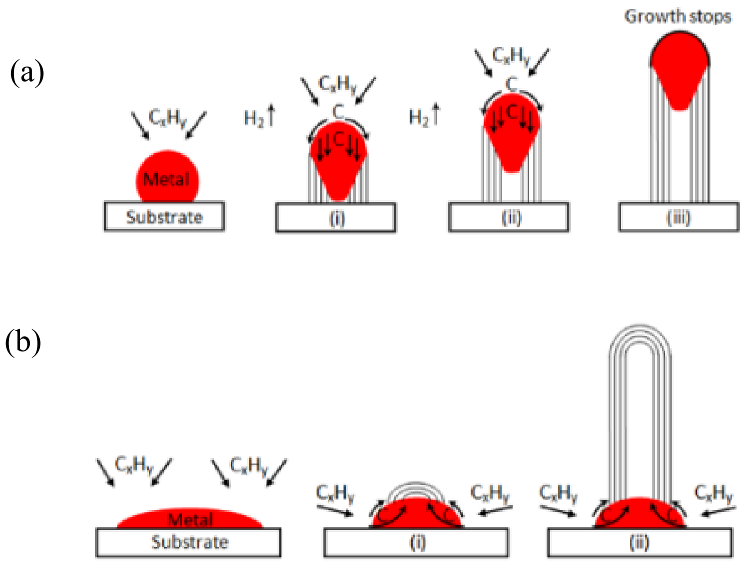

Figure 2-20. CNT growth mechanism of (a) tip-growth model and (b) base-growth model.

2.3.4.2 CNT Functional Conductivity

Electrical conductivity

One-dimensional CNTs have spectacular electrical and thermal conductivity. CNTs can be metallic, semi-metallic, or semiconducting with various sizes of energy band gaps based on their diameter and chirality. The electrical conductivity of CNTs depends on its geometrical structure. The theoretical conductivity of SWNT varies from semiconducting to metallic depending on the rolling angle and diameter of the tube (chirality). The metallic SWNTs can be defined by the indices (n,m) as follow:

Metallic : $(2n+3)/3 = p$, where p is an integer

Semiconducting : $(2n+3)/3 \neq p$, where p is an integer

In the case of armchair (*n*,*n*), these armchair tubes are always metallic ($p = 0$). However, most of the CNTs are semiconductors and only one-third of CNTs are metallic. The individual CNT can be characterized by their electrical conductivity along their tube axes using two- or four-probe methods to apply contact electrodes on CNT ends. The CNT resistances could vary from a few kΩ to a few MΩ [88]. Hence, many researchers have studied SWNT conductivity in a lower temperature range, but the effects of temperature on electrical conductivity are much smaller than those of tube types and qualities. The diameter range of MWNT is from 10-100 nm, which has a larger diameter than that of SWNT so electric bandgaps are minimized offering mostly semimetallic property. The disorder of MWNTs is higher than those of SWNTs because mostly discontinuous shells can be observed throughout the tube [89,90]. Due to the poor electron density, semimetallic MWNT tubes are more responsive to disorder, phonon scattering at defects, and phonon shortens the electron mean free path. Therefore, inelastic collisions primarily through electron-phonon interactions are the dominant result of diffusive and ohmic transport. An individual SWNT or MWNT is electrically more conductive than metals, thus CNTs can potentially substitute metal-mesh or coated on composites and deliver required properties with lighter weight.

Thermal conductivity

Carbon-based materials such as diamond or graphite manifest one of the maximum thermal conductivity at moderate temperatures. The longitudinal thermal conductivity of CNT could exceed that of graphite in the in-plane direction due to the long-range crystallinity of CNTs. The thermal conductivity of graphite is generally dominated by phonons and restrained by small crystallite size. A phonon is a quantum mechanical description of a typical vibrational mode that plays a significant role in many physical properties of condensed matter, including thermal, transport, and mechanical properties. There are three regimes of phonon transport behavior, namely, ballistic, quasi-ballistic, and diffusive that varying from a different range of temperatures. The Boltzmann method provides a physically insightful description of diffusive transport in SWNT, while ballistic phonon transport has been explored using Landauer theory, to describe quantized electrical and thermal transport in SWNT [91,92]. At low temperatures, the mean free path of phonon in SWNT has included the effect of boundary, mass-defect scattering, and length of CNTs. Due to the typical length of 1D SWNTs, the commonly perceived length for boundary scattering and mass-defect scattering are not necessarily the same as the total length of the CNT tube [93]. Hence, a 1D ballistic phonon conductor is performed in SWNTs without defects when the length is shorter than the phonon mean free path (MFP). In this regime, only acoustic modes conduce to transport, then thermal conductivity is independent in the tube chirality and enlarges linearly with the temperature [94]. As the temperature increases, both acoustic and optical phonons conduce to thermal transport, so the phonon MFP is reduced. Once the length of CNT is longer than the phonon MFP, thermal conductivity behavior will deviate from its linearity of the CNT length and categorizes into a quasi-ballistic transport regime. In this regime, the thermal conductivity follows the power law of temperature with an exponent, positive, and smaller than one. At high temperatures, phonon-phonon scattering known as the Umklapp process is the dominant factor (three-phonon and/or four-phonon Umklapp scattering). This uses to reduce the phonon MFP generating the diffusive transport regime where the thermal conductivity is expected to reduce as 1/T following the power-law with a negative exponent. Therefore, the measured MFP, which is both a function of temperature and tube radius, could control the thermal conductivity of CNTs. A 2 μm long SWNT has been experimentally measured in its thermal conductivity as a function of temperature. The thermal conductivity reached almost zero at cryogenic temperatures, increased up to the maximum point closely at room temperature, and then relatively dropped with the increase of temperature [95].

There are two major effects of phonon dispersion on rolling graphene into CNTs. The first effect is the collapse of the 2D band structure into 1D. Based on the periodic boundary conditions of CNTs, the circumferential wavevector is quantized and discrete sub-bands develop. The second effect is to rearrange low-energy acoustic modes because CNTs contain four acoustic modes which are LA mode (corresponding to the motion of atoms along the tube axis), Two degenerate TA modes (corresponding to atomic displacements perpendicular to the nanotube axis), and twist mode (corresponding to a torsion tube around its axis). The LA mode in CNT is exactly analogous to the LA mode in graphene. The TA modes in SWNT, on the other hand, are a combination of the in-plane and out-of-plane TA modes in graphene. There is a similar effect of stacking graphene sheets into 3D graphite in both MWNTs and SWNT ropes. This causes phonon dispersion in the z-axis that leads to a significant reduction of specific heat at low temperatures. In SWNT rope, phonons will propagate in both individual tubes and between parallel tubes in the hexagonal lattice direction conducting to steeply disperse in longitudinal (along-tube) and more weakly disperse in transverse (inter-tube) directions. Then, the twist mode becomes an optical mode because of the presence of nonzero shear modulus between neighboring CNTs. Since there is no theoretically addressed in the phonon dispersion of MWNTs, strong phonon coupling between layers of MWNTs should roughly have similar behavior as graphite. Due to the lack of bonding between the layers in MWNT, the interlayer coupling could conceive much lower than in graphite, especially in a twist and LA modes.

The thermal conductivity of MWNTs is also dominated by phonon transports as similar to SWNTs. However, MWNTs have more complicated transport phenomena and do not allow 1D ballistic phonon transport at low-temperature due to bigger diameters and multiple walls. In the case of graphite, the in-plane thermal conductivity can be roughly estimated without inter-planar coupling effect consideration. The temperature-dependence of the thermal conductivity of MWNTs should be close to their constituent tubes. However, an inter-tube scattering of MWNTs can also introduce and could somehow perturb both the magnitude and the temperature dependence of the thermal conductivity. Thus, the thermal conductivity of the MWNT system increases with temperature squared or 2D transportation. Inter-wall interactions of MWNT become negligible at room temperatures. Thermal conductivity theoretically reaches the peak at around 50 °C and relatively declines above 50 °C due to strong phonon-phonon Umklapp scattering. Owing to their splendid functional conductivity, embedding CNTs in CFRP composite are used as electromagnetic shields in stealth applications and radar absorbents [96] because it creates conductive pathways between carbon fiber plies for electrical discharge. The high aspect ratio of CNTs provides a physical network in the polymer improving thermal and electrical conductivity [20]. The thermal conductivity of an individual CNT normalizes to bulk density is still higher than metals. Thus, CNTs privilege in thermal conductivity and weight saving over metal-based materials.

2.4 Polymer nanocomposites

Nano-scale fillers have a great surface-to-volume ratio and a high fraction of atoms localized at the surface compared to micro-scale fillers. Even though many nanoparticles can improve material performances, the unsuitable dispersion methods can diminish the composite material properties. The major challenges of nanofiller distribution in the polymer matrix are the forming of filler agglomerations and the maintenance of stable dispersion. These could limit their potential and effect of nanoparticles in the matrix such as interfacial adhesion between polymer and filler particles. Therefore, the uniform nanofiller dispersion in the composite material can provide less free volume ratio, and high interfacial interaction results in better material properties and performances. The quality of filler dispersions can also affect the final structural properties of the products. Thus, the homogeneous filler-matrix dispersion is a significant step that needs to focus in order to produce great interfacial fiber-matrix compatibility and adhesion at the contact area. These effective techniques, such as high-shear mixing, solution blending, melt mixing, and in-situ polymerization, are commonly applied in several industries and research fields to improve the quality of the filler-matrix composite distribution.

High shear mixing

A high shear mixing technique is the most common method to directly disperse solid nanoparticles into the polymer matrix, especially thermosetting polymer. Three roll milling machine is a standard type to disperse the micro-scale particles into the polymer matrix, which is normally used in industries such as cosmetics, paints, and coating companies. This three roll calender, where the material is placed in between rotating rollers, has an easy approach to prepare and produce polymer composite products [97]. The calendar method has been applied to disperse DWNTs into epoxy resins. This is a suitable method to exfoliate and disperse carbon nanotubes into epoxy because it does not seem to decrease the length of DWNTs, which investigates by scanning electron microscopy (SEM) and transmission electron microscopy (TEM). The advantages of the high shear mixing technique are the possibility of scaling-up the capacity without losing the efficiency of the distribution, however, the limitation of high shearing might break the fibrous nanoparticles so then the aspect ratio becomes smaller.

Solution mixing

One of the most popular techniques to fabricate polymer composites is solution mixing methods. Nanofillers are dissolved in solvents or solvent mixtures and then mixed with the polymer matrix. The suspension of nanofiller-matrix is sonicated by ultra-sonication to obtain homogenously filler-matrix dispersion, and then subsequently removed the solvent by evaporation. The van der Waals force among nanoparticles is reduced and the aggregates are broken, which depends on the interactions between nanoparticles and solvent molecules. The macro-molecules diffuse into the space between nanoparticles during the evaporation process. Organic solutions such as water, acetone, and dichloromethane (DCM) are generally used as soluble solvents in the solution mixing techniques. This solution blending technique also offers an assuring approach to disperse the graphene oxide platelets into a certain polymer matrix [98].

Melt blending

A melt blending method is commonly used to synthesize nanocomposites, especially for thermoplastic polymers. The procedures of melt blending techniques utilize the high temperatures and shear forces dispersing the reinforcement phases or fillers in the polymer matrix to form the mixture of a molten polymer with nanoparticles. The annealing in the compound requires a temperature above the glass transition temperature. The cooling of the molten blending forms resultant nanocomposites. One of the melt blending method benefits is to prevent the use of toxic solvents, thus this process is more environmentally friendly and much more cost-effective than that of the solution mixing method. It also offers major attention in fabricating hybrid polymer nanocomposites at a fast pace and large-scale. However, the fibrous nanoparticles might break under high shear, results in reducing their aspect ratio during the extrusion process. In the case of graphene oxide polymer, the polymer matrices become soft during the high-temperature processing, allow graphene oxide particles dispersed easily. Nevertheless, the increase of viscosity of large percentage loading of fillers makes the dispersion of graphene oxide sheets less effective compared to other techniques such as solution mixing and in-situ polymerization. The high shear forces could cause buckling, rolling, or shortening the length of graphene oxide fillers. Even though the workload of graphene oxide production in chemical reduction has been constrained by graphene nanoparticles, a bulk quantity of thermal reduced graphene oxide product is a suitable alternative for many industries.

In-situ polymerization

An in-situ polymerization technique can be used to prepare nanopolymer composites for both thermoplastic and thermoset polymer. Nanoparticles are mixed with neat or multiple monomers. Monomers have replaced into the space between the nanoparticles, the high shear device or ultrasonication is then used to sonicate an initiator for thermoplastics, or a curing agent for thermosets to obtain homogeneous polymer nanocomposites. The small molecule size and great moveability of monomer can easily diffuse into the aggregated particles and the polymer chains can directly grow from the particle surface so the space between particles can expand further. Thus, the improvement of the interfacial interaction in nanopolymer composite materials can be acquired. The in-situ polymerization methods can produce both covalent and non-covalent composites such as epoxy with covalent crosslink between resin matrix and filler, and PMMA or polyethylene for non-covalent composites. These methods also have an excellent level of dispersion of graphene fillers without prior exfoliation comparing with other techniques such as solution blending or melt mixing [98]. Hence, this technique is another approach to ensure better filler dispersions and excellent interactions between fillers and matrix.

CHAPTER 3

Development of CNT-Hybridized Fibers and CNT Morphology

The method of CNT synthesis consists of carbon fiber fabric substrate preparation and the CNT growing process. The implementation technique of CNTs into polymer has a great influence on composite properties. Numerous papers are working on the direct integration of CNTs into the matrix polymer, followed by CFRP composite fabrication using the RTM technique. However, several challenges are revealed in composites because of high matrix viscosity and CNT dispersion quality. The high percentage of filler content of nano-reinforcement increases the viscosity in the polymer. Then, the high viscosity could cause unfortunate circumstances such as filler agglomeration resulted in imperfections or stress concentration in composites. The direct synthesis of CNTs on the carbon fiber surface, therefore, is one of the promising approaches to overcome non-uniform filler dispersion, agglomeration of CNTs, and high viscosity of polymer challenges. A number of studies have shown that CNTs can be grafted [99-101] or grown on carbon fiber using the CVD method. However, the CVD method is preferred over chemical grafting due to its versatility, controlled growth, and high purity. The use of an inorganic catalyst source such as Fe, Co, and Ni could be highly promising for growing CNTs with well dispersed, highly dense, and well-incorporated carbon fibers [102,103]. CNTs can act as bridges adjacent carbon fibers, thereby forming electrical and thermal percolation pathways within the ply and interlaminar region of composites. However, growing CNTs on carbon fibers by means of the CVD technique substantially decreases the initial mechanical properties of fiber composites and significantly degrades fiber properties due to the high synthesis temperature and/or heat treatment of cleaning acid [104-107]. Hence, growing CNTs on carbon fiber surface at the low-temperature process could maintain or enhance mechanical properties

In this work, the direct growth of CNTs on carbon fiber surface means that they can be grown at lower normal synthesis temperatures in the CVD process. Carbon sources, catalysts, and carrier gases are needed to adjust and investigate the most suitable parameter for growing CNTs in such a low-temperature environment. The process allows the catalyst to diffuse into catalyst particles and carbon fiber substrate even at a low temperature, while the carrier gas carries the evaporated liquid carbon precursor for the growth of high crystalline CNTs. In the following, a repeatable and scalable process for growing CNTs on carbon fiber surface was revealed in visual inspections using SEM images based on the growth mechanism. Then, each step of CNT synthesis will be demonstrated, together with numerous sampling inspections to manifest the morphology and quality of CNTs.

3.1 Preparation of carbon fiber substrates

CNTs were directly grown on carbon fiber fabric substrate to create fuzzy fiber using the floating catalyst-CVD method as demonstrated in Figure 3-1. Figure 3-1(a) presents an initial CVD process set-up. The liquid carbon source was located in the tube and was heated by heating tape. The limitations of this set-up were the insufficient carbon source together with an unstable temperature of heating tape. Therefore, the final set-up was developed as shown in Figure 3-1(b). An adequate liquid carbon precursor was heated using a heating pot with a water bath offering temperature stability during the process of CNT growth.

Plain weave carbon fiber fabric T300B from Sigmatex Composite Materials Company Ltd., containing 3000 filaments per tow was used as a substrate for growing CNTs. The thickness and density of woven carbon fiber sheets were 0.22 mm and 199 g/m^2, respectively. Samples were cut into 150 mm x 100 mm from as-received carbon fiber fabric. Chemical surface treatment was performed on the carbon fiber wafer to delicate the effects of a different aspect of the CNT growth process on carbon fiber. Carbon fibers were first cleaned with acetone for 15 minutes to remove sizing on the surface, followed by ethanol bathing for 15 minutes, and drying, and then subsequently coated with a catalyst.

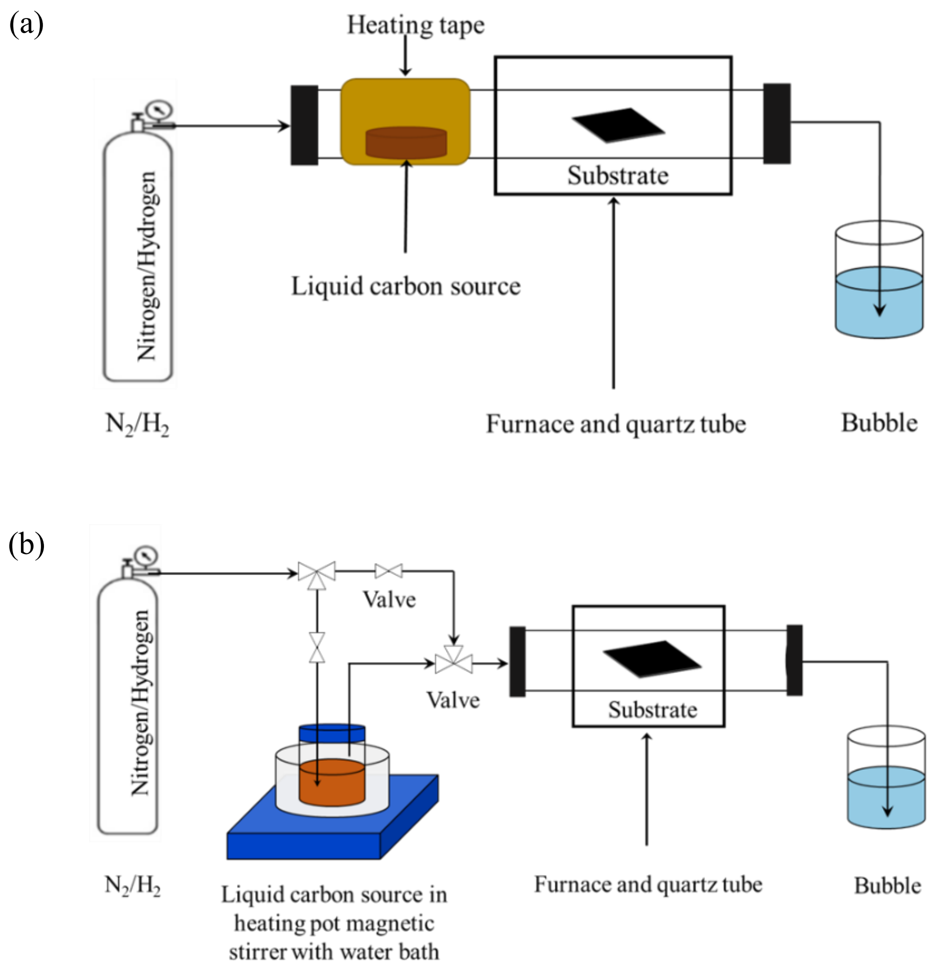

Figure 3-1. Schematic diagram of the floating catalyst-CVD method used for CNT synthesis (a) first set-up and (b) final set-up.

There are two different processes, namely dip coating and sputter deposition method, to deposit catalyst onto the wafer surface. Samples were prepared by dip-coating and the use of ferrocene ($C_{10}H_{10}Fe$), cobalt(II) acetate ($Co(OAc)_2\cdot 4\ H2O$), and nickel(II) acetate tetrahydratecatalyst ($Ni(Ac)_2.4H_2O$) as the precursors of iron, cobalt, and nickel as the catalyst, respectively. The solution was prepared by dissolving catalyst in different solubilities such as toluene (C_7H_8), and dimethylformamide (DMF, C_3H_7NO) for dip-coating technique. On the other hand, the various thickness film of nickel (Ni) catalyst was deposited onto carbon fiber fabric using a sputter deposition method. The catalyst-coated substrate was then subsequently loaded into a tubular reactor to grow CNTs on one side of a carbon fiber surface using the floating catalyst-CVD method as shown in Figure 3-1(b). The reactor was purged by flushing with nitrogen and hydrogen (N_2/H_2) carrier gas to release residual gases in the quartz tube. The temperature of the furnace was increased to 400 °C under the N_2/H_2 environment at the rate of 10 °C/min for 10 minutes. The heat reduced nickel oxides and started the dewetting process so the thin Ni film was broken into nanoparticles. After the furnace was heated to a sufficient reaction temperature (550 °C and 750 °C) at the rate of 10 °C/min, a mixture of liquid carbon source was delivered through a flow meter system with the N_2/H_2 process gas. The parametric details such as carbon sources, catalysts, and other parameters will be discussed as follows. When the decomposition of the carbon precursor took place, CNT had grown on the catalyst particle that can locate at the top or bottom of growing CNT in the reactor as shown in Figure 3-2. At the end of the reaction, carrier gas was turned off and the furnace was allowed to cool down to room temperature.

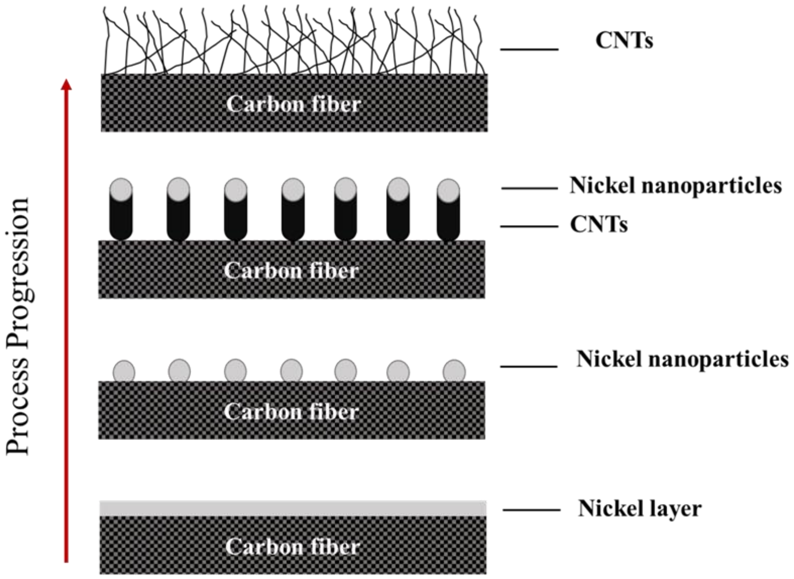

Figure 3-2. Overview of CNT synthesis: catalyst deposition, reduce catalyst film to nano-particles, and CNT growth.

3.2 Parametric study of growing CNTs on carbon fiber surface

There are many limitations of growing CNTs on carbon fiber surface due to unfavorable catalyst-carbon interactions, suitable processing temperature, and gas environment. The key parameters governing the morphology of CNTs grown directly on carbon fiber fabric are recognized to be able to control and acquire suitable CNT architecture on the fiber surface. Carbon fiber T300 was obtained from Sigmatex with 7 μm filament in diameter. Fibers were woven into a 0°/90° plain weave pattern with a density of 199 gsm and 93% carbon. The prepared fibers with catalyst were loaded into a CVD furnace system with different parameters. The diversified carbon sources, method, and amount of catalyst deposited on the fiber surface, carrier gas flow rate, processing time duration, temperature, and location of the substrate in the tube could affect the CNT morphology. At least three samples were fabricated under each combination of factors to confirm the reliability of the CNT growth method. Each sample was visually determined by Field Emission Scanning Electron Microscope (SEM) and Transmission Electron Microscope (TEM) images across its area at a minimum of three different locations.

3.2.1 Effect of methane carbon source

The dip-coated method was used for catalyst deposition. The catalysts, namely, ferrocene, nickel acetate, and cobalt acetate, were separately dissolved in acetone, followed by sonicated in an ultrasonic bath for 30 minutes. The catalyst precursor of 0.5 g was used in 10 ml solvent. Prepared sizing carbon fibers were dipped into the solvent and then dried in the oven for 3 hours at 60 °C to evaporate acetone. The different temperature (750 °C, 850 °C, and 950 °C), growing duration (30 mins, 60 mins, 120mins), and mass flow rate of carrier argon/hydrogen gas (50 sccm, 75 sccm, 100 sccm) were attempted to grow CNTs on carbon fiber. Unfortunately, CNTs were failed to grow due to the low content of carbon in CH_4 due to the high pyrolysis temperature range of 1,000-1,200 °C. The effect of methane gas carbon source on carbon fiber fabric is shown in Figure 3-3. Other organic liquid carbon sources were, therefore, resolved to use replacing methane gas because of limited facilities.

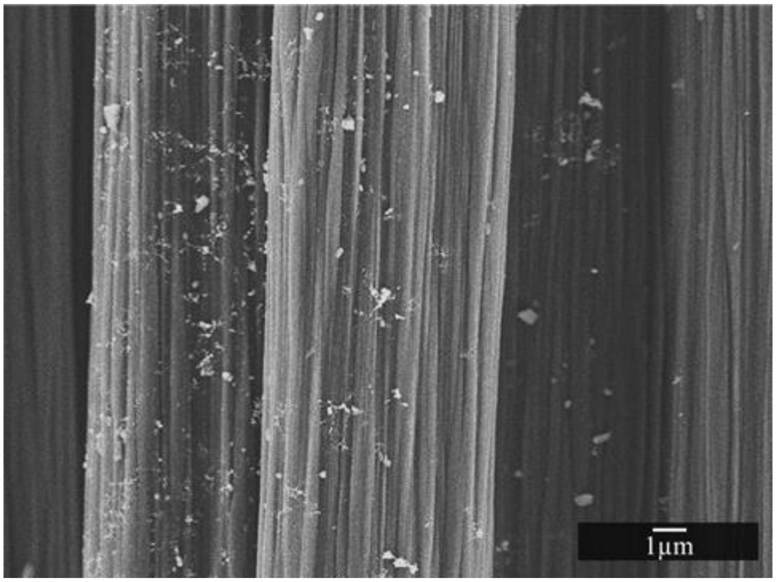

Figure 3-3. SEM image of the CNT growth using methane as a carbon source at 750 ℃.

3.2.2 Effect of toluene carbon source

In the case of liquid carbon sources, two catalysts were inspected with a fixed duration of a growth period, a mass flow rate of carrier gas (nitrogen/hydrogen), and temperature that was 30 minutes, 50 sccm, and 750 ℃, respectively. The furnace tube diameter was 5 cm. The schematic CVD set-up can be observed in Figure 3-1(a). Ferrocene ($Fe(C_5H_5)_2$) and nickel(II) acetate tetrahydrate ($C_4H_6NiO_4.4H_2O$) were chosen as the catalyst. Figure 3-4 shows the synthesized CNTs on different catalytic nanoparticle deposition (Fe and Ni) with toluene carbon sources, respectively. The highly-dense growth and long carbon nanotube were presented by the toluene precursor in both catalysts because of high carbon content. Toluene is, however, harmful to human bodies so other liquid precursors were inspected.

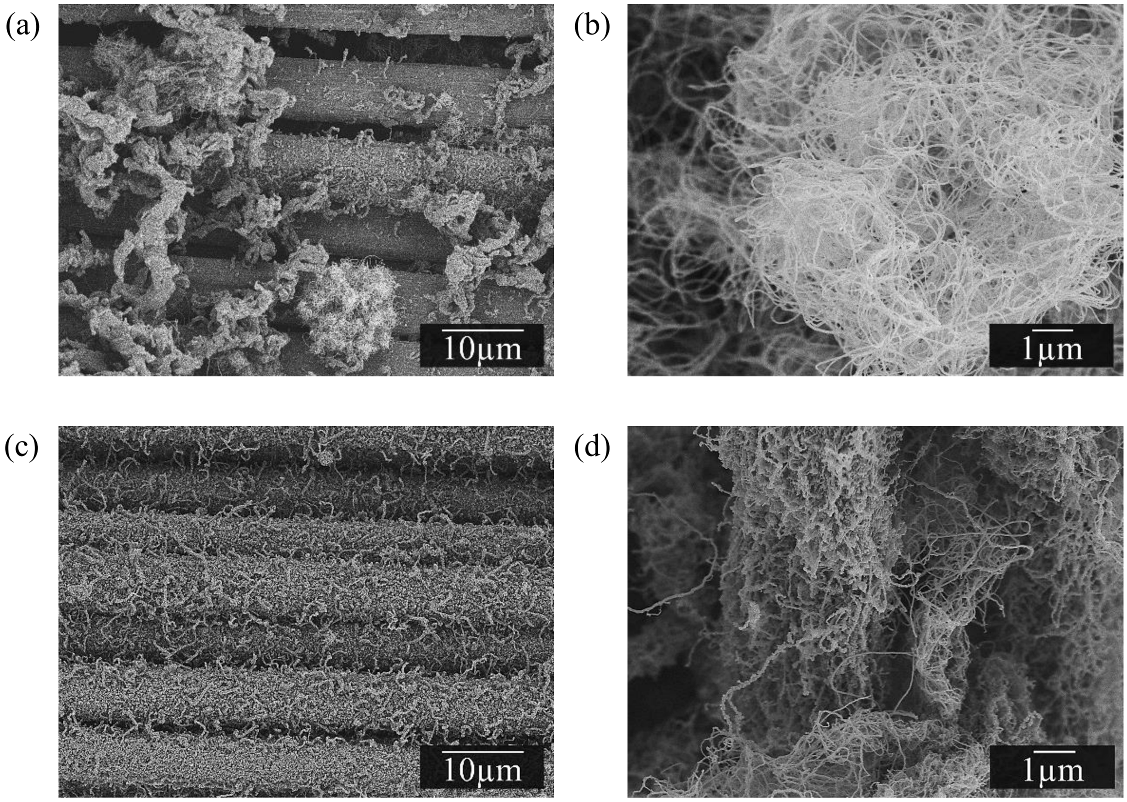

Figure 3-4. SEM images of the CNT growth using toluene as a carbon source at 750 °C with low (left) and high (right) resolution (a,b) ferrocene and (c,d) nickel(II) acetate tetrahydrate.

3.2.3 Effect of ethanol carbon source

All parameters were set as same as growing CNTs with a toluene precursor at 750 °C. To achieve the desired density and morphology of the CNT growth, the effect of diverse parameters, including catalysts, Ni film thickness, and carbon source enhancer were determined as summarized in Table 3-1.

Table 3-1. Parametric study of growing CNTs on carbon fiber surface at 750 °C.

Parameters	
Catalysts	- Ferrocene ($C_{10}H_{10}Fe$) - Cobalt(II) acetate ($Co(OAc)_2 \cdot 4\ H2O$) - Nickel(II) acetate tetrahydratecatalyst ($Ni(Ac)_2.4H2O$) - A mixture of cobalt(II) acetate and nickel(II) acetate tetrahydratecatalyst - Nickel (Ni) sputtering thin film
Thickness of Ni layer [nm]	10, 20,40
Carbon source enhancer	DMF

3.2.3.1 Effect of different catalysts by traditional dip-coating method

Figure 3-5 shows the successful CNTs grown on carbon fiber fabric with various types of catalytic nanoparticle deposition using ethanol carbon precursor. The catalyst solution was prepared by 0.8 g ferrocene ($Fe(C_5H_5)_2$) in 10 ml toluene (C_7H_8). On the other hand, 0.5 g cobalt acetate ($Co(CH_3COO)_2.4H_2O$), 0.5 g from a mixture of two equal cobalt(II) acetate and nickel(II) acetate tetrahydrate, or 0.5 g nickel(II) acetate tetrahydrate ($C_4H_6NiO_4.4H_2O$) were separately dissolved in 10 ml dimethylformamide (DMF, C3H7NO). The low density of CNTs was shown, when ferrocene, cobalt (II) acetate, and the mixture of cobalt (II) acetate with nickel(II) acetate tetrahydrate were deposited as a catalyst with an ethanol-based carbon source as displayed in Figures. 3-5(a) to 3-5(f). Nickel (II) acetate tetrahydrate catalyst shows, however, more dense CNT growth compare to other catalytic materials that can be observed in Figures. 3-5(g) and 3-5(h).

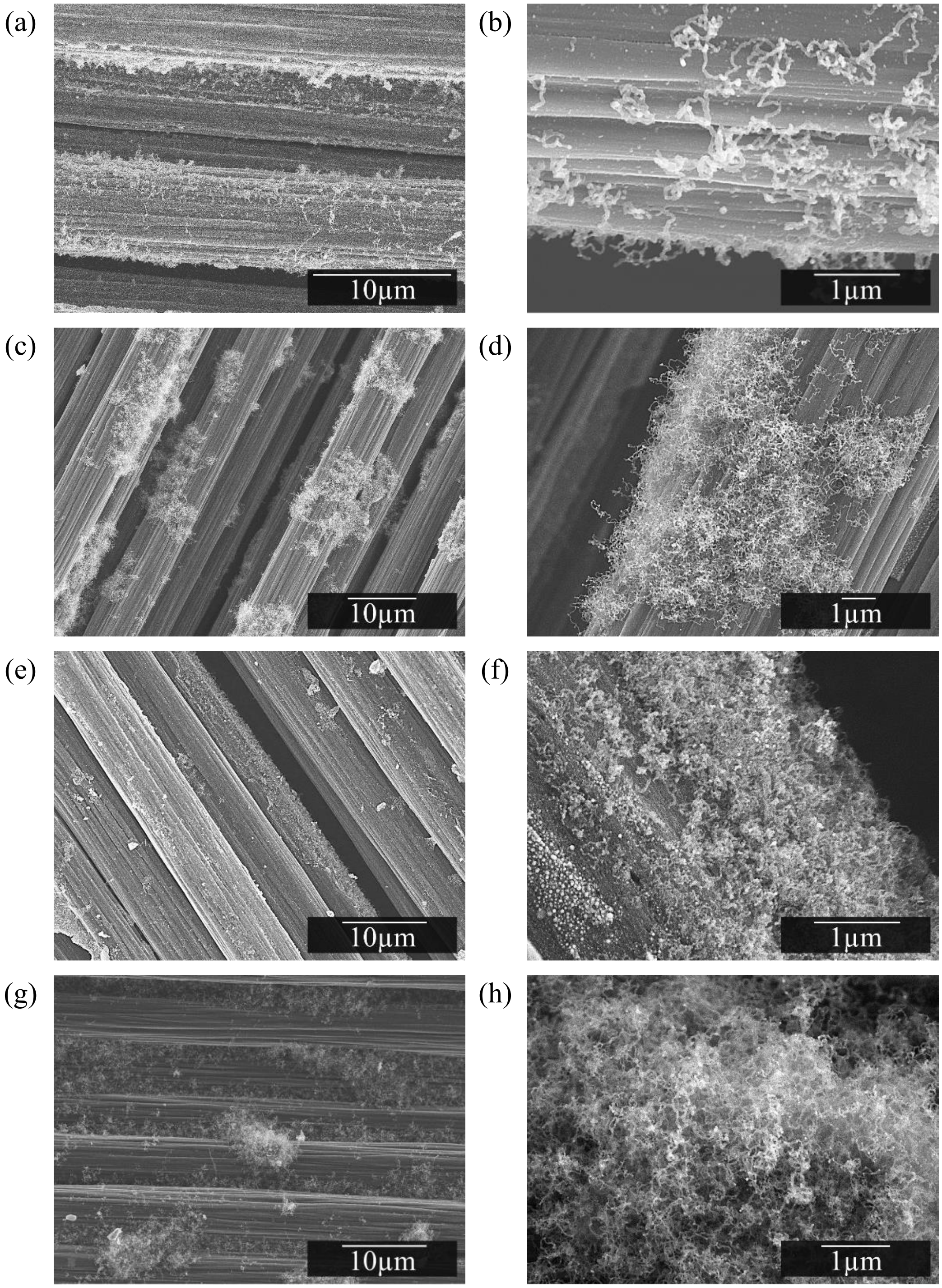

Figure 3-5. SEM images of the CNT growth at 750 °C with low (left) and high (right) resolution (a,b) ferrocene, (c,d) cobalt(II) acetate, (e,f) the mixture of cobalt(II) acetate and nickel(II) acetate tetrahydrate, and (g,h) nickel(II) acetate tetrahydrate.

3.2.3.2 Effect of Nickel (Ni) film thickness by DC magnetron sputtering technique

In the case of the sputter deposition method, Ni catalyst was deposited on the surface of carbon fiber fabric using a magnetron sputtering (Denton Explore-14) under an argon atmosphere ($8.7x10^{-7}$ Torr pressure, 150W of RF power supplies). The catalyst-coated fiber with different thicknesses of the Ni layer was subsequently placed into a tabular reactor to grow CNTs. Figure 3-6 shows homogenously and densely covered of long CNTs grown on carbon fiber by sputtering method compared with the CNTs grown by traditional dip-coating technique. This is because the DC magnetron sputtering technique yielded a continuous and uniform distribution of nickel film. It is considered that the density of CNTs can be directly related to carbon precursors and catalytic materials. In addition, the density and length of CNTs were increased by the thicker Ni layer. The coverage of CNTs was really poor in 10 nm thick Ni layer, while 40 nm thick Ni layer showed very dense CNT coverage on carbon fiber surfaces. The best CNT coverage was revealed in 20 nm thick Ni film compared with 10 and 40 nm thick Ni layer.

The observed trend of CNT density and coverage can be correlated to the size of Ni catalytic nanoparticles that could affect the diameter of CNTs during the annealing stage. A larger diameter of CNT can be observed in the thicker Ni layer as shown in Figures. 3-6(d) and 3-6(e). According to the 40 nm thick Ni layer, there were too many large diameters of CNTs grown which imbricated onto each other. The clusters coarsened into too small or too large particles creating non-uniform CNT growth on carbon fiber surfaces caused by the thinner or thicker Ni catalyst film, respectively. Therefore, an appropriate thickness of the Ni catalyst layer is required to synthesize the uniform and suitable diameter of CNTs grown on fiber cloth.

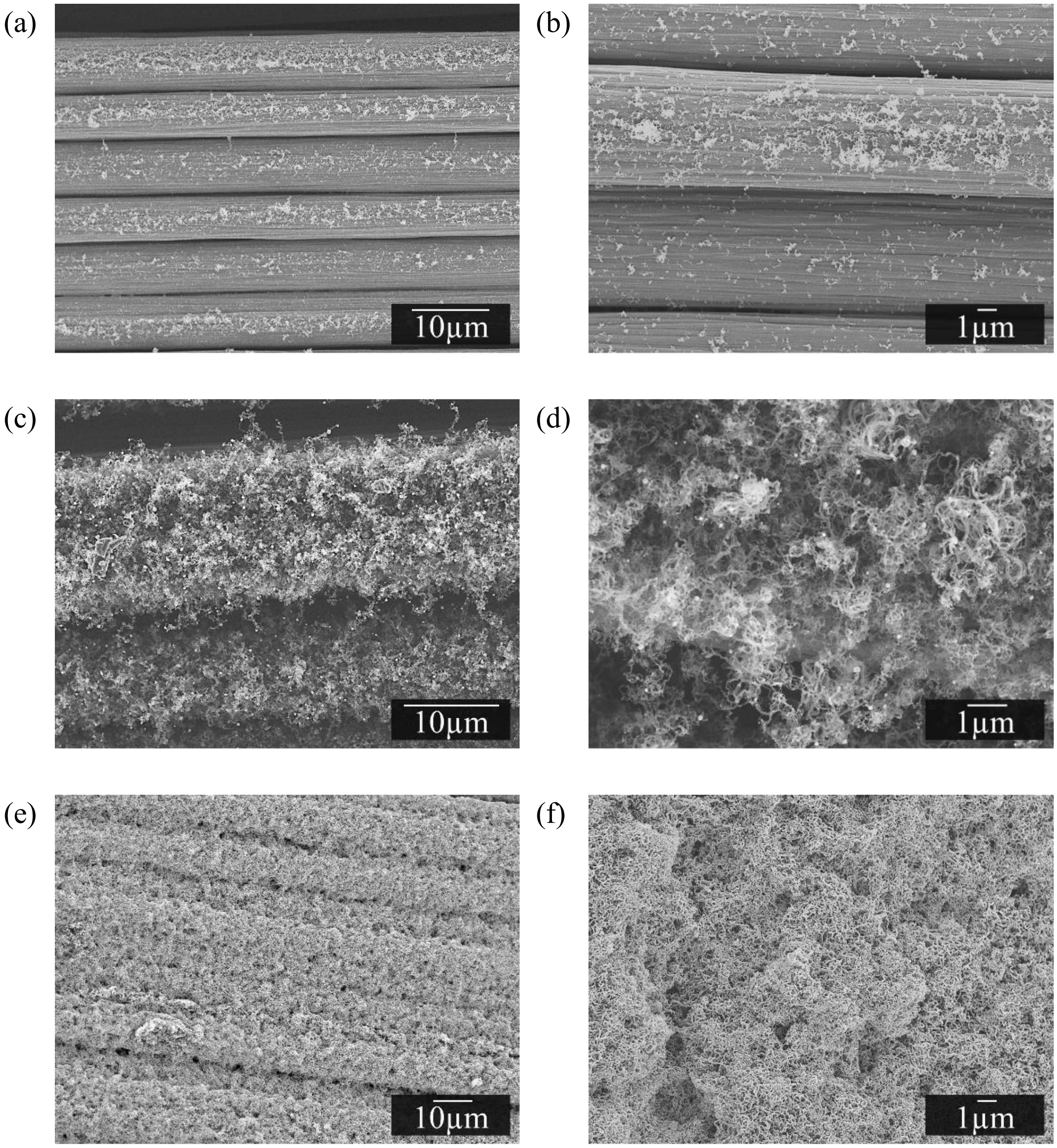

Figure 3-6. SEM images of the CNT growth on different thickness of Ni layer with low (left) and high (right) resolution (a,b) 10 nm, (c,d) 20 nm, and (e,f) 40 nm.

3.2.3.3 Effect of DMF enhancer

The effect of DMF as a precursor enhancer was justified to further improve the morphology of CNTs. The high carbon content organic DMF was added to an ethanol-based carbon source. The electrical conductivity of nitrogen-doped (N-doped) CNTs is higher than conventional CNTs [108]. The coverage of CNTs grown on 20 nm Ni coated-carbon fiber with DMF carbon source enhancer was much denser than that of a similar sample with a non-DMF enhancer as displayed in Figure 3-7. Therefore, the DMF solution can be used to increase the density, coverage, and electrical conductivity of CNTs on fiber surfaces.

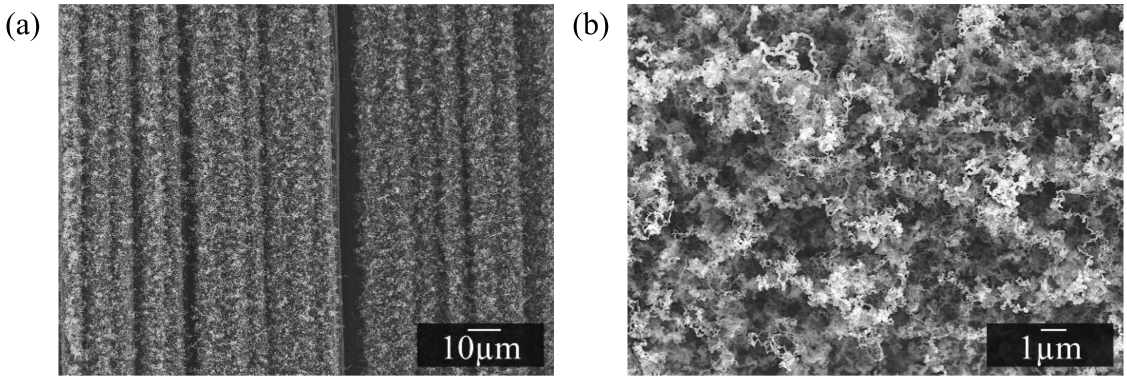

Figure 3-7. SEM images of the CNT growth with DMF enhancer in ethanol (a) low resolution and (b) high resolution.

3.2.4 Effect of temperature

The effect of processing temperature to synthesize CNTs on carbon fiber is summarized in Figure 3-8. Other parameters were still unchanged. Figure 3-8c demonstrates the highly-dense growth of CNTs on Ni-coated carbon fiber at 750 ℃ due to the higher thermal decomposition of liquid carbon source (a mixture of ethanol and DMF). However, the high processing temperature above 650 ℃ in the CVD process might damage the carbon fiber substrate. The lower temperature (550 ℃) of CNT synthesis was required to prevent mechanical property degradation in carbon fiber clothe. Even though the CNT length was not long which might result from the incomplete decomposition of carbon precursor compared with CNTs grown at 750 ℃, the better alignment of CNT coverage on carbon fiber can be noticed in Figure 3-8(a). The tendency of CNT length seemed to reduce due to the decrease in growth temperature in the CVD method. Therefore, adjusting other parameters is required for growing CNTs at 550 ℃ to acquire the optimum CNT morphology.

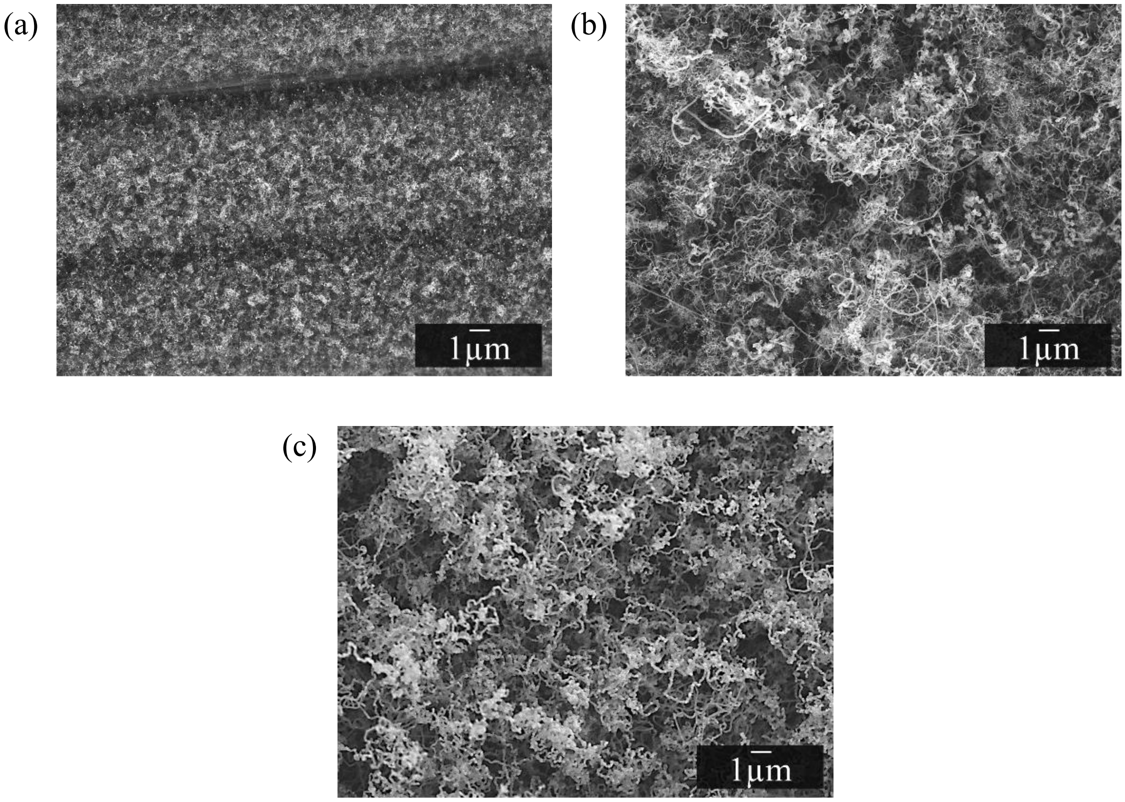

Figure 3-8. SEM images of the CNT growth with different processing temperatures (a) 550 ℃, (b) 650 ℃, and (c) 750 ℃.

3.2.5 Effect of different parameters at 550 °C

Five factors, including Ni film thickness, carbon sources, carrier gas flow rate, sample location, needed to be adjusted to improve the morphology and coverage of CNTs grown on carbon fiber cloth, as listed in Table 3-2. The Ni thin film layer thickness could influence the amount of Ni nanoparticles deposition resulted in different lengths and densities of CNT. CNTs were grown in the varieties of carbon sources and carrier gas flow rate to observe their structure, proportion, and density effects due to the thermal decomposition. Then, the position of the sample in the quartz tube can also be an essential condition due to the different thermal decomposition of carbon sources along the tube.

Table 3-2. Parametric study of growing CNTs on carbon fiber surface at 550 °C.

Parameters	**Values**
Thickness of Ni layer [nm]	10, 20, 40
Carbon sources	Acetone, ethanol-based with DMF enhancer, and ethanol-based with IPA enhancer
Gas flow rate [sccm]	60, 90, 120
Sample location at the center furnace as reference line [cm]	0, 10-12, 20-22

3.2.5.1 Effect of Ni layer thickness

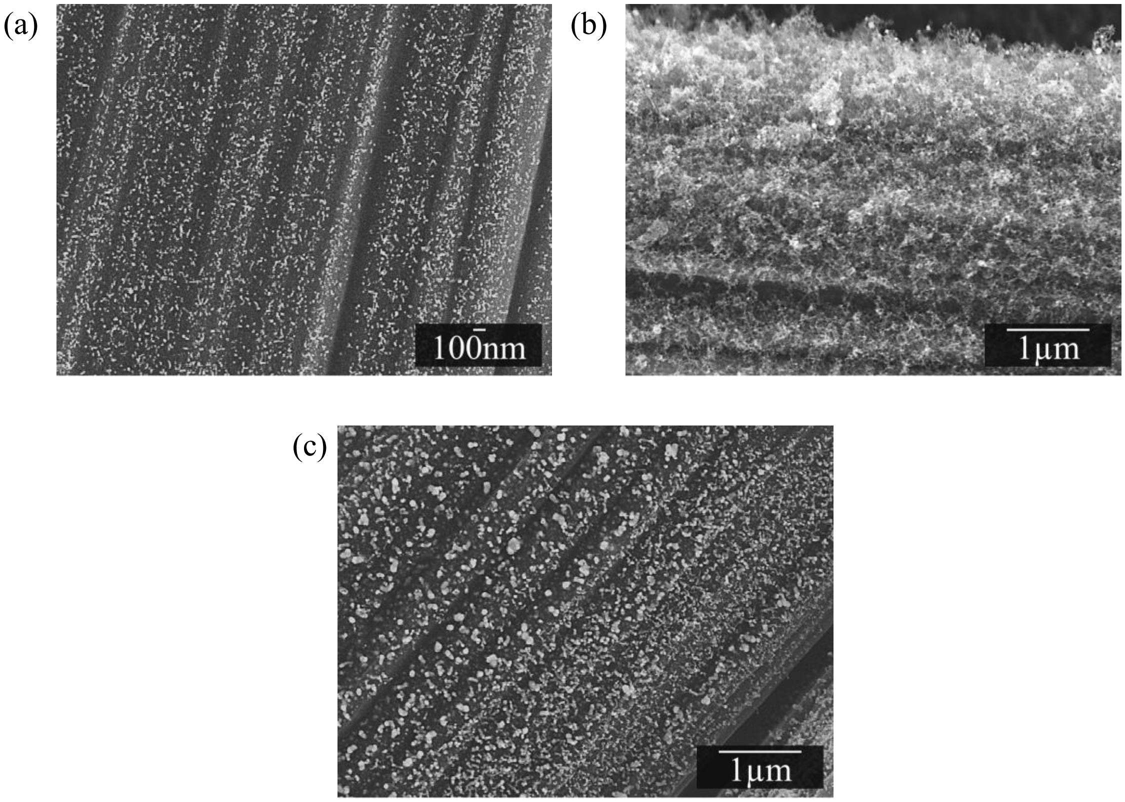

Figure 3-9. SEM images of the CNT growth with different thickness of Ni layer (a) 10 nm, (b) 20 nm, and (c) 40 nm.

The continuous and uniform nickel thin film was formed by the DC magnetron sputtering method so homogeneous coverage of CNTs can be synthesized on the carbon fiber surface. The effect in different thicknesses of nickel layer (10 nm, 20 nm, and 40 nm) was demonstrated to acquire an appropriate density of CNTs grown on carbon fiber surface with ethanol carbon source at 550 °C as illustrated in Figure 3-9. A short and poor of the CNT growth can be observed on the carbon fiber surface with a 10 nm thick Ni layer. The average diameter of CNTs was increased in the case of a 40 nm thick Ni catalyst layer. However, the catalyst nanoparticles were too big so small amounts of CNTs could be grown showing poor density and non-uniform CNT growth. Results reveal that 20 nm Ni layer was the most suitable film thickness to grow the uniform coverage of CNTs in both 550 °C (Figure 3-9(b)) and 750 °C (Figures. 3-6(c) and 3-6 (d)).

3.2.5.2 Effect of different carbon source

Figure 3-10 displays the effect of different liquid carbon sources. CNTs were grown in a variety of carbon sources with similar catalytic nanoparticle deposition to observe their morphology and density effects. All samples were placed in the center of the furnace tube. Although acetone precursors could enhance the CNT growth rate, the size and length of CNTs were vastly disparate. A DMF enchantment in ethanol-based carbon source could synthesized uniform but short CNT growth. Another high carbon content of IPA was selected to enhance ethanol carbon precursor. It is evidently shown that the IPA enhancer could increase both the length and diameter of CNT growth, but the size of CNTs is not uniform. Therefore, a mixture of ethanol-based with DMF carbon precursor was a suitable carbon source to grow high density and satisfactory coverage of CNTs on the carbon fiber surface.

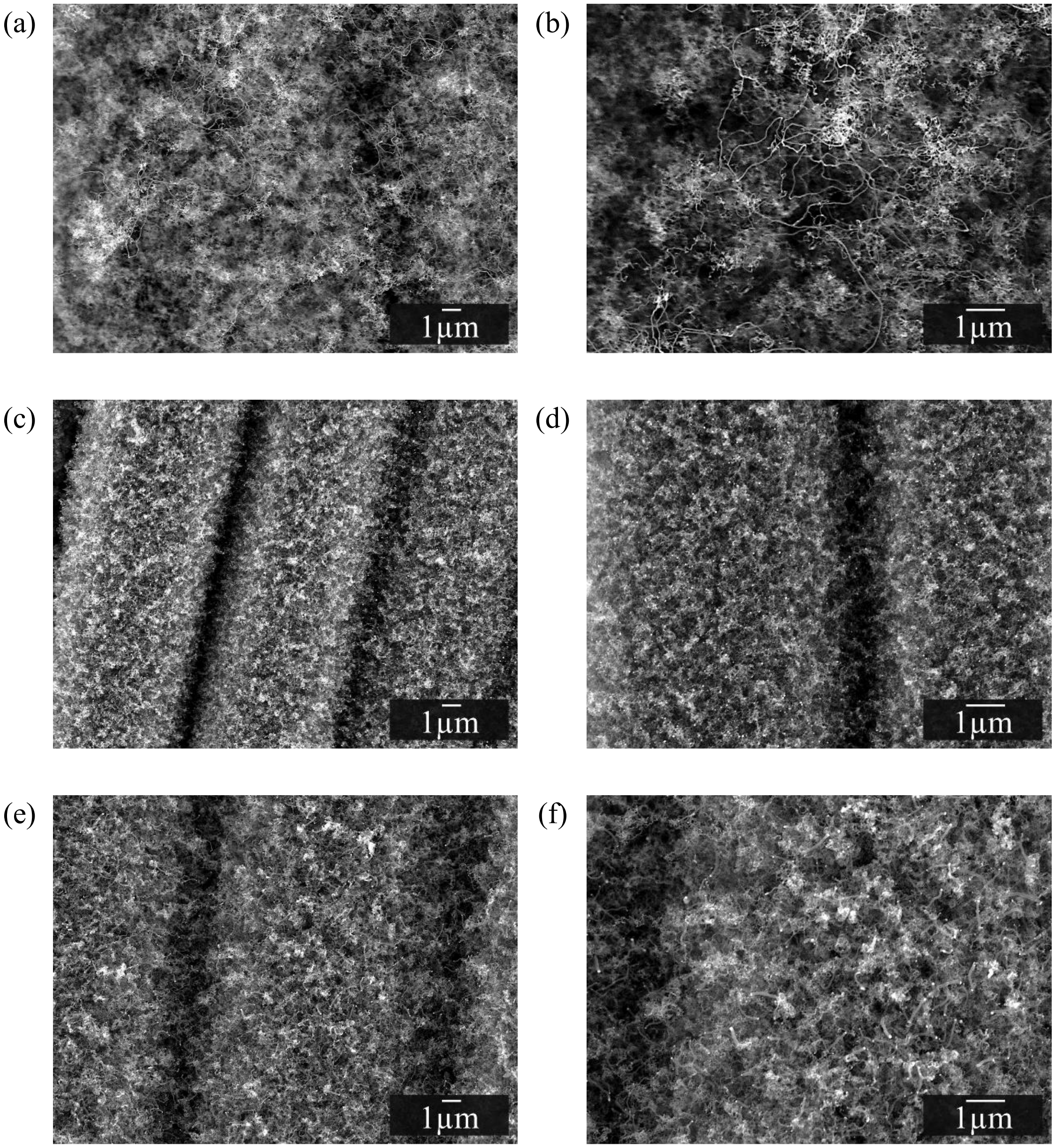

Figure 3-10. Effect of different carbon sources at 550 °C with low (left) and high (right) resolution (a,b) acetone, (c,d) ethanol based with DMF enhancer, and (e,f) ethanol-based with IPA enhancer.

3.2.5.3 Effect of carrier gas flow rate in the furnace tube

The effect of carrier gas flow rate is summarized in Figure 3-11. An optimum length and uniform coverage of CNT growth can be observed on samples with the carrier gas flow rate at 90 sccm and 120 sccm. Even though the gas flow rate at 60 sccm can successfully synthesize CNTs on the carbon fiber surface, the short length of CNTs was displayed. An inadequate speed of gas flow rate may result in poor density and the short length of the CNT growth. This is because a suitable gas flow rate velocity of carbon-rich precursors could lead to an increase of carbon dissolution into Ni nanoparticles to enable the growth of CNTs. The excessive use of gas flow speed, however, may also provide a reverse effect because the carbon source that interacts with Ni nanoparticles catalysts could not be effectively dissolved minimizing CNT growth density. Therefore, a suitable carrier gas flow rate is required to acquire the optimum size and uniform coverage of CNT growth on carbon fiber cloth.

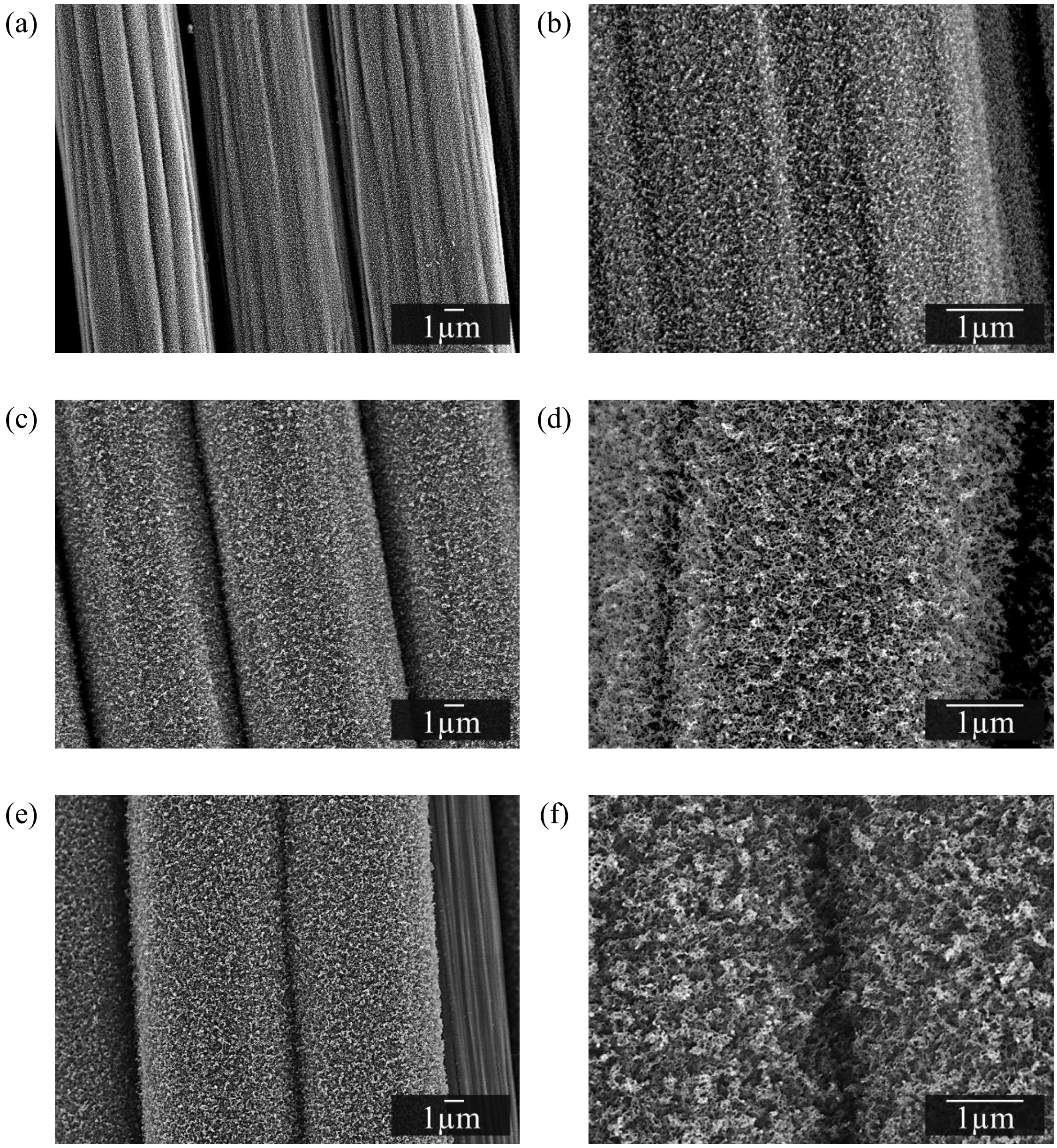

Figure 3-11. Effect of carrier gas flow rate in the furnace tube on CNT growth at 550 ℃ (a,b) 60 sccm, (c,d) 90 sccm, and (e,f) 120 sccm.

3.2.5.4 Effect of sample position in the furnace tube

It is experimentally demonstrated that sample location in the tube furnace had greatly influenced the CNT growth characteristics due to the thermal decomposition of gas concentrations and variation of temperature in the tube as shown in Figure 3-12. These mechanisms may depend on the interaction between catalyst and carbon fiber substrates. Prepared specimens, which were coated with 20 nm Ni layer thickness, were loaded in the 110 cm inner diameter wide furnace tube. The different positions were inspected from -20 cm to +20 cm marks, with 0 cm indicated as the center of the tube. According to our CVD system, samples at 0 cm and around 10-12 cm in the furnace provided great coverage and morphology of CNTs as presented in Figures. 3-12(a) and 3-12(b). Further placing the sample at around 20-22 cm of the tube, however, displayed a slightly shorter in the length of CNTs. It may cause by an inadequate intermediate gas concentration for CNT growth when the samples were located further downstream. Since reactants were thermally decomposed along the length of the quartz tube, which is hypothesized to occur. Then, this area was in a less favorable position to grow an appropriate size of CNT. Therefore, CNT morphology on carbon fiber can be affected by the sample placement position due to the reactant mixture decomposition into numerous active species at high-temperature. The center of the furnace is the hottest region and falls off towards the ends of the heated zone, where depends on the insulation placement.

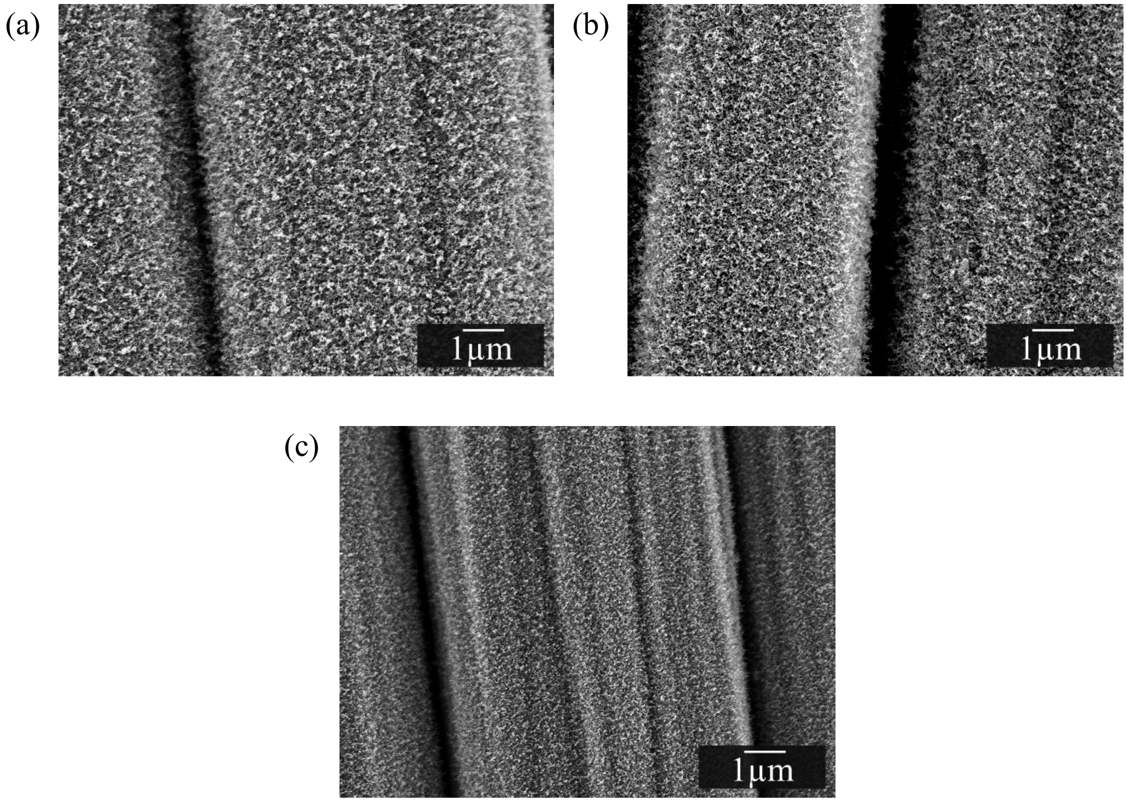

Figure 3-12. Effect of sample position in the furnace tube on CNT growth at 550 °C (a) 0 cm, (b) 10-12 cm, and (c) 20-22 cm.

3.3 The morphology of CNT growth on carbon fiber surface

Numerous parameters to synthesize CNTs were adjusted to acquire the desired CNT morphology. The optimum floating catalyst-CVD method for growing CNTs on the carbon fiber surface is described as follows. Catalyst-coated carbon fibers can be prepared by deposited 20 nm thick Ni layer on the surface of carbon fiber using DC magnetron sputtering process. The catalyst-coated substrate was then loaded into the center of a furnace tube to grow CNTs on one side of the carbon fiber surface as illustrated in Figure 3-1(b). The tube was purged by N_2/H_2 carrier gas (90 sccm) for 1 hour to remove residual gas inside the quartz tube. When the temperature was heated to 400 ℃ at the rate of 10 °C/min, the dewetting of nickel thin films was started to anneal and then broke up the layer into isolated islands (Ni nanoparticles) on the surface of the substrate for 10 minutes. CNTs began to synthesize on the carbon fiber substrate by the delivery of 90 sccm carbon precursor (ethanol-based with DMF enhancer) at 550 ℃. The vaporous carbon source was injected into the reactor by introducing N_2/H_2 carrier gas into a glass bottle of the liquid carbon precursor solution. The vaporous carbon source was turned off after 30 minutes of growth duration. Then, the reactor was allowed to cool down to room temperature under the N_2/H_2 gas condition.

After CNT growth, no further modification or functionalization was applied to CNTs. Each carbon fiber cloth was measured using a microbalance when they were coated with Ni film and after CNTs grew. CNTs were inspected by field emission scanning electron microscope (FE-SEM) and transmission electron microscope (TEM) to confirm the growth of CNTs throughout the carbon fiber surface and to analyze their morphology and structure. Then, the density and quality of CNTs can be revealed using thermogravimetric analysis (TGA) and Raman spectroscopy.

3.4 Characterizations

3.4.1 Scanning electron microscope (SEM)

The morphology of the fuzzy fiber was investigated by a HITACHI SU8010 field emission scanning electron microscope (FE-SEM). The use of acceleration voltage was 5 kV. FE-SEM is used to image the specimens by scanning their surface with electrons beam in a raster scan pattern offering high resolution and large depth of field. When the electron beam of the FE-SEM machine has interacted with the electron in the sample, it produces the secondary electrons and backscattered electrons that contain all the information of surface topography and physical properties of each sample. CNTs can be observed to be wavy and non-directionality due to the large aspect ratio of CNTs as shown in Figure 3-13. Ni nanoparticles reveal at the CNT tips, indicating tip-growth.

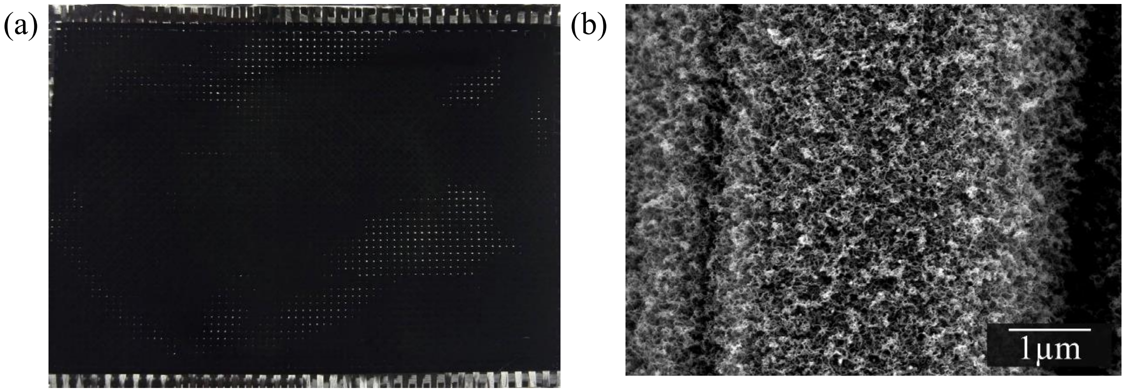

Figure 3-13. Images of CNT growth on carbon fiber fabric (a) optical image and (b) SEM image.

3.4.2 Transmission electron microscope (TEM)

CNTs were further characterized by a JEOL JEM-2011 transmission electron microscope (TEM) at an accelerating voltage of 100 kV. TEM is based on imaging elastically scattered and transmitted electrons from an ultrathin specimen that is ideally less than 100 nm in thickness. The operation of the electromagnetic lens allows imaging of an object in the corresponding image plane by focusing an ultra-thin beam of electrons beginning with different directions from individual object points to the corresponding image point. TEM samples were prepared by dropping individual growth CNT carbon fiber solutions onto a copper grid and drying them in the ambient environment. This suspension can be prepared by immersing fuzzy fiber into ethanol and sonicated for 15 minutes. TEM images were used to verify their parallel wall structure and to inspect the number of walls to confirm the type of CNT growth on carbon fiber substrate. They verified the parallel wall structure, which was approximately 15-20 walls. The diameter and distinct multiple wall constructions were consistent with multi-walled carbon nanotubes (MWNTs). The average length, inner diameter, and outer diameter were approximately 4 µm, 10 nm, and 20 nm, respectively as illustrated in Figure 3-14.

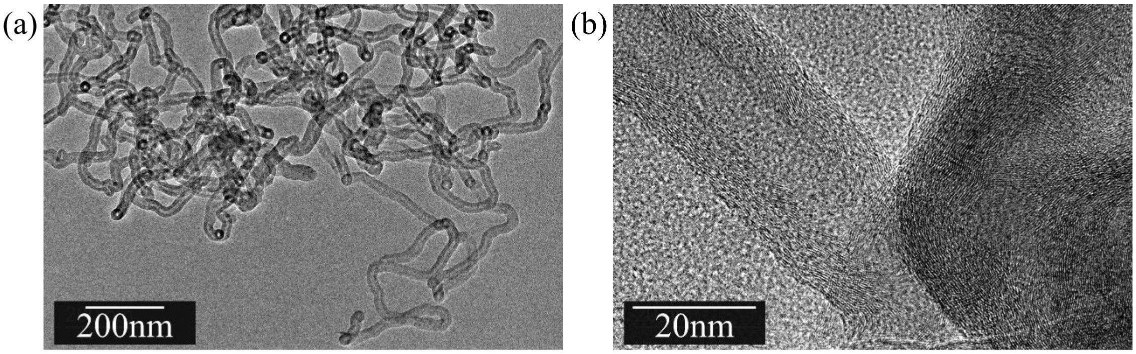

Figure 3-14. TEM image of MWNT growth on carbon fiber fabric (a) low resolution and (b) high resolution.

3.4.3 Thermogravimetric analysis (TGA)

The mass density of CNTs grown on carbon fiber surface can be characterized using Mettler Toledo TGA/DSC3+ on fiber samples in a platinum crucible in a flowing air atmosphere of 20 cm^3/min from 30 to 950 °C at a heating rate of 20 °C/min. Figure 3-15(a) shows the TGA and DTG curves of fuzzy fiber composites under the oxygen-enriched atmosphere. There was negligible weight loss in the temperature range between 300 ℃ and 400 ℃, which was attributed to the negligible amorphous carbon in the samples. A notable weight loss in the DTG curve of the fuzzy fiber sample can be confirmed at around 780 °C, indicating the complete oxidation of CNTs to gaseous products in the oxygen condition. The fuzzy fiber composites were thermally stable from 0°C to 600 °C and then stability significantly decreased in the temperature range between 600 °C and 900 °C, probably due to the thermal decomposition of aromatic rings in carbon fibers. This phenomenon indicated that the composite was completely decomposed at around 600 °C and 900 °C under an oxygen environment. However, the temperature range was still lower than that of the CFRP composites shown in Figure 3-15(b) due to the effect of high-temperature CNT growth that partially degraded the carbon fiber substrate. It was also observed that both composites had remaining masses of less than 1%, resulting from impurities. According to Figure 3-15(b), the typical CNT growth temperature over 750 °C may degrade carbon fibers, which probably causes a deleterious effect on the resulting mechanical performances of the whole carbon fiber composites. However, it should be noted that the air atmosphere is much more aggressive than the atmosphere in the furnace when the floating catalyst-CVD method is used.

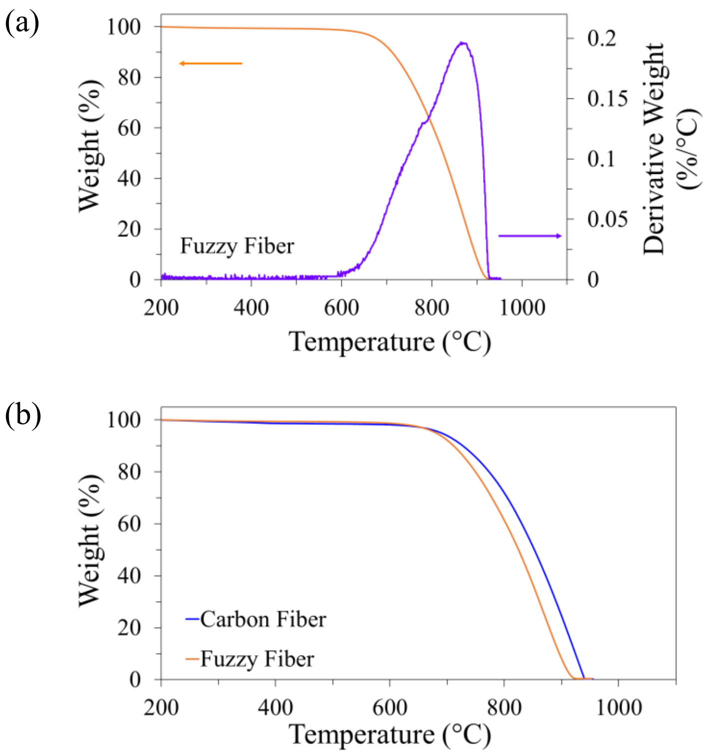

Figure 3-15. TGA data of (a) fuzzy fiber and (b) sized carbon fiber and fuzzy fiber under oxygen condition.

According to the observed CNT morphology, the average length and diameter of CNTs can be observed by TEM imaging. The area density of CNTs can be calculated according to the relations between the density of CNTs and their geometrical characteristics such as inner diameter, outer diameter, length, and wall number [109]. Assuming all CNT tubes had the same mass, m (g), average diameter, d (nm), length, l (nm), and the number of walls, n (tubes) on a support area, A (cm^2) so the population density of CNTs at the carbon fiber surface can be calculated [110]:

$$\frac{n}{A} = \frac{n.\ W_{MW}}{Al} \Big/ \frac{W_{MW}}{l} \tag{3-1}$$

where $\frac{n}{A}$ is the area density (tubes/cm^2), $\frac{n.W_{MW}}{Al}$ is the mass density (g/cm^3), and $\frac{W_{MW}}{l}$ is the weight gain per unit length of the tube (g/cm).

The mass density can be measured by weighing the carbon fiber surface before and after growing CNTs using a highly accurate microbalance with a resolution of 0.01 mg. The CNT wall number, length, and diameter can be observed from TEM images. The measured weight gain of CNTs grown on the carbon fiber surface, mean diameter, and mean CNT wall number can be used to derive the mass per unit length of the nanotubes. A rolled tubes of graphene is a single-walled carbon nanotube (SWCNTs) that has a specific surface area of 1,315 m^2/g so the weight of SWCNTs can be calculated from the surface area of graphene sheet as:

$$W_{SW} = \frac{1}{1{,}315}\pi l \mathrm{d} \qquad \text{(grams)} \tag{3-2}$$

The inter-chain bond length (C=C) in the curved graphene sheets is 0.1421 nm, which is similar to the planar sheet. Then, the MWCNTs are composed of concentric shells that are separated by the c-axis spacing of graphene, $d_{s\text{-}s}$, 0.34 nm so the surface area of MWCNTs is given by:

$$S_{MW} = \pi l[nd_i + 2d_{s-s} \textstyle\sum_{i=0}^{n-1} i] \quad (3\text{-}3)$$

The surface mass of each graphene is $\frac{1}{1315\times 10^{18}}$ g/nm^2, thus, the weight of MWCNTs (W_{MW}) can be calculated

$$W_{MW} = \frac{1}{1{,}315x10^{18}} \pi l[nd_i + 2d_{s-s} \textstyle\sum_{i=0}^{n-1} i] \quad (3\text{-}4)$$

The volume of a CNT (V_{MW}) is related to the outer diameter (*d_{out}*), of all n walls, with units in nm,

$$V_{MW} = \frac{\pi l d_{out}}{4} \quad (3\text{-}5)$$

The weight of the MWCNT, with units in g/nm when d_{out} is in nm. can be expressed as:

$$W_{MW} = \frac{1}{1315\times 10^{18}} \pi l\; [nd_{out} - 2d_{s-s} \textstyle\sum_{i=0}^{n-1} i] \quad (3\text{-}6)$$

which can be simplified as:

$$W_{MW} = \frac{\pi l}{1315\times 10^{18}}\; [nd_{out} - 0.34n(n-1)] \quad (3\text{-}7)$$

Thus, the mass density of MWCNTs (d_{MW}) is given as:

$$d_{MW} = \frac{w_{MW}}{v_{MW}} \tag{3-8}$$

The area under the DTG curve can provide a measure of the mass fraction in different materials. The measured mass density was between 0.16-0.20 g/cm^3. Therefore, the CNT population density on the carbon fiber surface can be calculated [109] to be in the range of 4-5×10^{10} tubes/cm^2, which is much denser than that previously reported [104]. It is believed that this simple and economic CVD method can successfully grow CNTs on carbon fibers with homogeneous coverage and high density.

3.4.4 Raman spectroscopy

The quality of CNTs is a great concern because any damages could degrade functional property in composites; however, the quantitative characterization of CNT defects is complicated. Raman spectroscopy is a powerful tool for investigating the nature of graphitic structure in carbon materials. Rayleigh scattering is the process of elastic scattering of light or other electromagnetic radiation by particles (atoms or molecules) that are much smaller than the wavelength of radiation. This scattering does not change the state of the material. This scattering can also mean that scattered light rays possess photons of energy and wavelength the same as those of incident phonon. A small fraction of scattered photons (approximately 1 in 10 million) has distinct energy and wavelength. In the case of the molecule, the incident light will interact with the electric dipole of that molecule and the photon of light can excite one of the electrons into a virtual state. Since the virtual state is unstable, the electron decays back to its lower state and releases another photon. This inelastic scattering of a photon by molecules that are excited to higher vibrational or rotational energy levels is known as Raman scattering. A fraction of incident light is scattered inelastically by the specimen so this intensity and wavelength can be measured by Raman spectroscopy. An inelastically scattered light has a different wavelength compared with the wavelength of the incident light. The energy of incident light is shifted by molecular vibrations providing inelastically scattered light with a different wavelength. The difference in energy of the incident light photon and inelastically scattered photon corresponds to the energy vibration of scattering chemical bond or molecule. This shift of energy manifests the uniqueness of different bonds and molecules in each material.

Raman spectroscopy (Renishaw with Leica DM LM) was performed using a 488 nm laser at a microscope magnification of 50 to determine the quality of the CNTs. It is a non-destructive technique that is suitable for symmetric homogeneous atomic lattice structures, including carbon fibers, graphene, and carbon nanotubes. Figure 3-16 presents the spectra of as-received carbon fiber (black curve) and fuzzy fiber (red curve). The CNTs grown on carbon fiber fabric were scanned over many regions to acquire an average surface quality of CNTs over the carbon fiber surface. The major two characteristic peaks are the defect induced double resonance band (D-peaks) and graphitic peak (G-peaks) in the carbon fiber material. The D-band, a result of disorder due to sp^3 carbon bonds indicating the presence of defects, was detected at 1,368 cm^{-1} for carbon fibers. The intensity of D-band indicates numerous defects in the synthesized material. The G band, on the other hand, indicates stretching in the graphitic lattice, showing 1,589 cm^1 in carbon fibers. It represents an in-plane vibrational mode involving *sp*^{2} hybridized carbon atoms that comprise the graphene sheet. In the case of fuzzy fiber, the D- and G-peak were located at 1,352 cm^{-1} and 1,594 cm^{-1}, respectively. A 2D-peak was also fitted because the basal planes of the carbon fiber may have been altered as a consequence of the high processing temperature during the synthesis of CNTs. This factor affected the turbostratic structure leading to a narrower 2D-peak. The 2D-peak at 2,957 cm^{-1} showed the possibility of weak carbon interlayer interactions as shown in Figure 3-16 (red curve). This 2D-band is the second order of D-band results of two-phonon lattice vibrations. It also indicates the stacking of graphitic layers within MWNTs and determined the CNTquality by comparing D- and G-peak intensity. It does not need to be activated in the vicinity of defects. The intensity ratio of D to G peaks (I_D/I_G) indicates the presence of the fraction of structural defects. Hence, a lower I_D/I_G ratio value shows higher quality and material that features minimal structural defects in the CNTs grown. The calculated I_D/I_G value of fuzzy fiber is 0.54 as shown in Table 3-3. This indicates a high quality that can be applied to composites enhancing electrical conductivity.

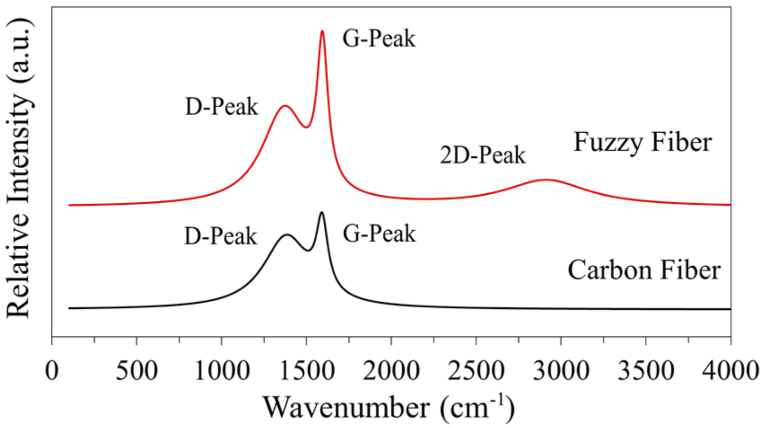

Figure 3-16. Raman spectra analysis of carbon fiber and fuzzy fiber at 488 nm excitation wavelength.

Table 3-3. The intensity ratio of I_D/I_G compared with other studies.

Method	$\frac{I_D}{I_G}$	**Ref.**
This work(488 nm)	0.58	
Growth CNTs on CF	0.87	
Pristine CF		
CVD growth CNTs on CF, 514 nm	0.4	[111]
CVD growth CNTs on CF, 514 nm	0.6	[112]
Graft CNTs on CF, 488 nm	0.74	[113]
CVD growth CNTs on CF, 532 nm	0.83	[26]
Electrophoretic deposition CNTs on CF (532 nm)	> 1	[114]

3.5 Summary

In conclusion, CNTs were successfully synthesized on the surface of carbon fiber at the low-temperature process. Carbon fiber preparation, CNT synthesis, and parametric effects of growing CNTs on carbon fiber fabrics are the major consideration in Chapter 3. Many parameters had been adjusted to achieve the desired CNT structure and quality on the surface of carbon fiber using the CVD technique. CNTs were observed their morphology, coverage, and structure by SEM and TEM images. Traditional dip coating and DC magnetron sputtering techniques were used to deposit catalysts on carbon fiber surfaces, but the sputtering method provided better density and coverage of the CNT growth. The results showed that the different catalysts and thicknesses of Ni film affected the size of catalyst nucleation resulted in the varieties of CNT diameter. Carbon sources, growth temperature, gas flow rate, and sample location were the considered parameters influencing coverage, density, and morphology of the CNT growth. Scalability was also investigated by changing the growth of CNTs into a double diameter of the quartz tube. In the larger furnace system, the visual inspections highlighted the effect of carrier gas flow rate acting on the CNT growth mechanism. Other characterization techniques, including TGA, and Raman spectroscopy were used to calculate and demonstrate the density and quality of the CNTs grown on carbon fiber.

CHAPTER 4

NANOCOMPOSITES AND COMPOSITE FABRICATION PROCESSES

Polymer nanocomposites display distinctive properties by combining the benefits of organic and inorganic nanofillers. Due to the large surface area of inorganic nanofillers, the interfacial area has vividly increased so the change of polymeric composite properties could be affected by the small concentration of inorganic nanofillers such as graphene, graphene oxide, carbon nanotubes, metal oxides (SiO_2, Al_2O_3, TiO_2), metallic group (Au, Cu), and semiconductors (PbS, CdS). The very small loading of nanofillers in the polymer matrix can modify the whole material structure leading to great cost-effectiveness. Nano-filler materials, which have a larger specific surface area than that of micro-scale particles, offer excellent stress transfer between nanofillers and polymer matrix. The incorporation of CNTs in the polymer matrix presents large variability and affects overall material performances, including mechanical and functional properties. The electrical conductivity of CNT was approximately 10^3-10^7 S/m [115,116], however, a significant varying from 10^{-7}- 10^{-1} was shown with a different weight fraction of SWNTs and MWNTs in the polymer matrix [117-119]. The volumetric electrical conductivity of in-situ polymerization of MWNT/Poly(Methyl Methacrylate), PMMA, was increased up to 10 orders of magnitude from 10^{-4} to 10^{-3} S/cm providing dielectric PMMA into a semiconductor [120]. The addition of 1 vol% CNTs in composite increased thermal conductivity more than two times of conventional polymer and the 17 vol% CNT denser arrays improved the thermal conductivity by as much as a factor of 18 [121]. A very small percentage of CNTs do not only provide significant enhancement in functional properties but also essentially improve mechanical properties. The addition of 1 wt% SWNTs in EPON 862 polymer resulted in 26% and 16% increase in modulus and ultimate tensile strength (UTS), respectively [122]. The improvement of 36-42% in the elastic modulus and 25% in the ultimate tensile strength were observed in the modified CNT-Polystyrene composites because of CNTs bridging the crack faces generated under tensile strain [123]. An ultrasonic probe offered a better dispersion of 0.5 wt% MWNTs in bisphenol-A diglycidyl ether epoxy (DGEBA) resulting in a 16% improvement in the modulus [124]. The interlaminar fracture toughness can be improved by dispersing MWNTs onto woven CFRP prepreg composites [125]. On the other hand, an inadequate dispersion of CNTs in the matrix can reduce the UTS of epoxy due to ineffective stress transfer that results from unsatisfactory bonding between epoxy and CNTs [126-128].

MWNTs can be directly grown on the carbon fiber surface to form fuzzy fibers providing better interlaminar reinforcement by using CNTs to stitch the plies together [129-132]. These fuzzy fibers also have excellent interlaminar shear strength make it complicated for fiber to fracture from the polymer matrix. Thus, CNTs increase the number of fiber bridging between ply interfaces that could improve interlocking between fibers and matrix and also mitigates crack propagation. The improvement of 11%, 35%, and 16% in in-plane tensile strength, in-plane ductility, and out-of-plane stiffness were shown due to the directly grow CNTs over carbon fiber surfaces at low-temperature conditions [133]. Fracture toughness is an important property desirable for achieving stronger and durable composites for specific applications. The addition of CNTs, in general, has a significant effect on the toughness of epoxy. The mechanical properties and electrical conductivity showed relative improvements after surfactant treatment. An enhance of 60% in Mode I fracture energy was reported due to the addition of 0.25 wt% of surfactant treated MWNTs to EPON 828 epoxy [134]. The growing well-aligned CNT forest on micro-fiber fabric cloth demonstrated remarkable enhancements in both mechanical and multifunctional properties, including interlaminar fracture toughness, hardness, delamination resistance, thermoelastic behavior, and thermal and electrical conductivities [135].

The manufacturing of nanofiller polymer composites is a necessary step offering different composite structures, results in dissimilar nanocomposite material properties. There are numerous techniques introducing CNTs into structural advanced fiber composites, including mixing CNTs into the polymer, depositing CNTs on fibers by electrophoresis, or direct CNTs grown on fiber surfaces. Other factors, such as types of CNTs, composite fabrication process, and characterization methods, could also attribute to the large variation in properties. In the case of CNT formations, a number of walls, chirality, localized lattice defects, or disorder, the ratio of a mean free path (MFP) to characteristic length are the major parameter that can affect transport properties in CNT. The option of appropriate measurement methods, experimental set-up, and data reduction methods are all critical because of their small specimen size and associated physical problems. Thus, it is crucial to understand and identify the causes underlying a wide gap of reduction or large variation of structural and physical properties with various types of CNT, although the utilize CNTs in the macro-scale application is successfully achieved.

The CNT implementation technique in the composite can significantly influence its material property. Due to the percolation threshold theory, electron transport occurs between conductive particles in the thin insulating polymer layer. This percolation is stated once the concentration of incorporated conductive fillers to an insulated matrix polymer is just the right amount to generate a continuous conductive network throughout the structure. However, conductive clusters will dramatically increase in size by absorbing neighboring smaller clusters when the conductive filler concentration is higher than a critical value. These electron transports in the thin polymer layer can be modeled as electron hopping or tunneling. Electron hopping occurs across a potential barrier and is increasingly dependent on temperature. However, electron tunneling is allowed electron transfer only through a very thin polymer layer that commonly has a minimal potential barrier and is also independent of temperature. According to Fermi-Dirac distribution and localized carrier hopping and Coulomb gaps, this model is created to investigate the critical insulator to conductor transition. These theories are tailored to accommodate the large aspect ratio of CNTs and to observe transport behaviors; for example, the electrical conductivity shows an abrupt increase at a percolation threshold. According to percolation theory, the conductivity is given by

$$\sigma = \sigma_0 (f - f_c)^t \tag{4-1}$$

where σ_0 is the conductivity of the conducting phase, f is the volume fraction of the fillers; f_c is the critical volume fraction, known as the percolation threshold; the index t is the exponent, which is the rate of conductivity change. To obtain the conductive composite materials, the concentration of conducting fillers must be at or above the percolation threshold. Then, the conductivity is described in terms of fiber orientation, length, and other parameters related to their microstructure when the percolation threshold is not considered.

Thermal boundary resistance at CNT polymer boundaries, various component morphologies at low filler volume fraction dispersion, and nano-scale transport behavior need to be considered in an effective medium approach (EMA) model. The thermal boundary resistance is related to phonon frequency mode changes required during heat exchange at contact interfaces between CNTs and polymer or inter-particle CNTs. These are due to the weak mechanical and/or chemical adhesion, acoustic mismatch, and thermal expansion mismatch. The quantity and type of CNTs are defined by CNT alignment versus heat flux direction and boundary conditions. This thermal boundary resistance performs as the bottleneck for overall thermal conduction. The EMA model will show a linear increase in thermal conductivity with the increasing volume of randomly distributed of low volume fraction of CNTs once the contradiction of high electrical conductivity between CNTs and polymer is assumed. Numerous numerical models have been developed or both electrical and thermal transport, however, their validation has not been accomplished due to the lack of consistent experimental data. Thus, the input parameter has not been evaluated for its effect on electrical and thermal transport properties.

The incorporation of CNTs in polymer composite is difficult to control because of Van der Waals forces between CNTs burdening homogeneous dispersion so non-uniform CNTs polymer composite can occur as uncontrolled implementation methods. To acquire a successful design of CNT composites with effectively improved transport properties, well-characterized sets of specimens need to be properly prepared and designed in the manufacturing processes. The improvement of sample preparation by controlling CNT implementation can offer more accurate results of transport property. The accurate results of experimentally measured are crucial to the modified simulation of complex CNT morphology, which leads to a better understanding of transport behaviors and also to realize their limitations in CNT structures.

This chapter discusses nano-composites, composite fabrication, and characterization of nano-composites hybridized with FF and GNPs incorporation. The growth of CNTs and incorporation of GNPs on FF layer created nano-scale mechanical connections on the surface of carbon fiber. GNPs could create more electron and proton transfer pathways in fuzzy fiber increasing electrical and thermal conductivity throughout the composite. CNT was filamentary with approximately 20 nm in diameter and 4 µm in length. Carbon fiber was a continuous filament with around 7 µm diameter with 1 m long. In this study, the CNTs grown on the carbon fiber surface was simply denoted as fuzzy fiber (FF) layer. The development of CNT quality is required by varying parameters (precursors, catalysts, processing time) while maintaining their controlled morphology through good characterization. The primary advantages of FF are mechanical and functional properties improvement. Due to the CNTs grown on the fiber surface, these CNTs interact with one another in both intra- and inter-plies that act as mechanical bridge forming conductive pathways in the insulating polymer matrix throughout the composite. A well CNT dispersion within the matrix can be obtained because CNTs remain attached to the fibers as grown. Thus, this method introduces a choice to overcome many issues of a traditional direct mixing CNTs method that causes agglomeration, defect, damage, and composite property degradation even with low volume fractions. Thus, the direct growth of CNTs on the carbon fiber wafer is one of the promising approaches to acquire well dispersion, high density, and good incorporation between CNTs and adjacent laminate even at a high volume fraction of nano-fillers. An additional GNPs conductive filler was then dispersed on the fuzzy fiber surface to form synergistic physical interactions between two different low-dimensional carbon-based nanostructures. Then, the fabrication methods of CFRP and FFRP composites with and without GNPs and composite characterization are discussed in detail.

4.1 Preparation modified polymer composite on fuzzy fiber surface

High purity industrial grade JCPG-99-2-6 GNPs with a diameter of approximately 6×6 μm and 99.7% purity was purchased from Nanjing Yokook Nano Technology, China. GNPs were supplied in few-layer stacks with thicknesses of less than 3 nm from the optimization of the Hummers method. Many preparation techniques have been studied to disperse graphene into epoxy resins [136]. GNPs are one of the novel fillers that can disperse in many different types of the polymer matrix. GNPs could effectively be distributed using the melt blending method in the high-temperature process, but an ineffective GNPs/epoxy can be observed due to the increase of polymer viscosity and bulking or shortening during the process [137]. The direct mixing of GNPs in the viscous epoxy resin is not an appropriate technique due to a high surface-to-volume ratio, results in non-uniform dispersion of the nanofillers in higher loading. To improve the dispersion quality and high chemical bonding of the immiscible phase between GNPs and epoxy resin, the solution mixing technique is recommended to reduce the chance of graphene sheets restacking in the dry state with strong hydrogen bonding. GNPs have a great level of dispersion in organics and polar solvents such as water, acetone, and IPA that acts as a spacer keeping GNPs separation and sonicates in the ultrasonic bath until a homogeneous dispersion is achieved [137].

Figure 4-1. Modified epoxy GNPs infiltration.

GNPs were initially dispersed in isopropyl alcohol (IPA) at the rate of 1 mg/ml for an hour of sonication to obtain a dark brown-colored solution without any visible precipitation remainder. Ultrasonication was used to distribute fillers into the solvent by agitating it and breaking the agglomeration of GNPs particles. The optimal ultrasonication time is one of the major parameters for acquiring a homogeneous suspension. The precipitation of fillers diminished significantly due to the increased ultrasonication time. To prepare modified GNPs/epoxy polymer, the desired weight fraction of GNPs to be added to the epoxy resin using magnetic stirring was calculated based on the pre-determined target. The epoxy mixture was then stirred at 90 °C for several hours under moderate speed to evaporate the solvents, followed by placing it in an oven overnight as shown in Figure 4-1. The decrease of viscosity by elevated temperature in the epoxy could increase the quality of the fillers-matrix suspension. After the solvent was completely removed, the modified GNPs/epoxy resin was allowed to cool down to room temperature. Then, an amine-based curing agent was added to the GNPs/epoxy, followed by degasses bubbles. The polymer solutions were then coated on the fuzzy fiber surface.

4.2 Manufacturing carbon fiber hybrid epoxy resin nanocomposites

Composites were fabricated using 2 different methods; namely VARTM and hand lay-up with autoclave post-cured technique. Nanocomposites were primarily comprised of 4 materials, which were FF layer, conventional carbon fiber, polymer, and GNPs. Two parts of the polymer matrix used to prepare the samples, which were epoxy resin and curing agent hardener. Epoxy resin and amine-based curing agent hardener polymer matrix were supported by high-performance ML-812A-LV and ML-812B-LV from Wells Advanced Materials Co., Ltd., Shanghai, China. This epoxy resin contains more than 50%, 10-30%, and 5-20% of Bisphenol A epoxy resin, Bisphenol F epoxy resin, and aliphatic glycidyl ether epoxy resin, respectively. The density of this epoxy is 1.1-1.2 g/cm^3 at 25 °C as provided by the vendor, which was used in this experiment. This high-performance epoxy resin, which was designed for the vacuum infusion process, provided strong adhesion, low viscosity, high toughness, superior mechanical and physical properties, and also chemical and heat resistance. An aluminum mold was used to fabricate hybrid CFPR composites with 100 x 150 mm in dimensions. Reference specimens were fabricated using 8 or 16 layers of carbon fiber. On the other hand, another batch of highly conductive composite specimens was fabricated using 8 or 16 plies of carbon fiber together with fuzzy fiber with and without GNPs on the outermost ply modification. The viscosity of epoxy resin was high at room temperature and reduced with the increase of temperature. However, the further increase in temperature could also increase viscosity due to the initiation of gel formation and subsequent curing process. In the case of matrix preparation, both epoxy and hardener were separately degassed using a vacuum oven for 15 minutes to remove air bubbles. The amine-based curing agent hardener was added to the formulation using an epoxy: hardener ratio of 2.5:1, mixed by a mechanical stirrer. This polymer matrix can be cured at room and post-cure at a higher temperature to expand more application scope.

4.2.1 Vacuum-assisted resin transfer molding (VARTM)

CFRP composites were fabricated using the VARTM method. The VARTM has attracted great attention because it can manufacture high-quality composites with cost-effectiveness. According to the VARTM process, a peel ply was laid in the first layer to facilitate the easier removal of the samples from the aluminum mold. Each ply of dry woven carbon fiber was placed on top of each other until 8 or 16 fiber stacks were acquired, followed by another peel ply on top of carbon fiber. Only the outermost ply was replaced by 1-2 fuzzy fiber layers with and without GNPs. Spiral resin infusion was placed at the entry for leading resin flow in both longitudinal and lateral directions and exit for release excessive epoxy. Then, a vacuum bag was covered and tightly sealed to the aluminum mold, connected with the resin inlet tube and resin outlet tube. Air was then evacuated by a vacuum pump that connected with the resin outlet tube. The panel of carbon fiber samples was cured at room temperature for more than 24 hours, followed by post-cured in the oven at 150 °C for 4 hours to reduce the excessive epoxy resin and voids. Then, fully impregnated hybrid nano-reinforced carbon/epoxy composites can be acquired. The finished composites were cut into the desired size. The thickness of 8 and 16 plies was approximately 2 and 3.52 mm, respectively. Conventional CFRP composites were served as a reference specimen. The mechanical properties and functional conductivities of fuzzy fiber composites with and without GNPs were demonstrated and compared with reference panels to evaluate the effect of fuzzy fiber with and without GNPs nanopolymer in Chapter 5.

4.2.2 Hand lay-up technique

A Hand lay-up method with autoclave curing is an alternative method with a more promising approach to achieve a better quality of composites. Conventional CFRP and fuzzy fiber together with different loading of GNPs polymer composites were fabricated using wet lay-up technique as illustrated in Figure 4-2. Epoxy was first poured onto carbon fiber cloths between the plastic film and cut carbon fiber into the desired size. Carbon fiber cloth was then added on top of each other. Sixteen laminates of resin-impregnated carbon fibers were fabricated with only the outermost ply modification by fuzzy fiber (with and without GNPs loading). A release film, an aluminum caul plate, thermal sensors, and numerous layers of the bleeder, and a vacuum bag were placed on top of carbon fiber, respectively to apply uniform pressure and to absorb excessive epoxy. The laminates were cured in the autoclave at 50 °C for 4 hours, followed by post-cured at 150 °C for 3 hours at 0.3 MPa cured pressure to reduce air bubbles resulting in a better quality of laminates. The cured laminates were cut into desired individual specimens. The thickness of composites was approximately 3.52 mm, which was thinner than the fabricated composites from the VARTM method. Autoclave curing could improve the quality of composites by minimizing voids and epoxy-rich area.

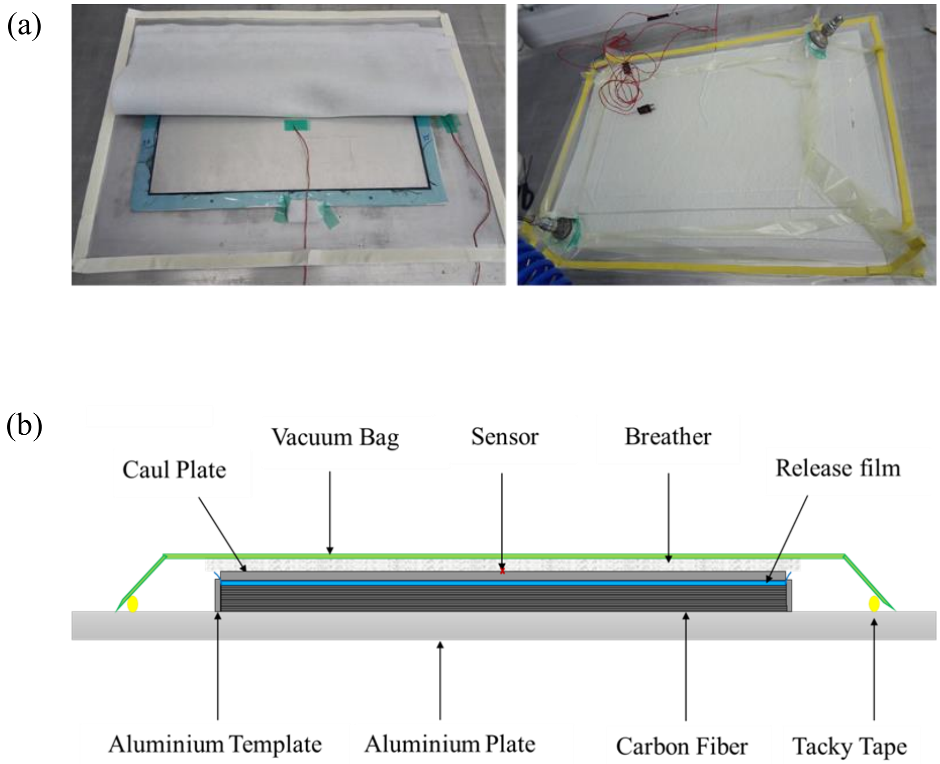

Figure 4-2. Composite fabrication by hand lay-up of the (a) top view and (b) side view.

4.3 Characterization of composites

The optical photos and cross-section images of composites can be observed with a digital camera and optical microscopy, respectively as shown in Figure 4-3**.** The conventional and fuzzy fiber composites, which were fabricated by hand lay-up with autoclave technique, are presented in. The CFRP composite served as the baseline panel to compare with CFRP with a carbon-based layer. The classification of composite specimens can be observed in Table 4-1.

Table 4-1. Classification of samples.

Type of specimen	No. of total carbon fiber	No. of CNT growth on carbon fiber surface	Content of GNP fillers (wt%)
CF8	8	0	-
FF8	8	1	-
2FF8	8	2	-
CF	16	0	-
FF	16	1	-
0.05G/FF	16	1	0.05
0.1G/FF	16	1	0.1
0.2G/FF	16	1	0.2

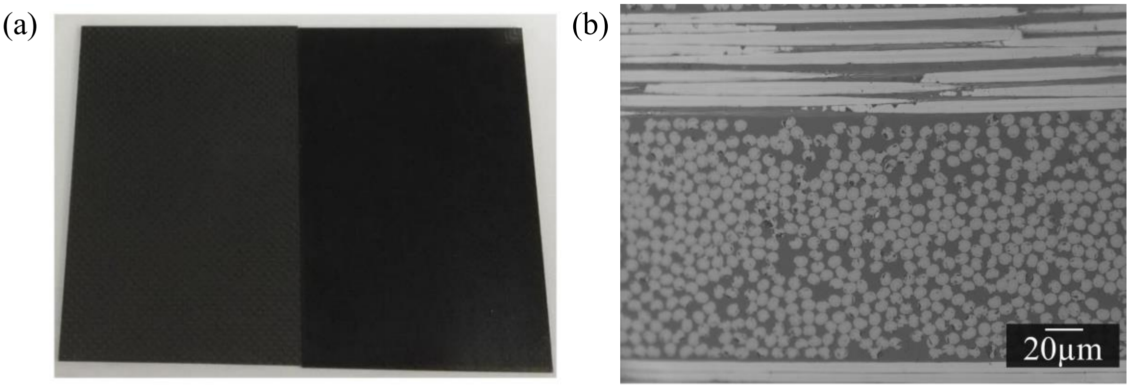

Figure 4-3. Composite photos of (a) optical image of CFRP (grey) and fuzzy fiber (black) laminate and (b) cross-section of CFRP composite.

The carbon fiber volume fraction demonstrated via TGA can be calculated to be approximately 58-60 vol%. TGA was carried out on the epoxy, CFRP composites, and fuzzy fiber composites to determine the volume fraction of fiber and matrix in the composites under nitrogen flow (20 ml/min) that can be observed in Figure 4-4. The TGA data of epoxy matrix samples showed a significant drop in mass around 300 °C to confirm thermal decomposition and by 600 °C less than 1.5 % of mass remained. The decomposition reaction of epoxy was ended around 500 °C according to the flat curve of derivative weight (DTG) presented in Figure 4-4(a). Then, the remaining mass was attributed to fiber reinforcement mass as shown in Figure 4-4(b). The fiber volume fraction (V_f) can be expressed as follows:

$$V_f = \frac{\left(\frac{W_f}{\rho_f}\right)}{\left(\frac{W_f}{\rho_f}\right)+\left(\frac{1-W_f}{\rho_m}\right)} \tag{4-2}$$

where W_f is the fiber weight fraction, ρ_f and ρ_m is the density of fiber and resin matrix (g/cm^3), respectively.

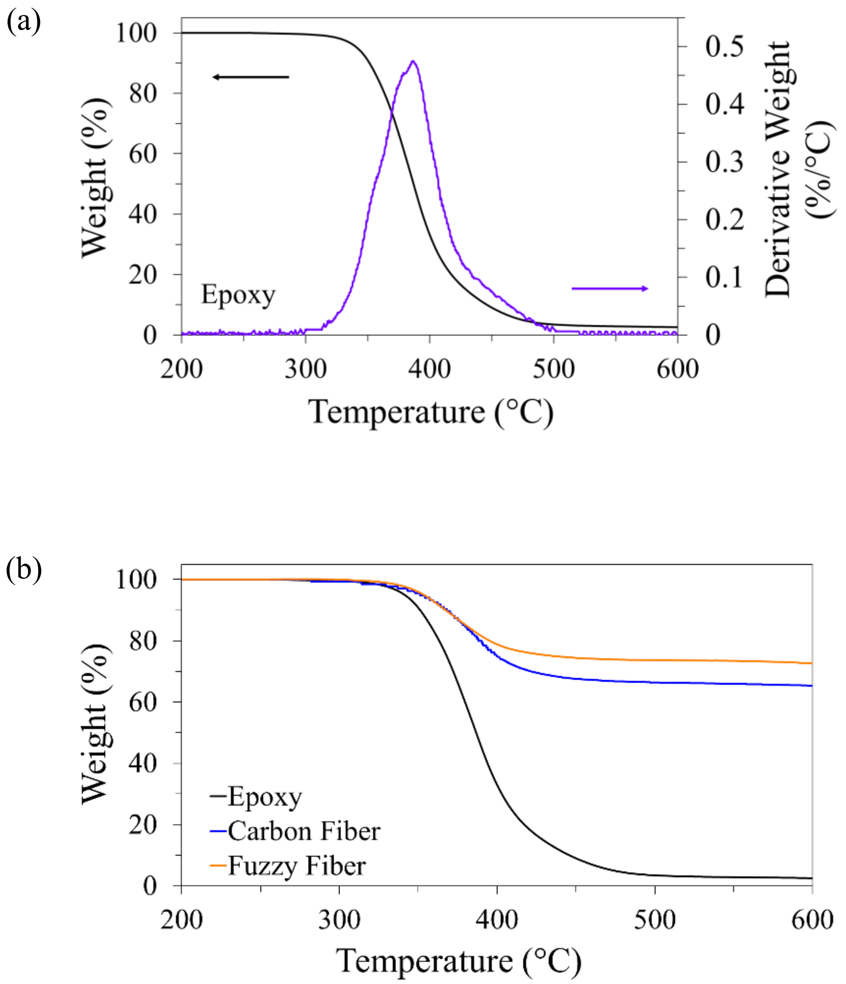

Figure 4-4. TGA data of (a) epoxy matrix and (b) composites under nitrogen condition.

4.4 Summary

Nanopolymer was prepared by incorporating GNPs into epoxy. Composites were then fabricated using 2 different methods, which are called VARTM and hand lay-up method. The traditional wet lay-up together with autoclave curing could reduce voids and excessive resin improving the quality of laminates. Highly conductive composites were modified only at the outermost surface of conventional composites using fuzzy fiber with and without GNPs. The volume fraction of fiber was calculated based on TGA results. The mechanical and functional properties of laminates will then be presented in Chapter 5.

CHAPTER 5

CHARACTERIZATION OF NANOCOMPOSITES

There were various tests applied in this experimental section. The experimental section can be used to characterize these hybrid polymer composite materials. Each experiment contained at least five similar specimens to average the results in order to acquire accurate results. Three different mechanical experiments were tested to inspect flexural, interlaminar shear strength, and toughness properties. Then, the morphological properties of the fracture surfaces from impact test specimens were carried out on FE-SEM. The functional properties were also performed to inspect and to compare the electrical and thermal conductivities in each batch of materials.

In this study, the objective is to overcome the lack of functional property issues in composite materials so the samples were fabricated by attaching a carbon-based LSP layer on the uppermost ply of CFRP composites. The suitable parameters of growing CNTs on carbon fiber and appropriate percentage of GNPs in composites were investigated on their structural, functional, and morphological properties. The FF composites with and without GNPs were demonstrated to ensure that the LSP layer provided an adequate capability to protect the underlying composite minimize the cost of maintenance. Due to the lightning-induced damages, the enhancement of structural and functional properties are required in the outer aircraft's skin. All of these testings were a primary experimental section to investigate the material behavior and performance for comparing its mechanical properties such as strength between four types of characteristics. The results of the experimental test conducted in the material testing laboratory at The Hong Kong Polytechnic University have also been discussed in this section. There were eight different series of composites as shown in Table 4-1. The experimental tests, including the mechanical test (three-point bending, short-beam shear test, and Izod impact test) and the electrical and thermal conductivity test were conducted on each type of specimen.

5.1 Materials and methodology

5.1.1 Three-point bending test

The flexural properties of nanocomposites were demonstrated according to ASTM D7264/D7264M-15 [138] using an Instron 5982 mechanical testing system with a 100 kN load cell. The setup of the three-point bending test can be observed in Figure 5-1. The rectangular specimen was loaded in a three-point bending mode. The width and thickness of the specimen were measured at least three different locations on the specimen using a digital Vernier Caliper for analysis. The specimens were resting on two supports and a loading nose was loaded with a downward force at the middle of the span. The span-to-depth ratio was set at 32:1 and the test was conducted at a constant cross-head speed of 2 mm/min. At least five specimens were tested in each testing series (each type of condition). Specimens presented an initial fracture followed by several secondary failures causing less load-carrying capacity.

The flexural strength (σ_f) and modulus (E_B) can be calculated as follow

$$\sigma_f = \frac{3PL}{2bh^2} \tag{5-1}$$

$$E_B = \frac{L^3 m}{4bh^3} \tag{5-2}$$

where *P* is the maximum load (N), *L* is supported span length (mm), *b* is specimen width (mm), *h* is specimen thickness (mm), m is the slope of the tangent gradient of the initial straight line of the load-deflection curve.

Figure 5-1. Three-point bending test of an Instron 5982 testing machine.

5.1.2 Short beam shear test

A three-point short beam shear test was conducted to determine interlaminar shear strength (ILSS) according to the ASTM D2344 [139]. At least five replicate rectangular bars with dimensions of 24 mm x 8 mm (length x width) were prepared and loaded in a three-point bending mode. The recommended geometry of specimens can be calculated from the Equation below.

$$\text{Specimen length} = \text{thickness} \times 6$$

$$\text{Specimen width} = \text{thickness} \times 2 \tag{5-3}$$

The width and thickness of the specimen were measured at least three different locations on the specimen using a digital Vernier Caliper for analysis. The specimens were placed on two supports and a loading nose was loaded with a downward force at the middle of the span. The support span-to-depth ratio and testing speed were set at 4:1 and 1 mm/min, respectively. At least five specimens were evaluated for each type of composite. Specimens presented an initial fracture followed by several secondary failures causing less load-carrying capacity. The typical failure modes can be observed in Figure 5-2. This data can be used for research and development purposes concerned with interply strength, or prove useful in comparing composite materials. Figure 5-3 illustrates the setup of conduct short-beam shear tests.

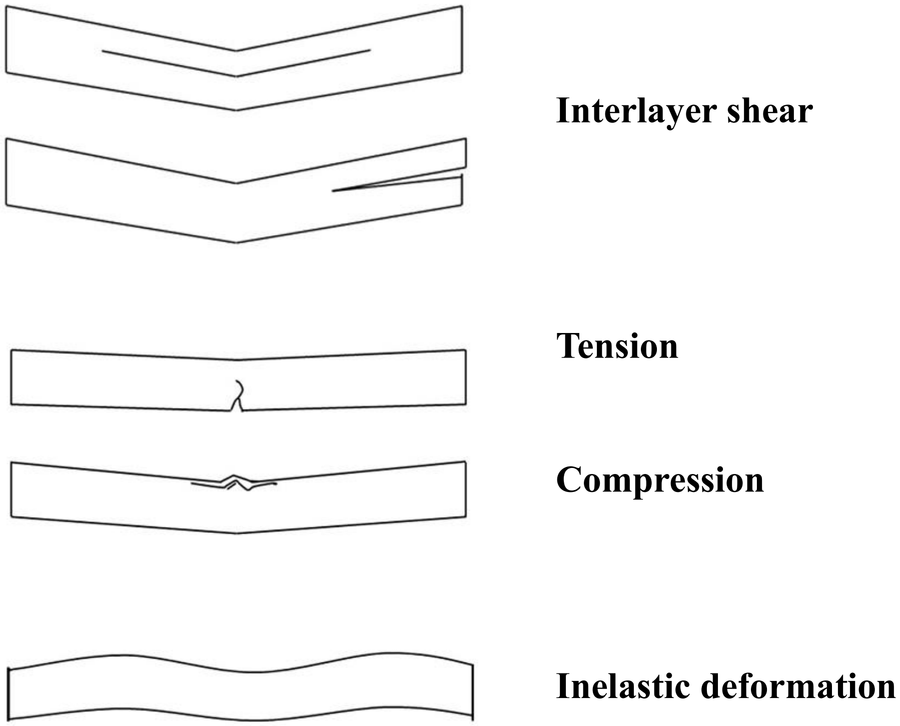

Figure 5-2. Failure modes in the short beam shear test.

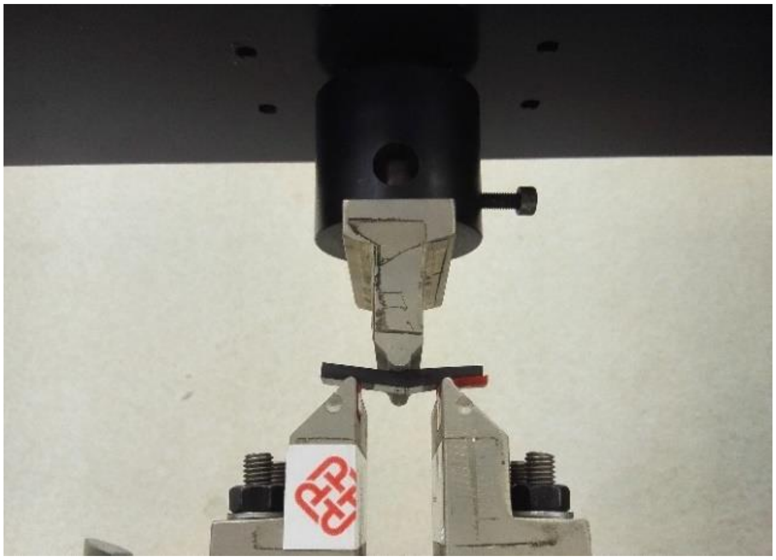

Figure 5-3. Schematic set-up of the short beam shear test.

The short-beam strength (F^{sbs}) and modulus (E_B) were calculated by Equation 5-4 and Equation 5-5.

$$F^{sbs} = 0.75 \text{ x } \frac{P_m}{b \, x \, h} \tag{5-4}$$

$$E_B = \frac{L^3 m}{4bh^3} \tag{5-5}$$

where F^{sbs} is short-beam strength (MPa), P_m is the maximum load (N), b is specimen width (mm), h is specimen thickness (mm).

5.1.3 Izod impact test

An Izod impact test was carried out to investigate the impact energy of V-notched composite specimens. A low energy testing with a pendulum hammer was applied to composites as stated in ASTM D256 [140]. The dimension of the specimen and the impact test set-up can be observed in Figure 5-4 and Figure 5-5.

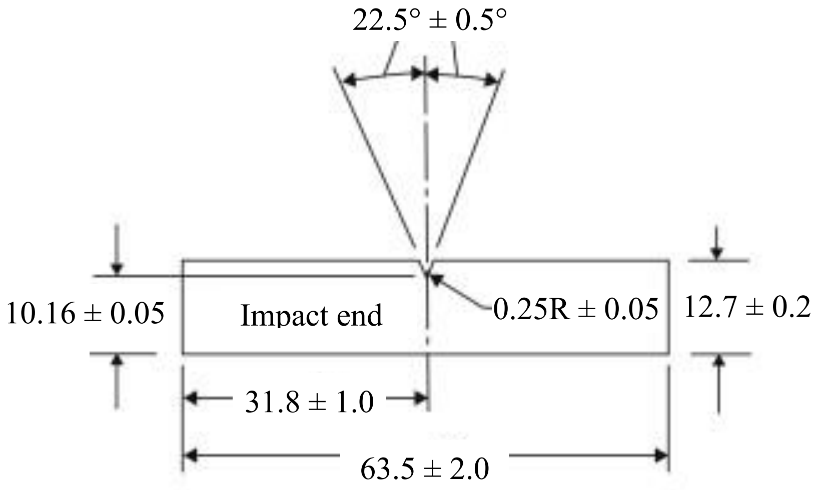

Figure 5-4. V-notched Izod type composite specimen (All dimensions shown in millimeters).

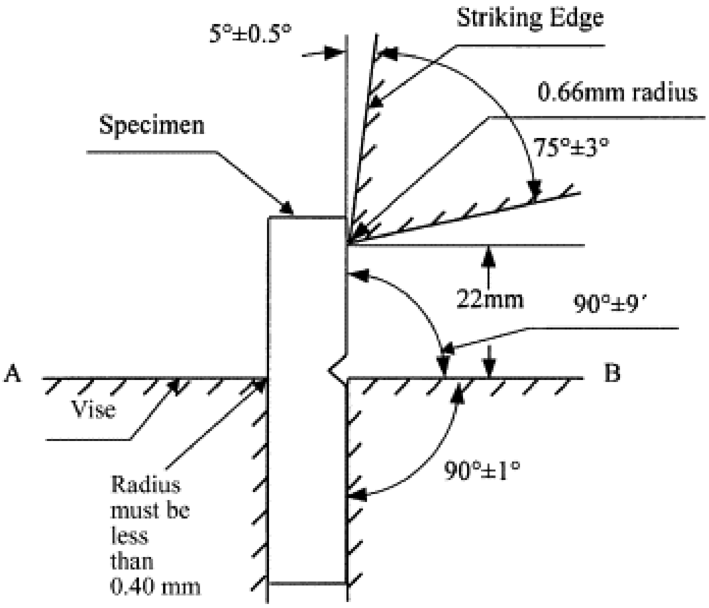

Figure 5-5. The apparatus set-up of Izod test [141].

There are four different categories of failure modes as mentioned below.

Complete break (CB) – A break where the specimen separates into two or more pieces.

Hinge break (HB) – An incomplete break, one part of the sample cannot support itself above the horizontal when the other part is vertically held (less than 90° included angle).

Partial break (PB) – An incomplete break that does not meet the definition for a hinge break but has fractured at least 90% of the distance between the vertex of the notch and the opposite side.

Non-break (NB) – An incomplete break where the fracture extends less than 90% of the distance between the vertex of the notch and the opposite side.

At least five replicate rectangular bar specimens were prepared and were vertically located in the machine holder. The average value of impact energy from the V-notched Izod impact test was acquired from each set of material conditions. The impact area was calculated from a specimen using Equation 5-6.

$$A_0 = b.(h - t) \tag{5-6}$$

The strength had required the energy to produce fracture for breaking the specimens, can be calculated by impact energy divided by impact area,

$$a_k = \frac{W}{A_0} \tag{5-7}$$

where A_0 is the impact area (mm^2), a_k is the impact strength (J/mm^2), W is the impact energy (J), b is the specimen width (mm), h is the specimen thickness (mm), t is the specimen notch depth (mm).

5.1.4 Electrical properties

Electrical conductivity is the flow of an electric current (a flow of electrons) on the surface of composite structures. There are two types of measurement, which are two-point and four-point probe conductivity measurements. Current injects through the outer probes and induces voltage at 2 different points in the inner voltage probes eliminating the contact resistance in the four-probe method. A four-point probe technique yields more error than the contact resistance of the probe minimizing inaccuracies from this contact resistance. In the case of a two-point probe measurement, one probe is used for current injection and another probe for voltage measurements, which are included contact resistance showing less accuracy.

In this work, the samples were analyzed by the two-probe resistivity method for determining in-plane and out-of-plane electrical conductivities along with the different directions of composites with and without LSP systems. Specimens were performed using Micromanipulator Probe station 450PM-B with Keithley 4200-SCS Semiconductor Parameter Analyzer. The geometry of rectangular specimens was designed based on ASTM standard D257 for baseline laminates and based on ASTM D4496 for fuzzy fiber composites. The electrical conductivity measurement set-up was depicted in Figure 5-6.

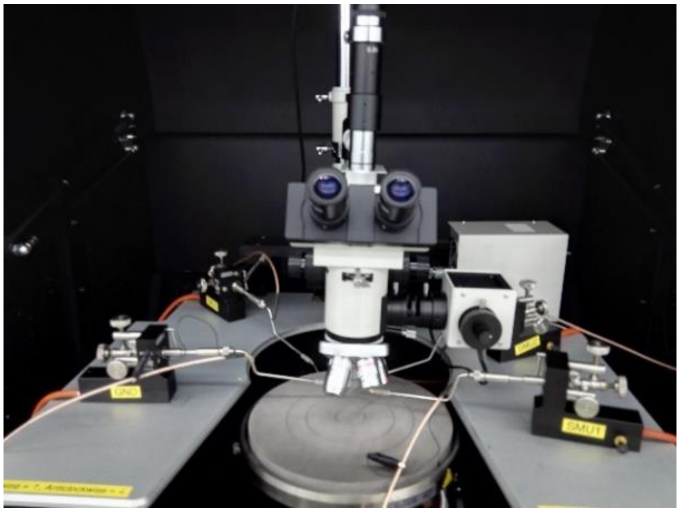

Figure 5-6. The specimen set up of electrical conductivity test.

The electrical conductivities were measured in the direction along with carbon fiber, surface, and through-thickness direction. Sample dimensions were controlled on the order of millimeters with less than 2% dimensional variation. All samples were painted with conductive paint (silver paster) acting as electrodes, which offer better current distribution across the samples. These two electrodes were parallelly deposited onto the relevant composite areas as shown in Figure 5-7. However, electrodes were manually coated showing a high chance of inconsistent electrodes. Electrodes were then carefully prepared to ensure smooth and good surfaces. Specimens were also conditioned in an environment of 9-15% humidity at 25 ℃ for 48 hours as mentioned in ASTM D4496. The resistance was measured when DC current was applied between two electrodes. A minimum of three replicate specimens was performed in each different loading series. The average electrical conductivity of in-plane and out-of-plane directions were acquired from each set of material conditions.

The electrical resistivity (ρ) is defined as

$$\rho = R\frac{A}{l} \tag{5-8}$$

The above equation can be transposed to get Pouillet's law.

$$R = \rho\frac{l}{A} \tag{5-9}$$

The given material resistance will be affected by the geometry of composites. According to the above equation, the electrical conductivity (σ) is defined as follow:

$$\sigma = \frac{1}{\rho} \tag{5-10}$$

where σ is the electrical conductivity (S/cm), ρ is the electrical resistivity (Ω.cm), R is the electrical resistance of a uniform specimen of the material (Ω), l is the length of the piece of material or between the electrode (cm), A is the cross-sectional area of material or electrode (cm^2)

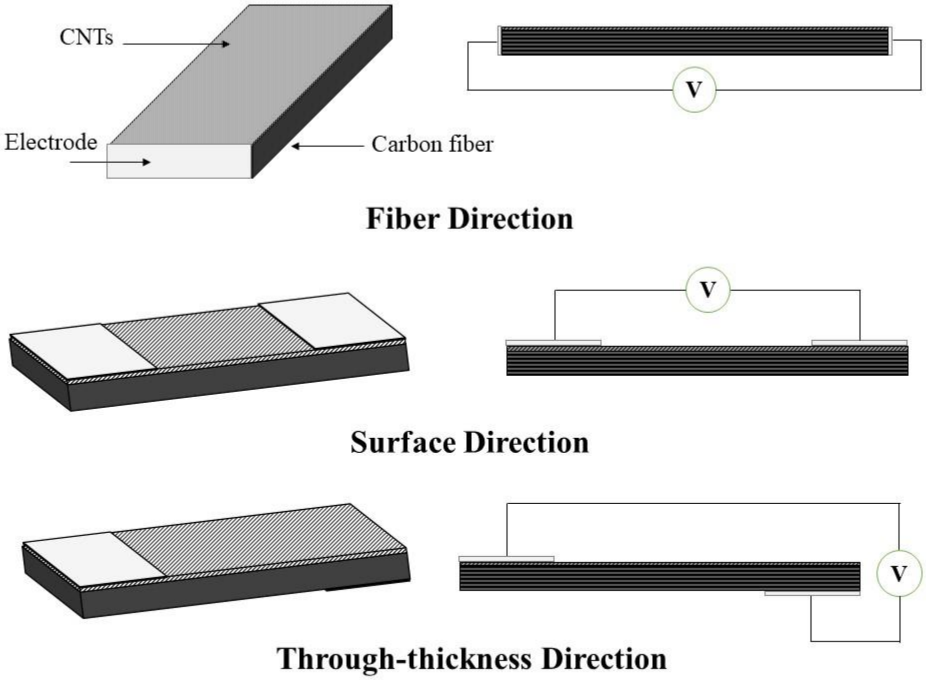

Figure 5-7. Diagram of electrical conductivity measurements.

5.1.5 Thermal properties

Thermal conductivity refers to the intrinsic ability to conduct or to transfer heat in the material. Samples were carried out according to ASTM E1461 [142] using Anter Flashline^{TM} 2000 laser flash method. This system can automatically determine thermal conductivity based on heat capacity and thermal diffusivity measurement. SP-1 Vespel (1.4 g/cm^3 density, 0.35 W/mK) material was chosen as the reference because its thermal conductivity is in the same range expected for these laminated composites. The reference sample was tested to evaluate the measurement environment, such as heat losses in the set-up. The disc-shaped specimens of 12.7 mm in diameter were prepared and measured their density. The thickness of the specimen was measured at least three different locations on the specimen using a digital Vernier Caliper for analysis. Samples were spray-coated with graphite to enhance emissivity. The prepared composites and reference material were then placed into the machine. The samples were heated with a laser pulse on the top surface and temperature profiles were recorded on the backside with an IR detector. The measurement was repeated three times on each batch.

5.2 Results and discussion

5.2.1 Flexural properties

The flexural strength of carbon fiber and fuzzy fiber composites as a function of GNP loading is shown in Figure 5-8. In the case of the VARTM method (red graph), the flexural strength of fuzzy fiber composites was moderately lower than that of conventional CFRP composites by 9%. The strength in 0.05wt%, 0.1wt%, and 0.2wt% GNPs on fuzzy fiber composites presented approximately 6%, 5%, and 9% improvement compared with CFRP composites, respectively. On the other hand, the insignificant improvement of flexural strength showed in fuzzy fiber composites that were fabricated by wet lay-up with autoclave curing process (black graph). The incorporation of 0.05 wt% and 0.2 wt% GNPs on fuzzy fiber composites increased the flexural strength by approximately 13% and 15% compared with CFRP composites, respectively. The maximum strength in 0.1 wt% GNPs on fuzzy fiber demonstrated a 20% enhancement compared with conventional composites. The modification of the uppermost ply composites using fuzzy fiber resulted in a slight improvement in the flexural strength compared to reference composites due to the better interlocking between CNTs and adjacent carbon fiber. Other researchers have reported the improvement of mechanical properties with the integration of GNPs in composite materials [25,75]. The small integration of GNPs on fuzzy fiber composites using the wet lay-up method with autoclave curing increased the flexural strength of the CFRP composites.

The flexural modulus also increased with the presence of GNPs due to the reinforcing-ability and rigidity of graphene nano-fillers, as illustrated in Figure 5-9. This modulus was calculated in the elastic linear region before respective failure modes came into account. The flexural modulus of fuzzy fiber by the VARTM method showed an unchanged trend as presented in Figure 5-9 (red graph). The modulus of the composites dramatically inclined up to the peak of 48 GPa demonstrating 12% improvement with the incorporation of 0.05 wt% GNPs into fuzzy fiber composites and then degraded in the composites with a higher GNP content loading. In the case of a hand lay-up process with autoclave curing (black graph), the maximum modulus was achieved with the incorporation of 0.05wt% GNPs into fuzzy fiber composites, which was a 32% increment compared with conventional composites. These nanofillers were integrated into the epoxy resin composite matrix structure through chemical bonding formation. They had further replenished porosity in the matrix, so it had a capacity to restrict the movement of the epoxy molecular chain. The improvement of the composite materials' modulus and strength could be attributable to efficient stress transfer across the matrix and filler interfaces that lead to higher flexural stress and stiffness of the matrix system.

The increase of flexural properties could also be attributable to mechanical interlocking, which is the mechanical locking at the interface between fiber and the epoxy resin polymer layer. This relates to the surface roughness of epoxy resin improving the interfacial adhesion bonding between fuzzy fiber and epoxy matrix by the reinforcement of GNPs [143]. The size of fillers has also facilitated the processing of fabricated composite samples because the small size of fillers could be easier to disperse into the epoxy matrix, resulted in reducing the possibility of agglomeration. Homogenous matrix composites with uniform GNPs distribution could increase the surface availability of fillers and improve the potential of interfacial interaction via covalent bonding, which also enhances the effect of filler loading transfer between fillers and matrix [144]. However, the flexural modulus of fuzzy fiber composites shows a slight decline when the GNP loading exceeds 0.05 wt.%. The integration of GNPs may decrease the flexural modulus due to large Van der Waals forces and strong $\pi - \pi$ interaction that might cause a multi-layer stack to form an agglomeration of GNPs in the epoxy resin matrix. The degeneration of flexural modulus could attribute to the mechanical interlocking and the absorption occur between matrix and filler. This indicates an uneven distribution of fillers that results in weaker interfacial interaction because the agglomeration of fillers can act as stress concentration points that lead to accumulation stress on the neighboring particle location forming cracks or other damages. The advancing and propagation of crack will eventually lead to brittle failure. Therefore, the non-uniform dispersion of GNPs possibly causes microstructural defects and adverse effects in the whole composite material.

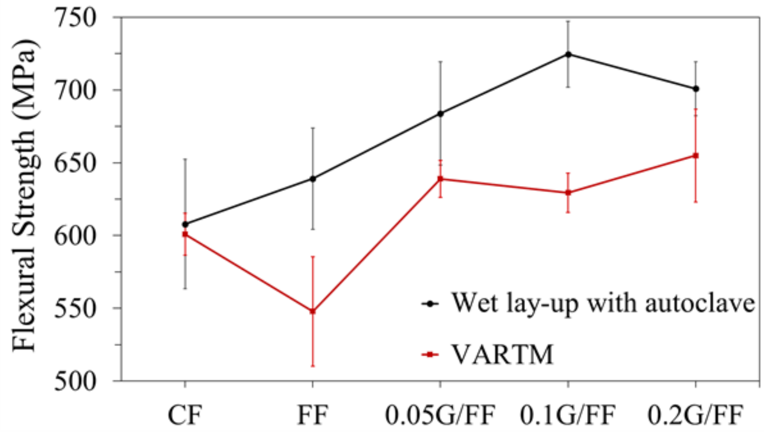

Figure 5-8. Flexural strength results of CFRP and fuzzy fiber composites with and without GNPs.

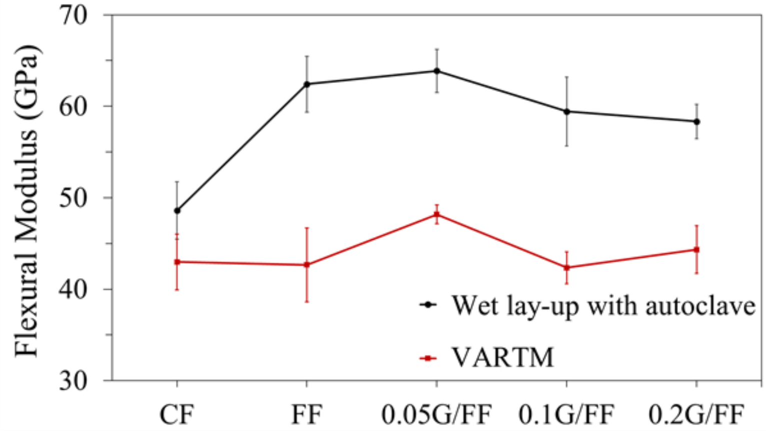

Figure 5-9. Flexural modulus results of CFRP and fuzzy fiber composites with and without GNPs.

5.2.2 Interlaminar shear strength (ILSS)

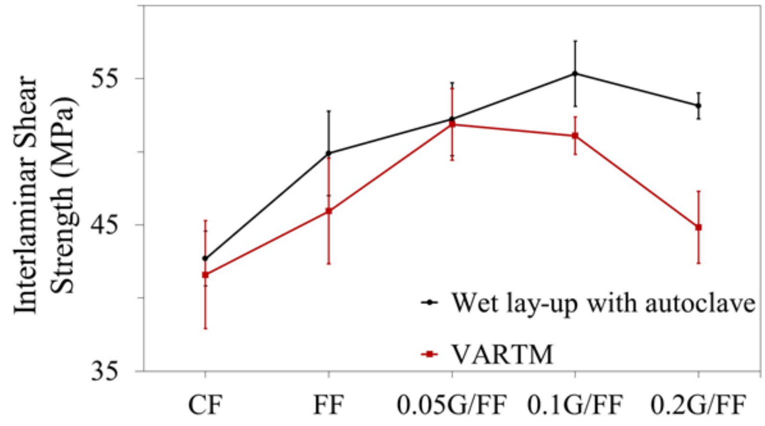

Figure 5-10. Interlaminar shear strength (ILSS) results of CFRP and fuzzy fiber composites with and without GNPs.

The ILSS results of carbon fiber and fuzzy fiber composites as a function of different GNP weight percentage content with both wet lay-up and VARTM method are shown in Figure 5-10. The ILSS results of the reference CFRP composites were 41.6 MPa and 42.7 MPa in the VARTM method and hand lay-up process with autoclave curing, respectively. Fuzzy fiber composites improved ILSS by 10% in the VARTM method and 17% in the hand lay-up process with autoclave curing, which can be attributed to the increment of the contact area between the carbon fiber and the matrix because of the CNTs grown on the carbon fiber fabric. The incorporation of GNPs in fuzzy fiber composites was further improved in ILSS because the GNPs stiffened the matrix and created mechanical interlocking between CNTs grown on the carbon fiber fabric. This can be attributed to the better stress transfer between filler and matrix. In the case of VARTM, the ILSS of the composites increased up to a peak of 51.9 MPa with the integration of 0.05% GNPs coated on fuzzy fiber. On the other hand, the maximum ILSS of 55.3 MPa was revealed with the incorporation of 0.1% GNPs coated on fuzzy fiber composites using wet lay-up with autoclave process and then degraded in the composites with a further percentage of GNP content. The decrease in ILSS with higher percentages of GNP loading may be attributable to the agglomeration caused by the non-sufficient distribution of nanofiller hybrids in the nanocomposites. This could have increased the interface stress concentration, which in turn would have resulted in deficient stress transfer between fillers and matrix. Furthermore, it could also be attributed to the increase in the viscosity of the epoxy. Due to the increase in viscosity, it may be difficult for the GNP/epoxy mixture to flow into the void spaces in the CNT-grown carbon fiber, thereby hindering the integration of fuzzy fiber with the hybrid epoxy matrix. The overall ILSS results of composites with and without LSP system using the VARTM method were lower than compare with those of composites fabricating by wet lay-up with curing.

5.2.3 Impact energy

One of the significant engineering challenges in material design is the conflict between strength and toughness due to their mutually exclusive properties. Izod impact toughness results of reference composites demonstrated approximately 35 kJ/m^2 in both VARTM and hand lay-up with autoclave process, as indicated in Figure 5-11. The toughness results of composites declined with the modification of fuzzy fiber with and without GNPs integration that was fabricated using the VARTM process. However, the small integration of 0.05 wt% GNPs on fuzzy fiber composites presented an 18.5% increment in the toughness compared with fuzzy fiber composites but was still lower than that of based composites by 6%. On the other hand, the Izod impact tests of GNPs-coated on fuzzy fiber composites yielded an impact toughness of 44.2 kJ/m^2, which was a 25% increment compared with conventional composites that were fabricated by wet lay-up with autoclave curing process (black graph). The synergistic effect of CNTs and GNPs on carbon fibers can restrict the fracture path, extend the crack propagation route, and hence result in a durable larger deformation effectively increasing the impact toughness. The enhancement of impact toughness can be attributed to the homogeneous dispersibility of GNPs filler at 0.1 wt.%, whereas the toughness of fuzzy fiber composites displays a slight reduction when the GNP loading exceeds 0.1 wt.%. The reduction in the toughness of fuzzy fiber composites by the integration of GNP loading is probably due to the composite fabrication process as shown in the integration of 0.05wt.% GNPs. The agglomeration of fillers can also minimize the impact of toughness because the increase in GNP loading can induce agglomeration in epoxy. These agglomerated fillers turn into defects, creating stress concentration, and consequently diminishing the fraction toughness. Interestingly, an adverse effect of impact toughness was shown in the fuzzy fiber composites integrated with and without GNPs using the VARTM fabrication process. However, the impact toughness in fuzzy fiber composites integrated with GNPs using wet lay-up with autoclave curing did not show an adverse effect of an increase in strength and stiffness. A noticeable variation in mechanical properties can be influenced by the composite fabrication method. It is believed that the hand lay-up with the autoclave process can improve the quality of composites and mechanical properties.

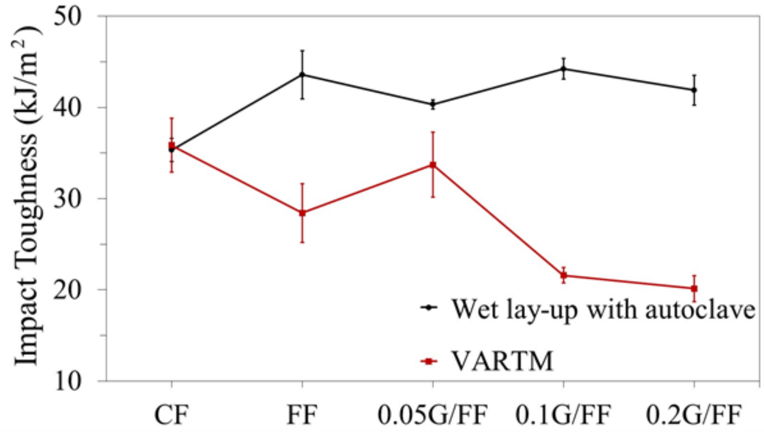

Figure 5-11. Impact toughness results of CFRP and fuzzy fiber composites with and without GNPs.

To gain more insights, the fracture surfaces of the impact test specimens using hand lay-up with autoclave curing process were investigated using SEM, as shown in Figure 5-12. Failure in conventional composites was dominated by splitting and smooth surface of fiber/matrix debonding, demonstrating low impact fracture toughness due to the weakness of interfacial bonding between carbon fiber and epoxy matrix. These findings can be observed in Figure 5-12(a). The simultaneous breaking of fibers, matrix cracking, and debonding of the fiber-matrix can be observed in fuzzy fiber composites (with and without GNP filler) in Figures. 5-12(b) and 5-12(c). Due to the growth of CNTs on the carbon fiber surface together with GNP incorporation, the fractional forces were increased and higher energy could thus be absorbed in the failure process. The small integration of filler content can increase ductility in the matrix as shown in the smaller deformation in the composites. The effective interfacial interaction between fiber and matrix, which can be clearly noticed, offered efficient loading transfer. This also induced the deflection of the propagation route, resulting in further mechanical property improvement. Agglomerations of GNPs in excessive resin, voids, and fiber-matrix gaps may, however, act as defects that cause composite material depreciation leading to the degradation of material properties.

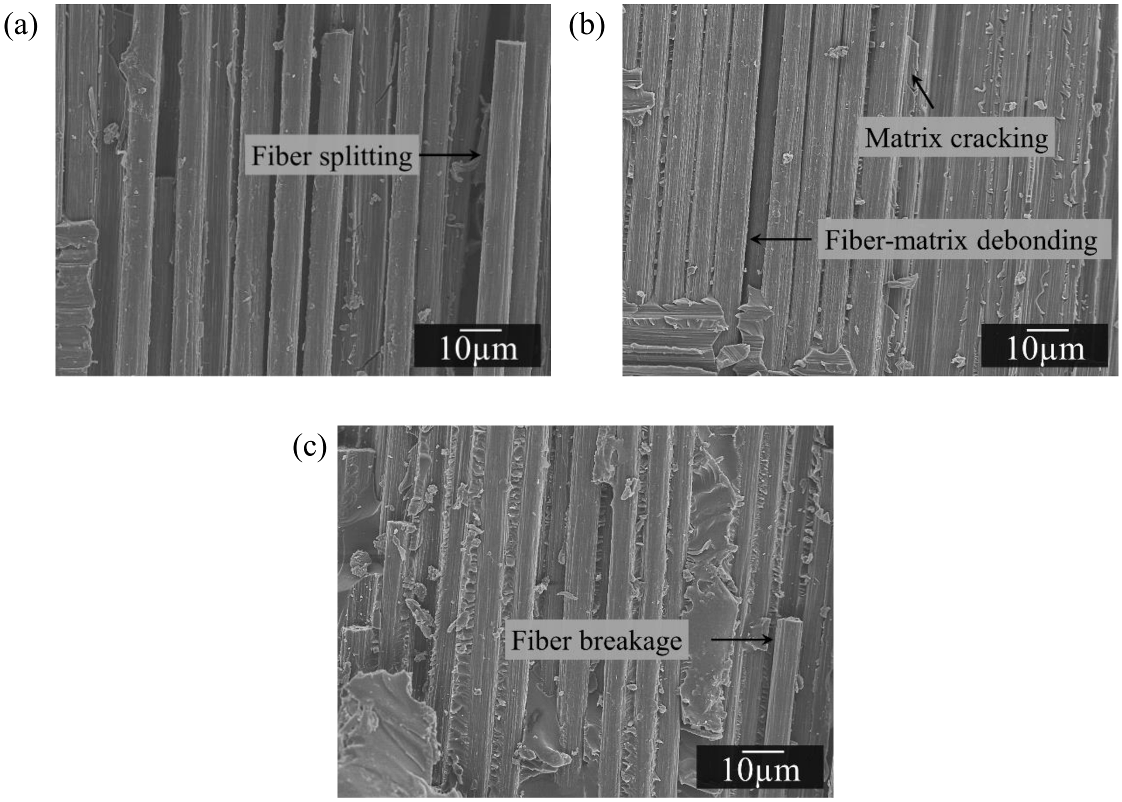

Figure 5-12. SEM images of the impact fracture surfaces of (a) CF, (b) FF, and (c) 0.2G/FF.

5.2.4 Electrical conductivity

Fuzzy fiber and the integration of GNPs into fuzzy fiber composites not only influenced mechanical properties but also their functional conductivity. The electrical conductivity measurements of CFRP and fuzzy fiber composites with different percentages of GNPs that were fabricated by wet lay-up and autoclave curing are shown in Figure 5-13. The synthesis of CNTs on nickel thin film-deposited carbon fiber fabric leads to electrical conductivity enhancement in the fiber, surface, and thickness directions. Furthermore, the incorporation of GNPs has further improved electrical conductivity in all directions. Figure 5-13 presents the enhancement of electrical conductivity in the fiber (120%), surface (400%), and through-thickness (440%) directions for the fuzzy fiber composites compared to the reference CFRP composites. A 1D structure of CNTs can act as bridges in the epoxy resin forming electrical contacts and increasing the number of electrical percolation pathways to enhance electron transport on carbon fiber surfaces and within interlaminar regions. The improvement in surface direction suggests CNTs are transported electrons through adjacent plies bridging the insulating gap between fiber and electrical probe. This is because CNTs form electrical pathways in the interlaminar regions in outermost plies. Therefore, the enhancement may originate from the modified uppermost ply that CNT growth generating electrical contacts on the surface and an increasing number of electrical percolation pathways. In the case of thickness direction, CNTs act as the bridges transferring electrons between electrically insulating interlaminar regions and ply to an electrical probe. Therefore, the improvement of electrical conductivity in through-thickness direction is a result of the expanding number of electrical percolation pathways with the interlaminar regions.

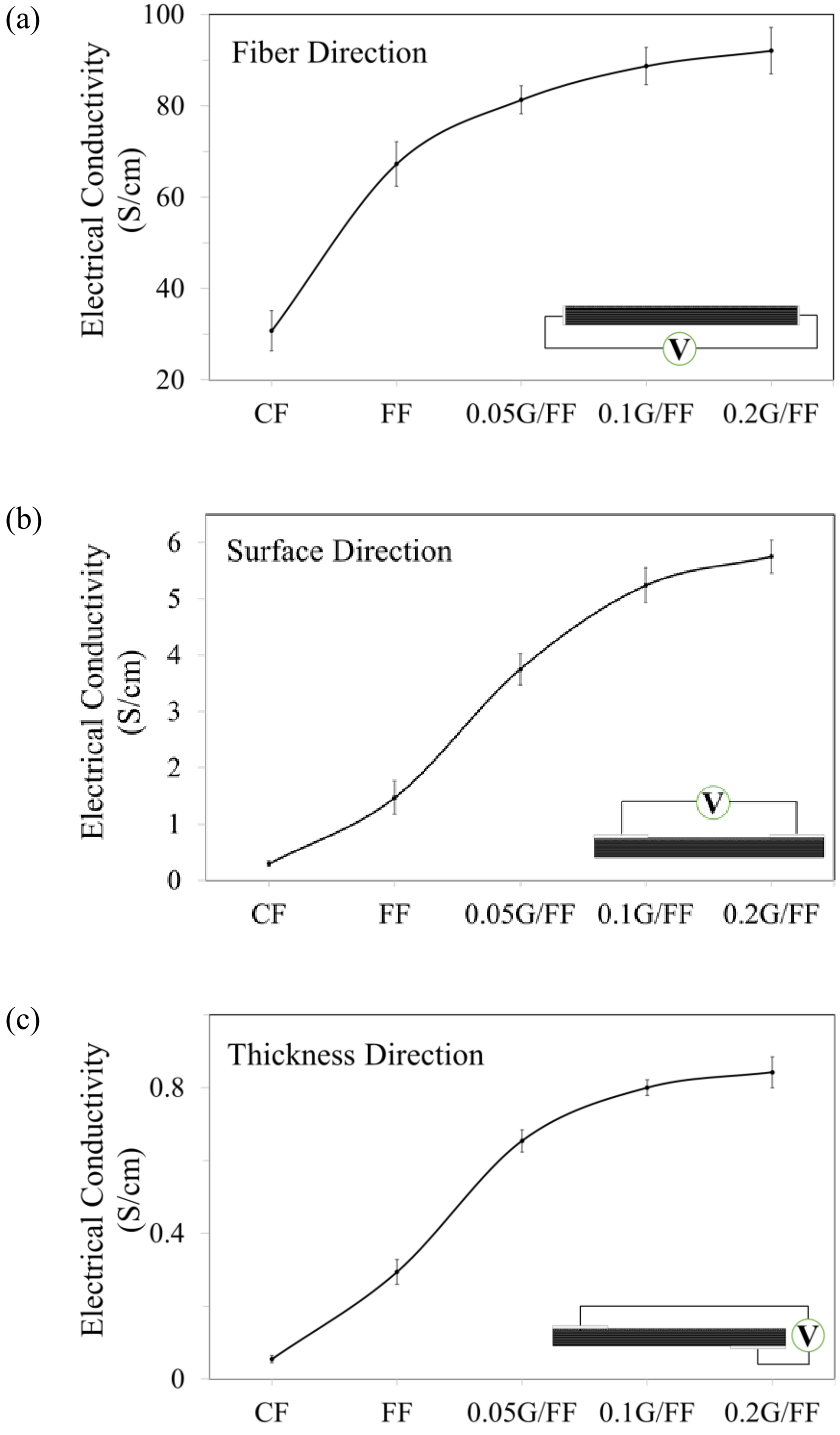

Figure 5-13. Electrical conductivity results of CFRP and fuzzy fiber composites with and without GNPs in (a) fiber direction, (b) surface direction, and (c) thickness direction.

The sufficient content of carbon-filler nanostructures can further offer good physical contact within the insulating epoxy interfaces. Hence, the increase of crosslinking degrees and the suitable gap between neighboring CNTs can be attributed to the tunneling effect allowing electrons to flow or jump from one CNT to another through an insulator [145]. The incorporated GNPs on the surface of the fuzzy fiber further enhanced the electrical conductivity of composites in the in-plane and out-of-plane directions due to the high electrical conductivity of graphene, which is approximately 10^8 S/m [146]. The typical conductivity of graphene-polymer composites and GNP/Epoxy is approximately 10^{-2} S/m and 10^{-10} S/m in GNP/epoxy, respectively [29]. Earlier work reported that the electrical conductivity value of GNP/paraffin wax nanocomposites was around 74 s/m [147]. A noticeable variation in electrical conductivity can be influenced by choosing different experimental procedures such as nanofillers (percentage content and preparation process) and composite fabrication methods (wet lay-up with autoclave curing and vacuum-assisted resin transfer molding) according to application requirements. Therefore, GNPs are one of the secondary carbonaceous-based reinforcement candidates. Indeed, they are a consequence of the synergistic interactions of GNPs and CNTs. To further understand the influence of CNT growth and GNP filler content on electrical conductivity, the conductivity of composites was calculated according to the rule of mixture. As expected, the trend of electrical conductivity abruptly increased along with an increase in GNP filler loading until a percolation threshold (critical concentration of filler) was reached. The graph appeared to level off by further increasing the filler loadings of GNPs. The electrical conductivity of fuzzy fibers was 67.26 S/cm in the fiber direction, 1.47 S/cm in the surface direction, and 0.29 S/cm in the thickness direction. The integration of 0.2 wt% GNPs offered significant conductivity improvements of 40%, 300%, and 190% in the fiber, surface, and thickness directions, respectively (opposing fuzzy fibers). Hence, our calculation results suggest that the electrical conductivity of a fuzzy fiber and a modified 0.2wt% GNPs on fuzzy fiber are 614.79 S/cm and 1,011.49 S/cm in the fiber direction, respectively. The increase in electrical conductivity may be attributable to a high lateral-to-thickness ratio of GNPs facilitating the formation of networks for electron transport pathways between adjacent CNTs in the matrix. GNPs also act as an interlayer medium, increasing the number of the conductive path for electrical conduction.

A major finding is that due to the effective synergistic effect of GNPs and CNTs, a conductive network was formed, increasing conductivity even at a very low percentage fraction of GNPs filler. This conductive percolation network structure may facilitate more efficient electron transport throughout the polymer matrix, thus reducing electrical resistivity. The preserved long length of CNTs can effectively bridge the gap between GNPs and GNPs and/or adjacent ply, forming and increasing the number of intra- and interlaminar percolation pathways. At the same time, the effective link between adjacent nanofillers can increase the contact area with the result of a lower contact-resistance providing tunneling resistivity reduction.

Figure 5-14 shows the electrical conductivity results of 8 layers composite modified with 1 or 2 fuzzy fibers at the outermost layer. The attachment of a single layer of fuzzy fiber provided excellent electrical conductivity enhancements of 268% in the surface direction and 154% in the thickness direction. The CFRP composites with 2 layers of fuzzy fiber integration further enhanced the conductivity up to 488% and 188% in the surface and thickness direction compared to the reference CFRP composites, respectively. Hence, the number of fuzzy fiber plies can also affect the conductivity in all directions. These results suggest that the increments of conductivity in both in-plane and out-of-plane may be attributable to the combination of CNTs bridging the insulating layer between adjacent plies, increasing the number of intralaminar percolation pathways, and forming the interlaminar regions in uppermost plies.

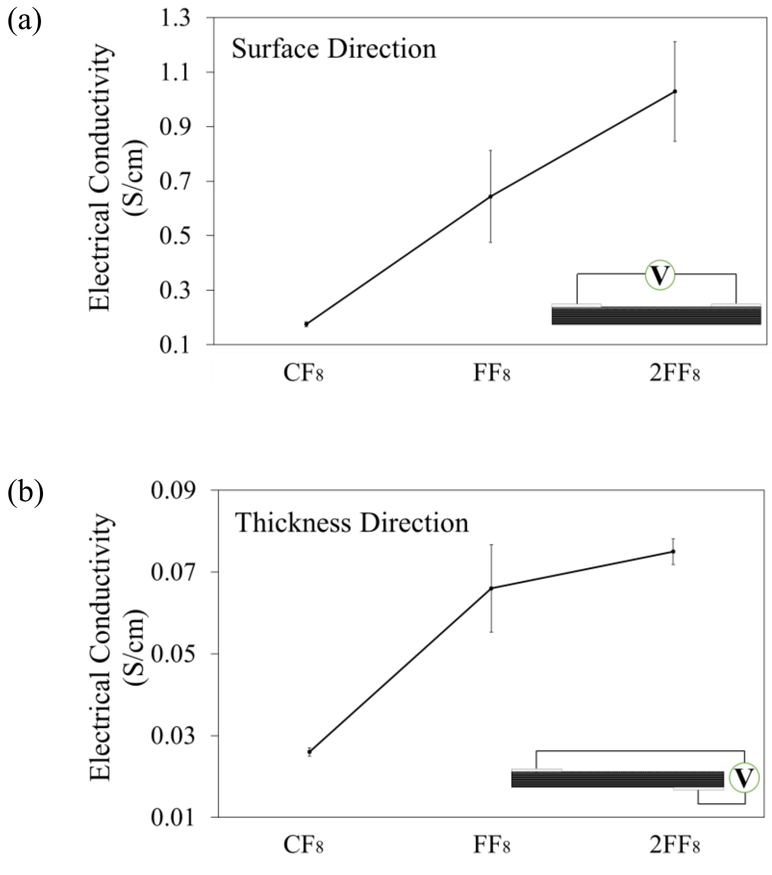

Figure 5-14. Electrical conductivity results of CFRP and fuzzy fiber composites (8 plies) with and without GNPs in (a) surface direction and (b) through-thickness direction.

5.2.5 Thermal conductivity

CFRP composites are characterized by their anisotropic and lack of thermal conductivity, especially in the through-thickness direction. Figure 5-15 presents the thermal conductivity results on CFRP and fuzzy fiber composites with and without GNPs in the through-thickness direction. The thermal conductivity of conventional CFRP composites was 1.29 ± 0.14 W/mK because CFRP composites typically display poor and anisotropic thermal conductivity. The conductivity of composites is normally 10 W/mK and 1 W/mK in the surface and thickness direction, respectively, that much smaller than metals [20]. MWNTs are an ideal type of CNTs as the concentric cylindrical structure reduces phonon scattering. The longer length of CNT accommodates a wider range of phonon frequencies so it can increase the thermal conductivity [148]. The thermal conductivity of fuzzy fiber composites was 1.845± 0.078 W/mK, which was approximately 43% improvement in the thickness direction. These radially CNTs grown on the carbon fiber fabric was expected to enhance phonon coupling. Furthermore, it can also minimize phonon scatter from the interlaminar regions that are dominated by the thermally insulating polymer matrix. This is because the implementation of CNTs grown was used as bridges between adjacent conductive fibers. This can enhance phonon transfer across adjacent fibers in the through-thickness direction improving conductive thermally property. However, the addition of different percentage GNPs onto fuzzy fiber demonstrated insignificant enhancement compared with fuzzy fiber composites. The defective phonon transport between fibers may cause by the poor GNPs interfacial interaction in epoxy and with CNTs.

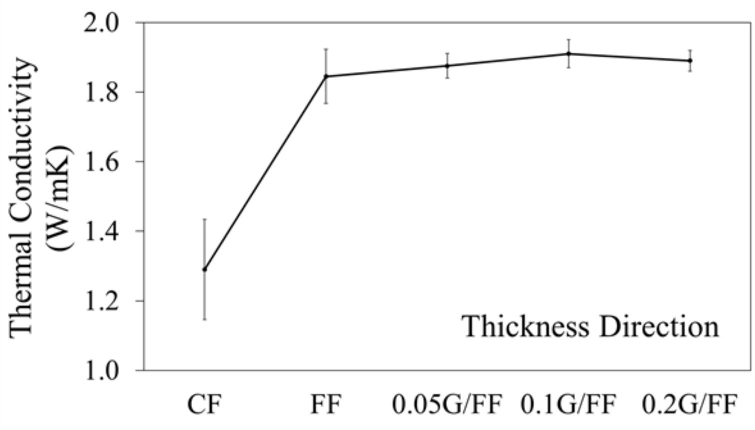

Figure 5-15. Thermal conductivity results of CFRP and fuzzy fiber composites with and without GNPs in the out-of-plane direction.

5.3 Summary

Fabrication methods could affect the mechanical properties of the composites. Composites that were fabricated by wet lay-up with an autoclave curing process revealed better mechanical properties, including flexural, ILSS, and impact toughness properties compared with those of composites using the VARTM fabrication method.

Fuzzy fiber composites displayed increased electrical conductivity of around 120%, 400%, and 440% in the fiber, surface, and through-thickness directions, respectively. The conductivity was increased by more than 3 times in the fiber direction, 20 times in the surface direction, and 15 times in the thickness direction over reference laminates, due to the inclusion of GNPs at 0.2 wt%. The thermal conductivity of the composites improved 43% in the thickness direction with the modification of fuzzy fiber. This is because CNTs can improve phonon coupling reducing phonon scatter from the interlaminar regions that are dominated by the thermally insulating polymer matrix. However, the integration of 0.1wt% GNPs onto fuzzy fiber composites provided better improvements in mechanical properties, including flexural strength (20%), flexural modulus (22%), ILSS (30%), and impact toughness (25%) with high electrical conductivity. The simultaneous incorporation of GNPs and CNTs into composites offers an improvement in electrical conductivity without adversely affecting mechanical properties. These enhancements were much higher than those of reference composites, confirming that synergistic physical interactions can promote both efficient electron transport and load transfer by extending the crack propagation route. Therefore, the novel conductive carbon fiber proposed here could potentially minimize damage to composite materials and lead to more resilient materials. According to this study, the development of conductive carbon fibers enhances electrical and mechanical properties and provides an alternative material to open up new opportunities for a variety of innovations and broad industrial applications.

CHAPTER 6

STUDY OF LIGHTNING-INDUCED DAMAGE DEVELOPMENT ON CFRP COMPOSITE WITH/WITHOUT AN LSP LAYER

The carbon-based LSP system fabricated in Chapters 3 and 4 is essential to enhance mechanical properties and functional conductivities of CFRP composites towards further investigating lightning-induced damage propagation in composite based on experimental and numerical simulation. Metal sheets are used as a primary material in aircraft structures due to their excellent electrical and thermal conductivities, which allow electrical current to travel on the exterior aircraft skin and instantly exit through other extremity points (e.g., wingtips, tail) [149]. However, recent developments in aircraft design involving non-metallic skins and lightweight structural concepts have used carbon fiber reinforced polymers (CFRP), which have high orthotropic electrical resistivity and therefore increase aircraft vulnerability to the effects of lightning strikes. Considerable damage could be observed in the low electrical conductivity materials as they have absorbed high electrical energy during a lightning strike due to the increase of Joule heating. With the concern about extensively using composite materials in aircraft structures, a number of studies have experimentally investigated the damage mechanism in CFRP composites under artificial lightning strikes. Yin et al. [150] conducted an artificial lightning strike test to examine the relationship between stacking sequence and damage size on the formation of different damage forms in woven laminates by visual inspection and damage peeling approaches.

Finite element (FE) analysis of composites exposed to simulated lightning currents has been extensively conducted to assess lightning damage propagation modes because experimental tests of artificial lightning strikes require a high-energy voltage generator, which poses safety concerns. The suitable variables and model conditions can be designed and optimized for cost and time efficiency because no specimen fabrication or testing is required. Thus, FE software is a useful method to predict lightning strike damage propagation to obtain insights into the damage mechanism of lightning-induced thermal response in composites. Ogasawara et al. [151] analyzed a coupled thermal-electrical model to investigate damage resulting from anisotropic thermal and electrical conductivities of unidirectional carbon fiber composites in the thickness direction due to epoxy decomposition and carbon fiber sublimation. Muñoz et al. [152] developed an FE model to ascertain damage in a composite that had been struck by lightning, including Joule heating and electromagnetic/acoustic pressure that arched around the attachment areas. Li et al. [153] considered resin pyrolysis damage in CFRP laminates due to temperature-dependent material properties caused by variations in the peak current and waveform parameters. Yin et al. [154] investigated lightning strike ablation damage in simulated composite models with metallic fasteners. Liu et al. [155] addressed the blow-off impulse effect, a highly explosive burn procedure, in a coupled electrical-thermal numerical model to investigate lightning strike damage behavior in composites.

The considerable damage in CFRP composites caused by the Joule heating effect is created by the extremely high lightning current that generates severe heat. High thermal loads may cause matrix decomposition, fiber breakage, and composite delamination, which degrades composite performance. To withstand lightning strikes with less adverse effects, the inclusion of conductive metallic meshes of Al or Cu have been fabricated on top of composites to create a lightning current path to the ground [156]. These materials have the high conductivity and heat of vaporization necessary to manage the massive current levels of a lightning strike. Hence, the development of functional conductivity is a basic requirement for lightning strike protection (LSP) applications in aircraft structures to solve important electrical and thermal management issues, such as discharging the lightning current away from critical areas. The principal objective of an LSP structure, which acts as a Faraday cage, is to minimize damage and prevent composites by creating electrically conductive pathways when exposed to high lightning currents; namely, to conduct the lightning current away on the exterior skin of the aircraft. Metal meshes or foils made of copper (Cu) or aluminum (Al) are commercially used in LSP structures by application on the composite surface of the aircraft. Lee et al. [157], Khalil et al. [158], and Abdelal et al. [159] examined the effectiveness of metal mesh or coating protection on CFRP laminates. However, these materials are comparatively heavy with lower corrosion resistance and are weakened by the adjacent materials between the metals and composites.

The functional and mechanical properties of CFRP composites can be enhanced by integrating carbon-based nanofillers into the polymer matrix [14,34,160-165].

Kruckenberg et al. [138] proposed electrically conductive surface films, paints, or primers made of integrated nano-reinforcement, such as carbon nanofiber, Cu powder, metal-coated carbon nanotubes (CNTs), single-walled carbon nanotubes (SWNTs), or graphite nanoplatelets in polymers to protect aircraft structural composites against lightning strikes. Multi-walled carbon nanotubes (MWNTs) are lightweight carbon-based nanofillers with excellent functional conductivity and can be fabricated as an effective LSP layer [166]. The electrical and thermal conductivities of MWNTs have been reported 5×10^4-1×10^6 S/m and 3,000-6,000 W/m·K, respectively [34]. The incorporation of MWNTs in the polymer matrix can enhance mechanical properties, functional conductivities, and thermal stability [167]. Soykasap et al. [168] and Ma et al. [34] proposed CNT-doped epoxy resin for effectively reducing the thermal damage region in CFRP composites because of high electrical conductivity, especially in the thickness direction. However, composites are jeopardized under increased loads as a consequence of high polymeric viscosity and filler agglomeration due to van der Waals forces. Once the loading level is limited, the high electrical and thermal conductivities of the composite cannot fulfill the requirements of an LSP system. CNT paper, buckypaper, or fuzzy fiber (FF) can alleviate non-uniform dispersion problems and strengthen fiber-matrix interfacial adhesion. The FF fabric is synthesized by growing CNTs on the carbon fiber surface. The FF layer can improve the mechanical properties and functional conductivities of a structural laminate [101], making them effective for the LSP layer to replace traditional metallic materials. As a new approach to the LSP system, Kumar et al. [169] experimentally investigated the damage evolution of CFRP composites with MWNT buckypaper interleaved in each lamina. Chu et al. [16] developed a sesame-cookie topography silver nanoparticle in CNT paper placed on the outermost CFRP layer. The results demonstrated an increase in electrical conductivity and mechanical properties that increased the LSP effect in composites. Han et al. [15] and Fu et al. [170] focused on LSP effectiveness and damage mechanisms in composites using CNT buckypaper-based coating on the top insulating adhesive layer. Limited experimental and numerical studies have reported the thermal damage behavior in CFRP composites with FF layer under lightning strike.

In this Chapter, we conducted artificial lightning tests to determine the appearance and size of damage on woven CFRP and FFRP composites. Simulated composites with a carbon-based LSP layer fabricated by direct CNTs grown on the composite are scarcely reported. Hence, a coupled thermal-electrical analysis model based on COMSOL simulations subjected to lightning currents was also used to assess the thermal damage response of unprotected and FFRP composites for comparison with the experimental results and to increase model accuracy. We also investigated matrix decomposition under different LSP functional property effects by improving functional conductivities in the outermost ply of composites to better understand the thermal damage mechanism. The results provide insights into lightning-induced damage evolution and potential thermal damage mitigation in underlying composites by integrating a high electrical conductivity FF layer on CFRP composites for performance enhancement.

6.1 Experimental section

6.1.1 Materials and composite preparation

Plain weave T300 carbon fiber fabric was supplied by Sigmatex Composite Materials Company, China. Epoxy resin (Bisphenol-A DiGlycidyl Ether) and amine-based curing agent hardener were obtained by Wells Advanced Materials, China. Woven CFRP composites with and without LSP layer were fabricated by wet lay-up. The composite specimens were then cured in an autoclave at 50°C for 4 hours, followed by post-curing at 150°C for 3 hours at pressures of 0.3 MPa. The CFRP laminates consisted of 16 plies with a [(0/90F)] stacking sequence. The anti-lightning protection layer was fabricated by direct synthesis of MWNTs on the carbon fiber fabric to form an FF fabric that can be referred to Chapter 4. The FFRP composite was fabricated by integrating the FF fabric in the outermost ply of the composite. The volume fraction of fiber (V_f) identified by thermogravimetric analysis (TGA) was approximately 58% in CFRP composites and 63% in FFRP composites (CNT volume fraction of 5%). The dimension of the laminate specimens was 150 × 100 × 3.52 mm with reference to ASTM D7137 [171].

6.1.2 Simulated lightning strike test

The lightning strike was simulated by a high-current generator at the Beijing Research Center in Commercial Aircraft Corporation of China, Ltd. (COMAC). Figure 6-1 shows the artificial lightning strike test setup. The test specimen was wrapped by Cu foil tape and placed between two columns on the two short edges. An electrode width diameter of 10 mm was located at the center of the specimen surface. The current waveform of component D was set to approximately 20 kA peak current over a 100-μs duration. The discharge gap between the electrode and the CFRP surface was less than 1 mm. The morphology of the CFRP composites after simulated lightning treatment was investigated using a digital camera and C-scan ultrasonic flaw detector device.

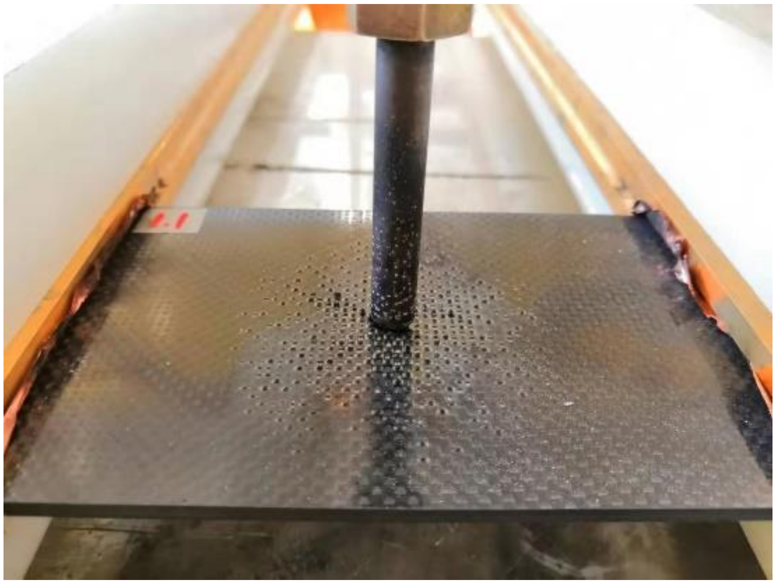

Figure 6-1. Configuration of a simulated lightning impact high impulse current generator.

Lightning current waveforms are used to evaluate the direct and indirect effects of damage in aircraft structures and avionics, which are defined by standard MIL-STD-464 [41]. These current waveforms can be divided into four components (initial stroke, intermediate current, continuing current, and restrike) with key characteristics of peak amplitude, charge transfer, action integral, and time duration, as shown in Figure 6-2. Components A and D represent two peak amplitudes of 200 and 100 kA, respectively, with a duration of 500 μs; these figures are substantially higher than those of components B and C. These high currents generate extreme heat burning composite materials. According to SAE ARP 5412B [172], the double exponential equation of standard current waveforms is described as

$$I(t) = I_0 (e^{-\alpha t} - e^{-\beta t}) \tag{6-1}$$

where I_0 is a current constant, α is the reciprocal of the wave tail time constant, β is the reciprocal of the wave front time constant, and t is time duration. The exponential current waveform equation can be also explained by front time (t_1) and tail time (t_2); t_1 represents the time from 10% to 90% of the maximum current and t_2 represents the time to half of the maximum current, as shown in Figure 6-3.

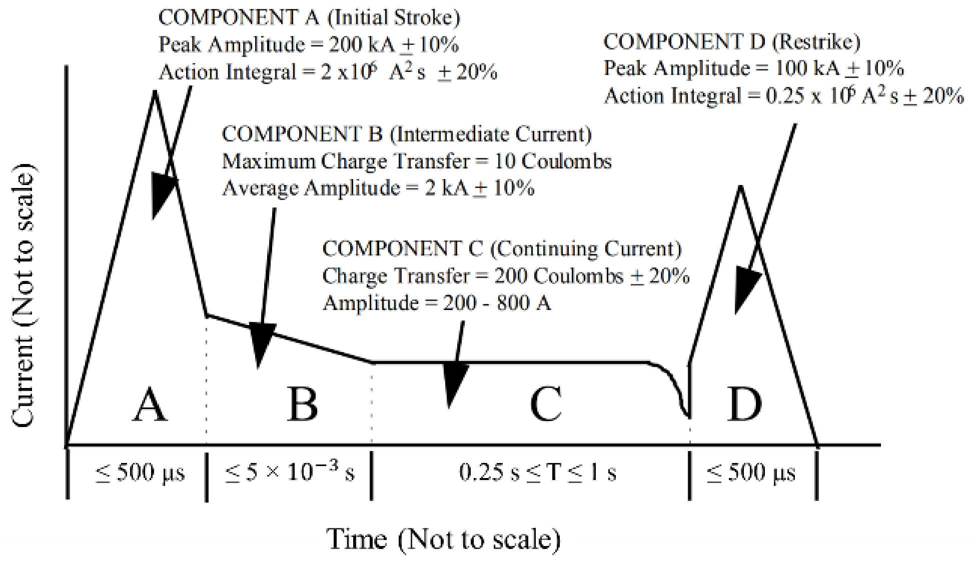

Figure 6-2. Standard lightning current waveforms.

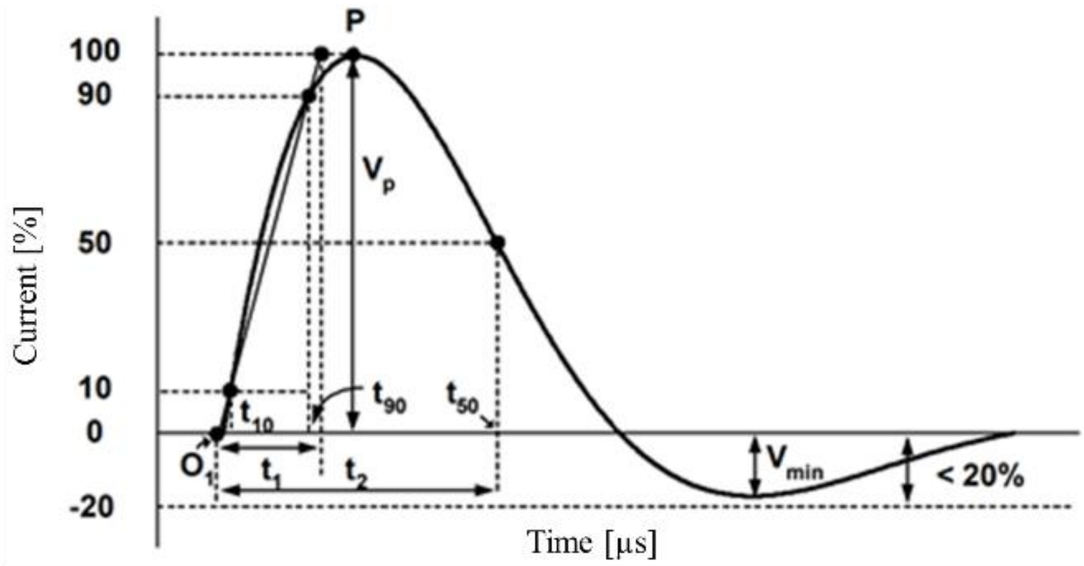

Figure 6-3. Double exponential impulse current waveform.

6.2 Finite Element model

6.2.1 Theory

Coupled thermal-electrical analysis was simulated using the numerical model COMSOL. The steady-state, transient, and linear/non-linear temperature field distribution is obtained when the relevant boundary and loading conditions are provided. Based on the electrical field aspect in a conducting material, the reduced Maxwell's equation of charge conservation with steady-state direct current can be calculated as

$$\int_S J.ndS = \int_V r_c dV \tag{6-2}$$

where V is the control volume with surface S, n is the outward normal to S, J is the electrical current density (current per unit area), and r_c is the internal volumetric current source per unit volume. The electrical current flow can be described by Ohm's law:

$$J = \sigma^E \cdot E = -\sigma^E \cdot \frac{\partial\varphi}{\partial x} \tag{6-3}$$

where σ^E, E, and φ are electrical conductivity, electrical field intensity, and electrical potential, respectively. An increase in potential occurs when a charged particle moves against the electrical field so that the gradient direction is opposite to the electrical field. According to Joule's law, the amount of electrical energy (P_{ec}) dissipated by the current flow through a conductor is

$$P_{ec} = J \cdot E = \frac{\partial \varphi}{\partial x} \cdot \sigma^E \cdot \frac{\partial \varphi}{\partial x} = E \cdot \sigma^E \cdot E \tag{6-4}$$

where P_{ec} is evaluated at time $t + \Delta t$ under steady-state conditions, and the average P_{ec} can be calculated over the time increment as

$$P_{ec} = \frac{1}{\Delta t} \int_{\Delta t} P_{ec}\, dt = E \cdot \sigma^E \cdot E - E \cdot \sigma^E \cdot \Delta E + \frac{1}{3} \Delta E \cdot \sigma^E \cdot \Delta E \tag{6-5}$$

According to the basic energy balance, heat conduction behavior can be written as

$$\int_V \rho \dot{U} \delta\theta dV + \int_V \frac{\partial \delta\theta}{\partial x} \cdot k \cdot \frac{\partial \theta}{\partial x} dV = \int_V \delta\theta r_c\, dV + \int_S \delta\theta q\, dS \tag{6-6}$$

where ρ is the material density, $\dot{U}$ is the internal energy, k is the thermal conductivity, r is the heat generated within the body, q is the heat flux per unit area, and $\delta\theta$ is an arbitrary variation field that satisfies the essential boundary conditions. Due to the nonlinear thermal-electrical problem, the electrical conductivity depends on temperature whereas internal heat generation within the body is a function of electrical current.

6.2.2 Numerical model

A coupled thermal-electrical analysis, referring to the Joule heating governing equation, was used to determine the damage effects by heating from the high electrical current. The temperature distribution of the CFRP composites was used to predict matrix delamination and fiber ablation damage in the in-plane and out-of-plane directions using COMSOL. The simulated plain weave CFRP composite model contained 16 plies (ply thickness of

0.22 mm) in a sequence of [(0/90F)]. A 150 × 100 mm composite was modeled for the simulated lightning strike tests. An unprotected woven CFRP composite served as a reference composite. The temperature-dependent density of the CFRP composites can be described by the rule of mixtures. The density of carbon fiber and epoxy resin are 1.76 g/cm^3 [173] and 1.1 g/cm^3 [174,175], respectively. The fiber volume fraction of the CFRP composites was assumed to be 58%, corresponding to the specimens in the Experimental section. The electrical conductivity at room temperature was also determined using the rule of mixtures. The electrical conductivity of carbon fiber (T300) is 58,824 S/m [173]. Due to the insulating epoxy resin, the electrical conductivity is very low and can be neglected here. The electrical conductivity in the transverse direction is much smaller than that in the longitudinal direction for unidirectional fiber lamina. In the case of woven fabric CFRP lamina, the electrical conductivity in the transverse direction is equal to that in the longitudinal direction, while the electrical conductivity in the thickness direction is approximately 1×10^{-6} times the electrical conductivity in the longitudinal direction. The in-plane and out-of-plane electrical conductivity were quite different due to resin-bonded between fibers in the thickness direction. Once the epoxy has fully decomposed, the thickness electrical conductivity was assumed to be 2000 S/m [159]. The temperature-dependent material properties of CFRP composite including density, specific heat, thermal conductivity, and electrical conductivity were calculated and acquired from the published literature, as listed in Table 6-1. The local temperature-dependent composite properties were adjusted using linearly interpolating the properties between the given temperature in Table 6-1.

Table 6-1. Material properties of the carbon fiber/epoxy plies [159,173].

Temperature (°C)	Density (kg/mm^3)	Specific heat (J/kg·K)	Thermal Conductivity		Electrical Conductivity	
			Long & Trans (W/mm·K)	Thickness (W/mm·K)	Long & Trans (S/mm)	Thickness (S/mm)
25	1.48 E-6	1,065	0.008	0.00067	34.12	3.412E-5
343	1.48 E-6	2,100	0.002608	0.00018	34.12	3.412E-5
500	1.02 E-6	2,100	0.001736	0.0001	34.12	2
510	1.02 E-6	1,700	0.001736	0.0001	34.12	2
1000	1.02 E-6	1,900	0.001736	0.0001	34.12	2
3316	1.02 E-6	2,509	0.001736	0.0001	34.12	2
>3316	1.02 E-6	5,875	0.001015	0.001015	0.2	1.0E+06

Criteria for matrix decomposition prediction

Thermal damage (e.g., carbon fiber ablation, matrix decomposition, sublimation) results in composite degradation. In the simulation model, irreversible matrix decomposition was generated based on localized temperature variation. The temperature range of matrix degradation in the CFRP composite is defined from 300 °C to 500 °C, which was evaluated by thermogravimetric analysis (TGA) in Chapter 4. The composite latent heat of epoxy matrix decomposition was assumed to be 4.8×10^3 kJ/kg, which was released between 300 °C to 500 °C. A linear rate of decomposition was assumed in the range of matrix decomposition temperature. The increased temperature then caused resin pyrolysis and the matrix decomposition index, *MDI*, was calculated as

$$MDI = \frac{T - T_0}{T_f - T_0} \tag{6-7}$$

where T is the temperature of composite, T_0 is the temperature of the initial matrix degradation (300 °C), and T_f is the temperature at which complete matrix decomposition occurs (500 °C). The *MDI* equals zero when the temperature is less than the initial matrix decomposition temperature and *MDI* is one when the temperature is higher than the final matrix decomposition temperature. Once the local temperature exceeded 3,316 °C, the fibers began to sublimate with 43×10^3 kJ/kg latent heat of sublimation. Carbon fiber will char with the increase of temperature and eventually ablate in the experimental specimens around 3,316 °C, hence the thermal conductivity was assumed to be isotropic due to irreversible fiber char formation.

During a lightning strike, the electric charge was allowed to transfer to the next intact layer when any regions in the preceding layer have been ablated. Thus, the electrical conductivity in the ablated region was reduced in the in-plane direction to prevent in-plane conduction, but increased in the thickness direction to have high conduction property. Contact properties were also included to characterize heat transfer in the resin-richness interfaces between fiber and epoxy matrix. The electrical conductance of 2.5×10^7 S/m^2 [176] and thermal gap conductance of 500 W/m^{2}K [177] were assumed between composite laminates in this simulation. When the thermal conductivity of epoxy reduced up to 30% due to the thermal decomposition of epoxy resin, the thermal conductance could also be reduced by the same percentage.

The FF layer, which served as an anti-lightning protection layer, was integrated on the outermost CFRP composite and labeled as an FFRP composite. Many properties of the FF layer are not available in the published literature and assumptions in the FF layer properties were made in this simulation. The FF layer was assumed to be orthotropic electrical and thermal conductivities. CNTs were only grown on the surface of woven carbon fiber fabric so the conductivity in the longitudinal direction and the transverse direction was assumed to be the same. The data of electrical and out-of-plane thermal conductivities at room temperature were received from Chapter 5. The through-thickness electrical conductivity was assumed to be equal to the in-plane electrical conductivity when the epoxy has completely decomposed (500 °C). The in-plane thermal conductivity was determined by the average thermal conductivity of composite fuzzy fiber (CFF) with the effect of wavy CNTs being coplanar with the 1-3 and 2–3 planes and carbon fiber thermal conductivity at high temperature [178,179]. The specific heat above 25 °C was assumed to be bulk graphite [180]. The density of FFRP composites was calculated by the rule of mixtures. Material properties of the FF layer were obtained from open literature and experimentally determined by two-probe resistivity measurement and laser flash thermal conductivity analysis, as defined in Table 6-2. The latent heat of vaporization in the FF fabric was assumed to be similar to the woven carbon fiber (43×10^3 kJ/kg) at the sublimation temperature (3,316 °C). CNTs may partially exist in the FF layer above the maximum sublimation temperature of carbon fiber (3,367 °C), so the latent heat, which was released between 3,367 °C - 4,000 °C [181], was assumed to be that of pure carbon

(59.9×10^3 kJ/kg) [182]. The electrical and thermal gap conductance of the FF layer were assumed to be the same as those of CFRP composite to characterize the electrical conductance and heat transfer at the FF layer interface.

Table 6-2. Material properties of the FF/epoxy protection layer [178-180].

Temperature (°C)	**Density (kg/mm^3)**	**Specific heat (J/kg·K)**	**Thermal Conductivity**		**Electrical Conductivity**	
			Long & Trans (W/mm·K)	**Thickness (W/mm·K)**	**Long & Trans (S/mm)**	**Thickness (S/mm)**
25	1.54 E-6	853	0.65	0.00185	6.7	0.029
343	1.54 E-6	1,401	0.20	0.00185	6.7	0.029
500	1.13 E-6	1,598	0.097	0.00185	6.7	6.7
1000	1.13 E-6	1,947	0.097	0.00185	6.7	6.7
1500	1.13 E-6	2,096	0.095	0.00185	6.7	6.7
3000	1.13 E-6	2285	0.091	0.00185	6.7	6.7
3316	1.13 E-6	2285	0.091	0.00185	6.7	6.7
3367	1.13 E-6*	2285*	0.090*	0.00185*	6.7*	6.7*
4000	1.13 E-6*	2285*	0.090*	0.00185*	6.7*	6.7*

*Properties extrapolated of the empirical data over the temperature range (25-3,316˚C)

Due to the high heat generation in the composite from large electric current during lightning strike, the thermal energy of lightning may cause melting, evaporation, and explosive boiling in the LSP layer. The explosive boiling or phase explosion is a process of rapid phase change and only occurs when the target becomes superheated with its temperature far beyond its boiling point. Then, homogeneous nucleation begins when the temperature reaches the superheat limit, which increases closer to the critical temperature. In this study, explosive boiling damage was not considered since it only occurs when the temperature of the LSP layer closes to the critical point. Thus, the ablation mechanism of the LSP layer was assumed to be vaporization only. The flow of vaporized material from the surface (ablation rate) can be described by the Hertz-Knudsen equation [183]:

$$\upsilon(T) = (1-\beta)\sqrt{\frac{m}{2\pi k_B T}}\frac{p_0}{\rho}\exp\left[\frac{L_v}{k_B}\left(\frac{1}{T_B}-\frac{1}{T}\right)\right] \tag{6-8}$$

where m is the atomic mass of material, k_B is the Boltzmann constant (8.31 J/mol.K), L_v is the latent heat of vaporization of the material, T_B is the boiling temperature at the pressure p_0 (1 atm), β the back flux coefficient (0). It was assumed that all molecules can be freely vaporized from the surface of the material. The vaporization and local heat increment could be stopped when the FF layer has been completely ablated or reached the maximum temperature. Thus, the FF layer maximum temperature was used as a simulation threshold.

The thermal material behavior of the LSP system was defined to calculate the total internal energy change during the heat transfer process. The change of material status, which is called a phase transition, consumes a lot of energy (latent heat). Due to the effect of latent heat, the material specific heat can be calculated as

$$C_p = \frac{H_L}{\Delta T_m} + \frac{C_{ps}+C_{pl}}{2} \tag{6-9}$$

where H_L is the material latent heat (melting, evaporation), ΔT_m is the temperature range of phase transition, C_{ps} is the material specific heat before phase transition temperature, and C_{pl} is the material specific heat after phase transition temperature. The change of internal energy due to the heat conduction effect (ΔU_C) is affected by the specific heat of the LSP layer, which can be written as

$$\Delta U_C = \frac{\Delta U}{\Delta T}\Delta T = C_p \Delta T \tag{6-10}$$

The internal energy change due to the Joule heating effect can be calculated as

$$\Delta U_E = \eta P_{ec}\left(\frac{1}{\rho}\right) \tag{6-11}$$

where η is the energy conversion factor (0.92), P_{ec} is the electrical energy dissipated per unit volume, and ρ is the material density. Due to the damage behavior of the FF layer associated with heat conduction and Joule heating, the total internal energy change can be described as

$$\Delta U_T = \Delta U_C + \Delta U_E \tag{6-12}$$

Electrical and thermal boundary conditions were assumed based on the lightning strike tests to improve the credibility of the results. A composite supported at the two short ends was set to zero electrical potential for the grounding current. Due to transient heat transfer, the top and side surfaces radiated heat with 0.9 emissivity for all composites at 25 °C. The bottom surface was adiabatic because zero temperature increment was shown on the bottom surface of the specimen [159]. Surface-to-surface contact was used to applied electrical and thermal gap conductance at the interface between composite laminates. The peak current (20 or 40 kA) with 25/100 μs waveform was directly applied at the center on the composite surface with a 10-mm lightning source diameter [170]. The lightning current waveform corresponds to the experimental conditions, which were used to validate the simulation results. The electrical current is a function of time that can be used to calculate impulse current waveforms of the action integral on the damage extent with regards to high lightning current ablation damage on the composites [41], as shown in Figure 6-4. An explicitly discretized method with 8-node brick elements was constructed on each ply of the composites. A single element was applied in each lamina in the depth direction. The mesh quality was evaluated using different mesh densities, especially in the damage area at the center of the composite surface region. The total element number of composites with and without LSP systems was 15,808. Figure 6-5 shows a simulation model with mesh and boundary conditions.

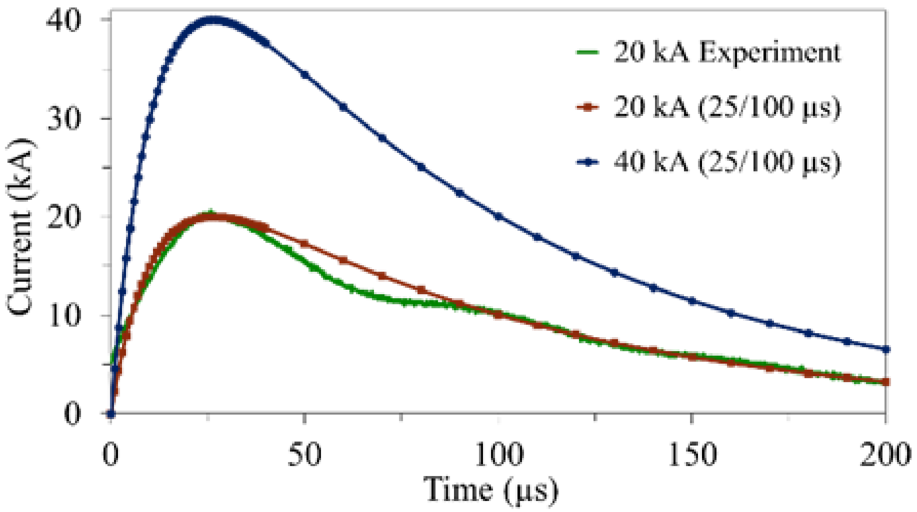

Figure 6-4. Lighting current waveform for 20 and 40 kA with 25/100 μs.

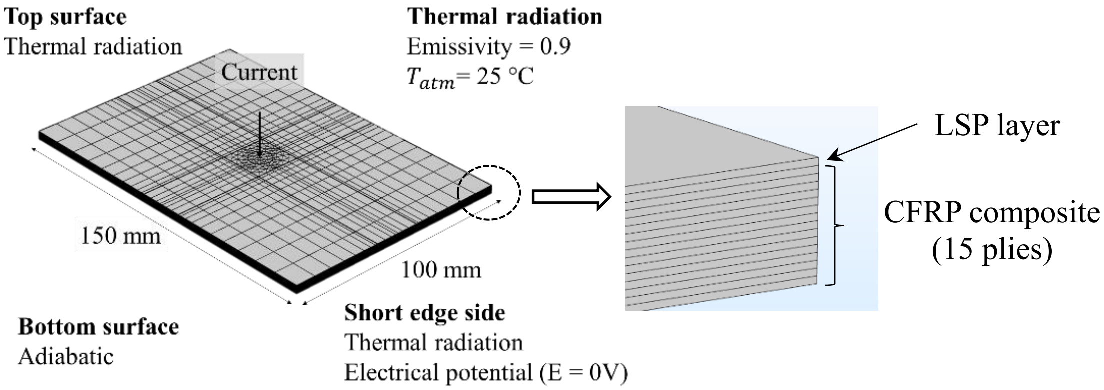

Figure 6-5. Simulation composite model with electrical and thermal boundary conditions subjected to a simulated lightning current.

6.3 Results and discussion

6.3.1 Comparison of simulation and experimental results

The area and appearance of damage from the simulations and experiments were compared to assess model accuracy. Irreversible matrix decomposition damage based on localized heat generation and different material properties was predicted by the numerical simulation model. The maximum lightning current was set to 20 kA with a 25/100 μs waveform in both the experiments and simulation model. The observed and predicted appearance and size of damage on the surface of the unprotected CFRP composite are shown in Figure 6-6. The scale of the figures differs to distinguish the damage development at the lightning attachment location. Figures. 6-6(a) and 6-6(b) show the post-lightning visual damage and ultrasonic C-scanning image in the outermost ply of the CFRP laminate from the artificial lightning experimental test. Figures. 6-6(c) and 6-6(d) show the temperature profile and matrix decomposition degree on the composite surface from the numerical analysis, respectively. The electrical conductivity was equal along with the longitudinal and transverse directions due to the woven fiber material properties; hence, the current penetrated in both directions and generated high resistive heating and resin pyrolysis. The damage is strongly localized in the vicinity of the high current attachment point at the center of the circular pattern and spreads outward along the surface of the carbon fiber direction. This matrix ablation region is revealed over the composite surface in a slightly elliptical shape, including the fiber damage region observed in the ultrasonic C-scan image (Figure 6-6(b)) and simulation model (Figure 6-6(d)).

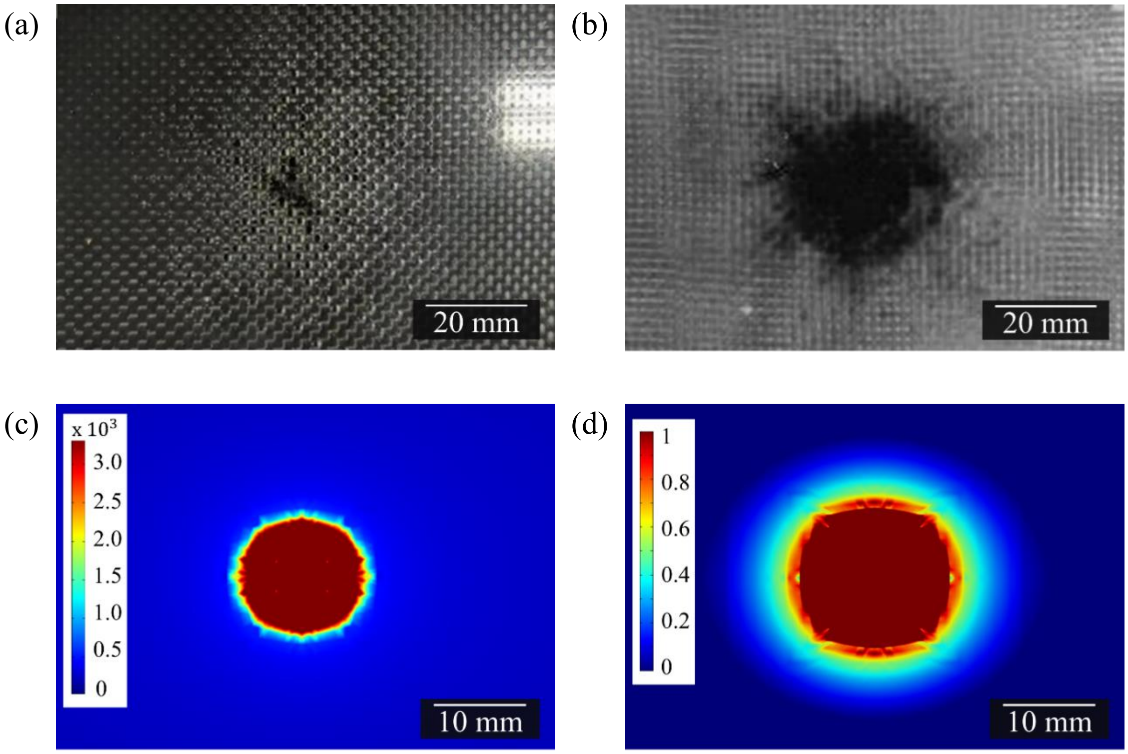

Figure 6-6. Comparison of lightning-induced damage in the outermost ply of CFRP laminate between experiments and simulations: (a) photograph; (b) ultrasonic C-scan image; (c) temperature profile; (d) matrix decomposition.

The FF layer was fabricated by growing CNTs on the carbon fiber fabric, as observed in Chapter 3. An integration of FF layer on the uppermost ply of the CFRP composite serving as an FFRP composite was analyzed to validate the simulation model. The visual and predicted damage inspection on the FF surface at 20 kA nominal peak current is shown in Figure 6-7. Amelioration of the electrical and thermal conductivity in both the in-plane and out-of-plane directions of the FF layer provides improved instantaneous electrical current distribution and reduces localized heat generation. Hence, FFRP composites show a smaller thermal penetration damage region than unprotected composites.

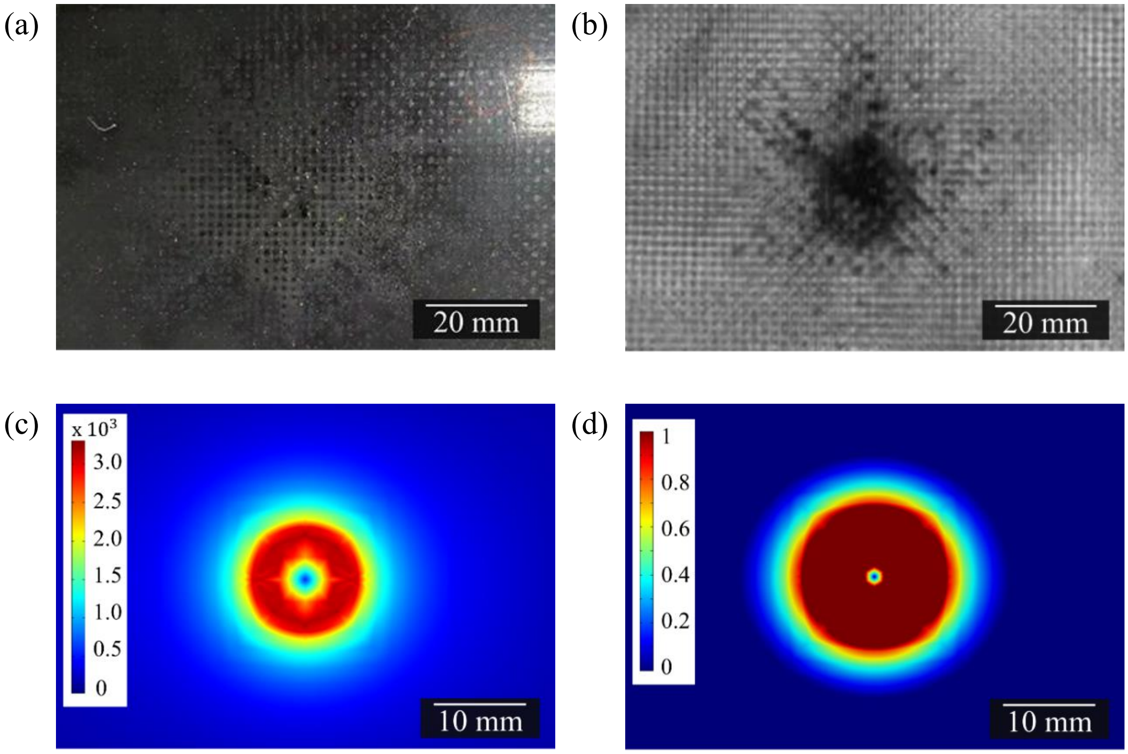

Figure 6-7. Comparison of lightning-induced damage in the outermost ply of FFRP laminate between experiments and simulations: (a) photograph; (b) ultrasonic C-scan image; (c) temperature profile; (d) matrix decomposition.

Table 6-3. Comparison of damage area between experiments and simulations at 20 kA.

Sample	**Experiment**	**Simulation**	**Error (%)**
	Visual damage area (mm^2)	Resin damage area (mm^2)	
CFRP	776	669	−13.81
FFRP	473	418	−11.56

Table 6-3 presents the thermal decomposition area of the experiments and simulations, together with the percentage error of the CFRP and FFRP composites. Both the damage area and appearance of the fiber and matrix damage in the outermost ply of the simulation results correspond well with experimental tests. However, the visual damage from the experiments is somewhat larger than the model predicted damage. The error of matrix decomposition is approximately 13.81% and 11.56% in CFRP and FFRP composites, respectively. These errors might be caused by resistive heating in the coupled thermal electrical analysis. In contrast, magnetic forces, internal expansion pressure, and acoustic shockwave effects may have affected the experiments with regards to the comparative damage area error. The damaged area and appearance of the simulation results match fairly well with the visual damage in the experiments with less than 15% error. The numerical model can therefore be used to simulate high current damage in CFRP composites.

6.3.2 Effects of varying functional conductivities in the LSP system on thermal decomposition damage development

The LSP layer requires high functional conductivity to provide a conduction path for lightning current penetration over the surface to minimize damage and protect the underlying CFRP composites. Hence, the effect of electrical and thermal conductivity in the LSP system was analyzed to understand the lightning-induced damage mechanism from localized heat propagation in the laminate due to Joule heating and heat conduction. The conductivity of the outermost ply in the composite was varied in the in-plane and out-of-plane directions to constrain the electrical and thermal conductivity impact of the LSP system in terms of the extent of thermal damage. The simulated model was subjected to a 40-kA peak current and 25/100 μs waveform for 100 μs. The index of resin pyrolysis of the first underlying ply was between non- and fully-decomposed (0–1). The predicted matrix damaged area in the first underlying carbon fiber lamina and damage depth of the CFRP composite with and without an LSP layer is shown in Figures. 6-8 to 6-11. Figure 6-8 demonstrates considerable heat concentration at the lightning attachment point, resulting in full matrix decomposition damage in a round shape, which then dissipates in the direction of the carbon fiber.

Figures. 6-9 and 6-10 show the predicted damage on the surface of the underlying CFRP ply with enhanced electrical and thermal conductivity by 1–2 orders of magnitude in the LSP ply, respectively. Due to the improvement of electrical conductivity in the in-plane direction, the electrical current is effectively conducted away from the lightning source over the surface and results in less Joule heating generation. Hence, the delamination damage region and intensity are appreciably reduced, as shown in Figures. 6-9(a) and 6-9(b). When only the electrical conductivity in the through-thickness direction increases, the slight reduction of pyrolysis damage area and intensity can be observed in Figures. 6-9(c) and 6-9(d). The electrical conductivity enhancement in the thickness direction of the LSP ply does not efficiently distribute the current through the underlying ply. When the electrical conductivity in both the in-plane and out-of-plane directions of the LSP system are 10 and 100 times higher than the reference composite, respectively, the damage intensity and region of thermal damage penetration are noticeably reduced and practically no thermal damage occurs in the underlying laminate. A smaller amount of heat is generated because of the instantaneous in-plane electrical current flow on the surface. A concomitant electrical conductivity enhancement in both the in-plane and out-of-plane directions can then further minimize heat pyrolysis damage in the depth direction.

Inadequate thermal conductivity in composites cannot instantaneously dissipate heat, which may accumulate at the attachment point and surrounding area and cause thermal damage and composite deterioration. When the thermal conductivity in the in-plane or out-of-plane direction increases by 100-fold from the original material properties, the predicted matrix damage presents an inconspicuous change from the unprotected composites, as shown in Figures. 6-10(a) and 6-10(b). When the thermal conductivity in the in-plane and out-of-plane directions simultaneously increases by a factor of 100, the surface of the underlying ply shows a slight damage area change (Figure 6-10(c)). These results show an insignificant effect of thermal conductivity on the evolution of matrix decomposition in underlying CFRP composites for a short-period simulation.

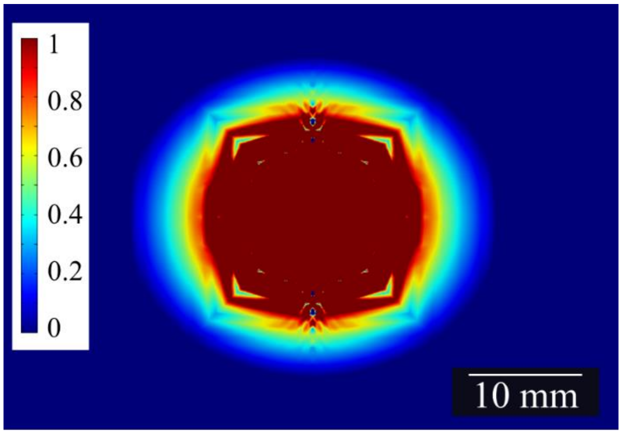

Figure 6-8. Matrix decomposition of unprotected laminate.

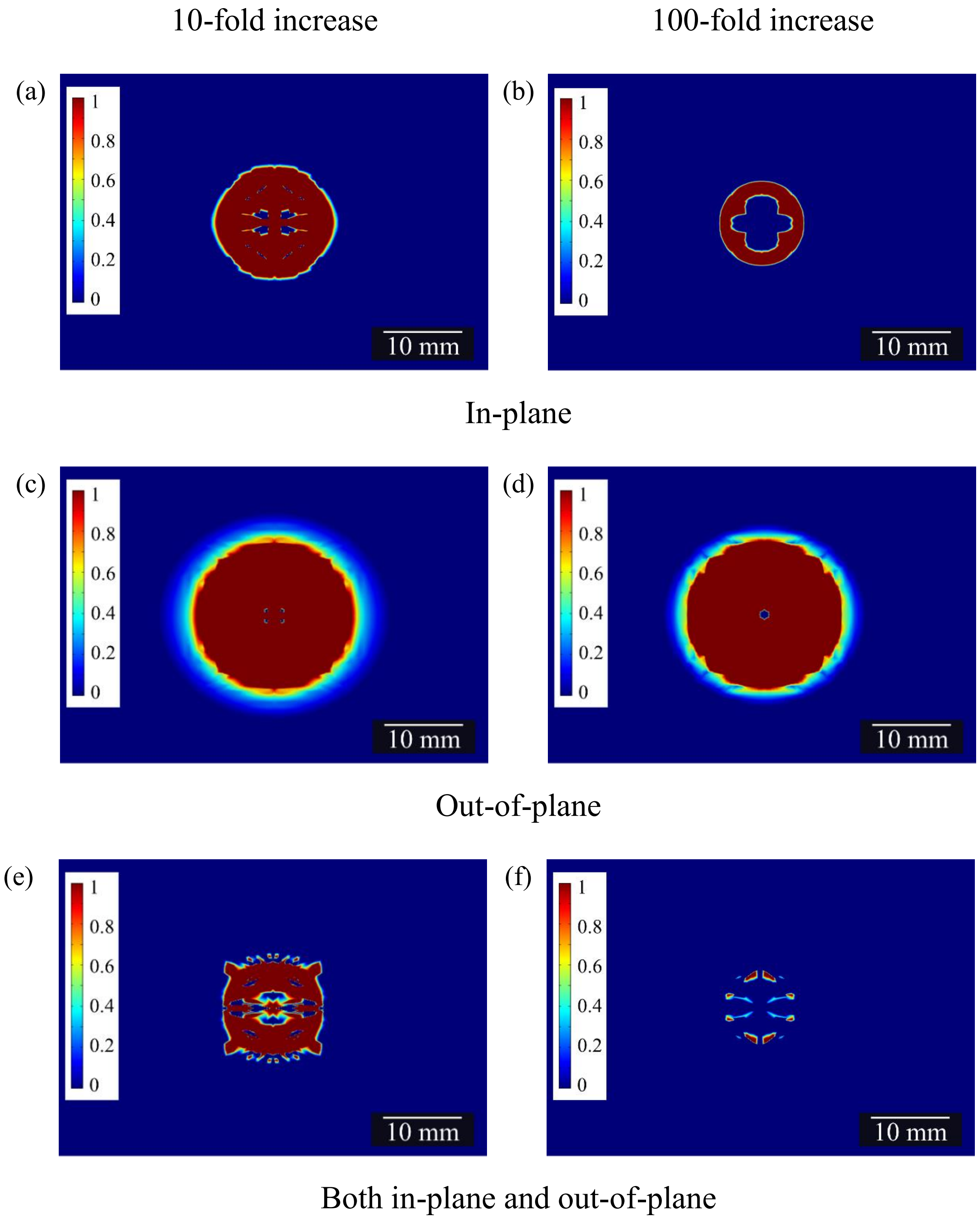

Figure 6-9. Matrix decomposition of underlying CFRP laminate with LSP systems under 10- and 100-fold electrical conductivity enhancement of the (a,b) in-plane, (c,d) out of plane, and (e,f) both in-plane and out of plane directions.

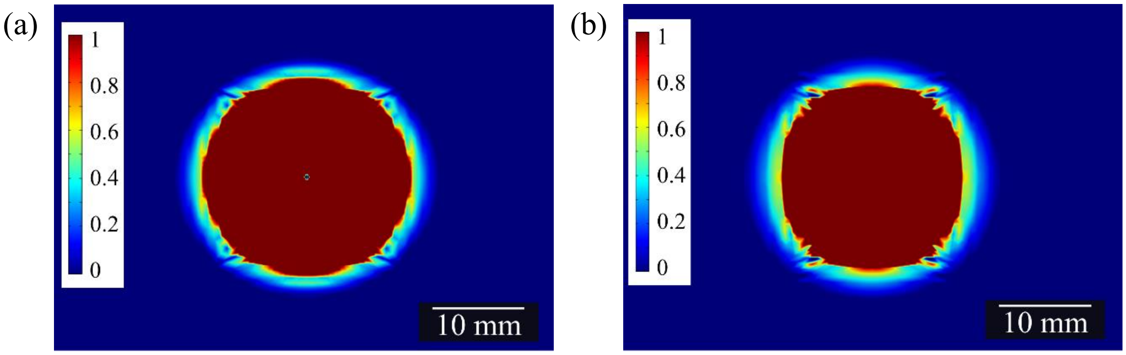

In-plane

Out-of-plane

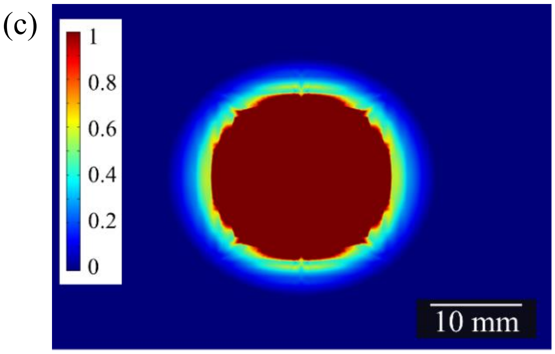

Both in-plane and out-of-plane

Figure 6-10. Matrix decomposition of underlying CFRP laminate with LSP systems with enhanced thermal conductivity of the (a) in-plane, (b) out of plane, and (c) both in-plane and out of plane directions.

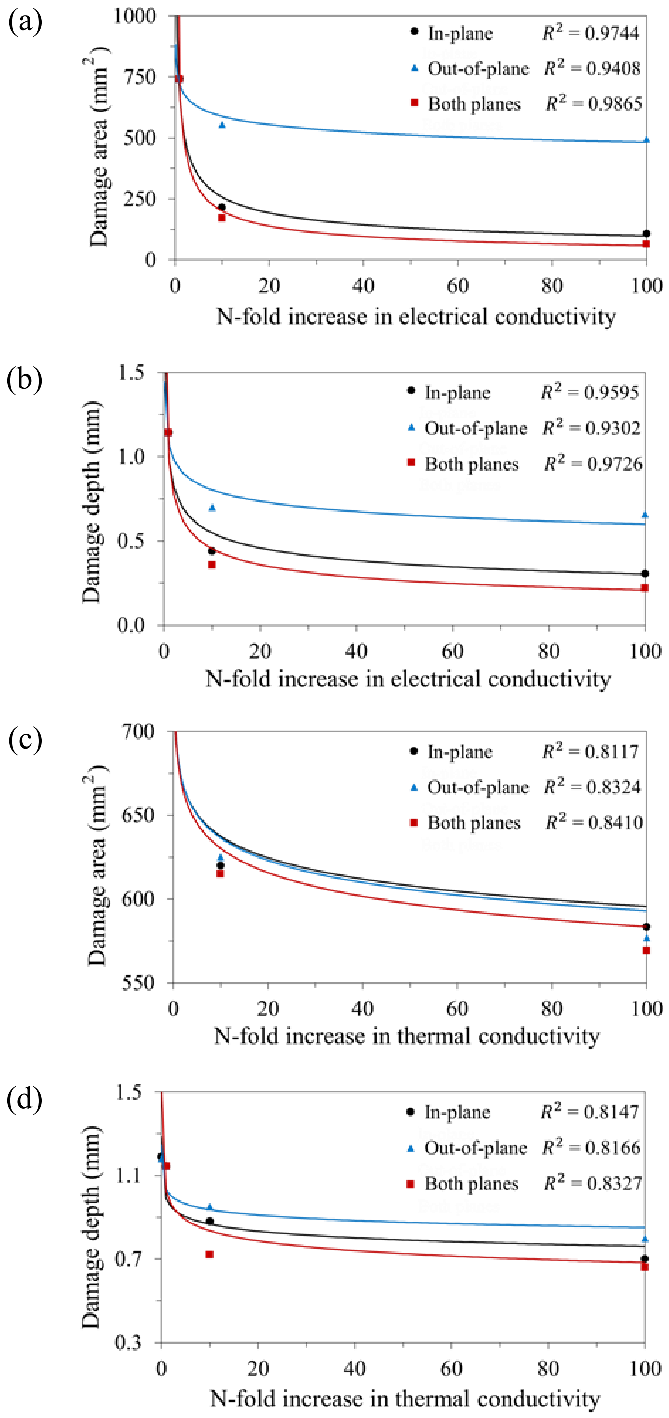

Figure 6-11. Damage area and depth prediction with the conductivity effects in the LSP system of (a) in-plane electrical conductivity, (b) out of plane electrical conductivity, (c) in-plane thermal conductivity, and (d) out-of-plane thermal conductivity.

The relationship between the thermal damage region and conductivity improvement was further investigated using regression analysis to predict the extent of thermal damage in the in-plane and thickness directions of the underlying CFRP composite. Figure 6-11 depicts the results of the damage area and depth concerning the functional conductivity of the LSP system over a period of 100 μs. The R^2 values in Figs. 6-11(a) and 6-11(b) indicate a strong power relationship between matrix ablation in both directions and electrical conductivity. However, the R^2 values that reflect the effects of increased thermal conductivity are lower than those with increased electrical conductivity, which indicates a weaker relationship between damage intensity in both directions and thermal conductivity (Figures. 6-11(c) and 6-11(d)). The electrical conductivity improvement in the LSP layer is significantly reduced the damage area and damage depth of matrix thermal decomposition. Thus, sufficient electrical conductivity in the LSP layer, especially in the in-plane direction, can increase the delay of electrical current distribution to localize heat generation in the composites due to Joule heating and heat conduction. The small change in matrix decomposition in the outermost ply and through-thickness of the underlying CFRP composite is indicated by the effects of thermal conductivity amelioration. These results illustrate the LSP system's ability to minimize ablation damage and deterioration in composites by enhanced electrical conductivity.

6.3.3 Lightning damage propagation in FFRP composites

Electrical conductivity in the LSP system is clearly one of the most important parameters of the underlying CFRP composite during lightning strike damage. Thus, we compared the thermal damage propagation behavior of FFRP with unprotected composites at 40 kA peak current and 25/100 µs current waveform over a 100-µs duration. Once the lightning current reaches the composite, the lack of functional conductivity in the composite may generate high resistive heating. The increased temperature can affect heat dissipation and localized heat generation results in terms of thermal damage, including fiber ablation and resin decomposition. Figures. 6-12 and 6-13 display the temperature distribution profile at the maximum damage region and predicted matrix decomposition, respectively, in the thickness direction of the unprotected and FFRP composites. The temperature in the thickness direction rises abruptly over the first 50 µs in both the unprotected and FFRP composites. The increase in temperature during this period largely originates from resistive heating due to the intense lightning current, which results in resin pyrolysis and carbon fiber sublimation. However, abundant generated heat that cannot be consumed by the composites may cause a rapid change in the depth of damage. A slight temperature increase in the out-of-plane direction is observed after 50 µs in the CFRP with and without an LSP system. A decrease in lightning current can gradually reduce resistive heating, which minimizes heat transfer. The depth of damage, which was controlled by the conducting heat, therefore slowly expands in the composite.

In the case of the unprotected composite, the temperature in the first four plies (0.88 mm) reaches 3,316 °C and then rapidly decreases in the fifth ply between 50 and 100 µs (Figure 6-12(a)). Due to continuous heat penetration up to 100 µs, the composite delaminated up to the fifth interface (~1.1 mm) with temperatures higher than 300 °C. The improved functional conductivity in the FFRP can mitigate the depth of thermal damage penetration so that only the surface of the underlying CFRP composite ply reaches 3,316 °C (0.22 mm), as shown in Figure 6-12(b). It shows that the predicted thermal delamination is limited in the top three plies (0.66 mm) of the FFRP laminate. Figure 6-13 shows that thermal damage penetration in the thickness direction of the CFRP composite with the FF protection layer is better mitigated than that of the unprotected composite because of the conductivity enhancement in the FF ply. The high functional conductivity provides efficient electrical current flow and low resistance heating.

(a) CFRP composite

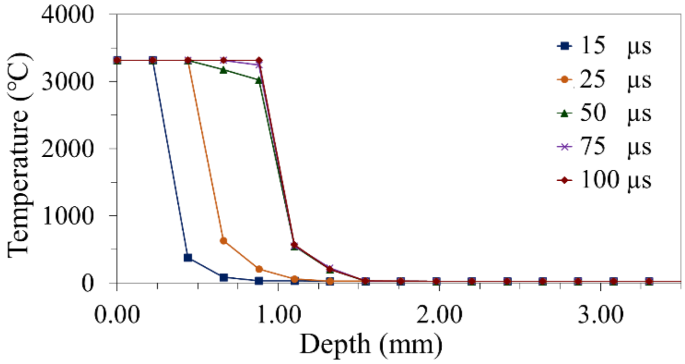

(b) FFRP composite

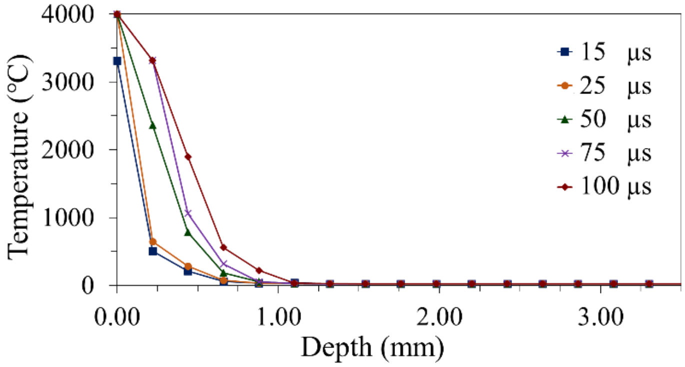

Figure 6-12. Temperature profile in the out-of-plane direction at the maximum damage area of the (a) CFRP composite and (b) FFRP composite.

CFRP composite

(a)

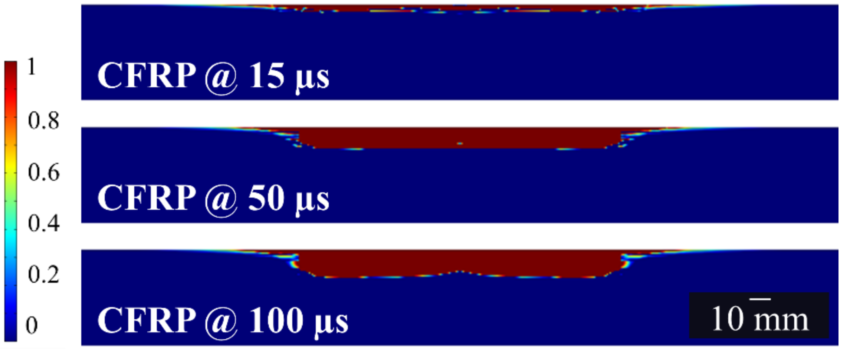

FFRP composite

(b)

Figure 6-13. Predicted thermal damage depth of the (a) CFRP composite and (b) FFRP composite.

CFRP composite

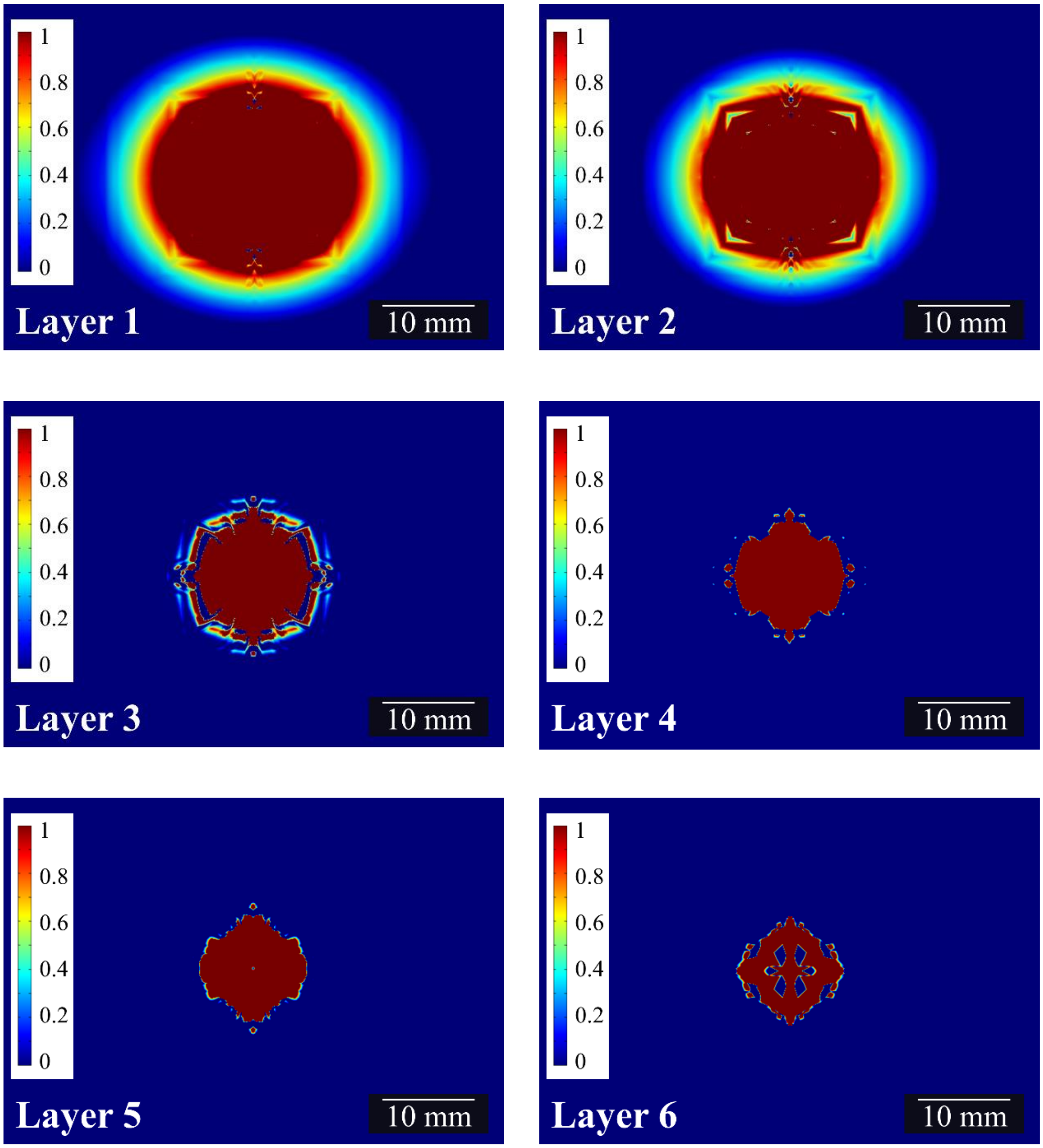

Figure 6-14. Predicted matrix decomposition damage in the underlying composite of a CFRP composite at 100 μs.

FFRP composite

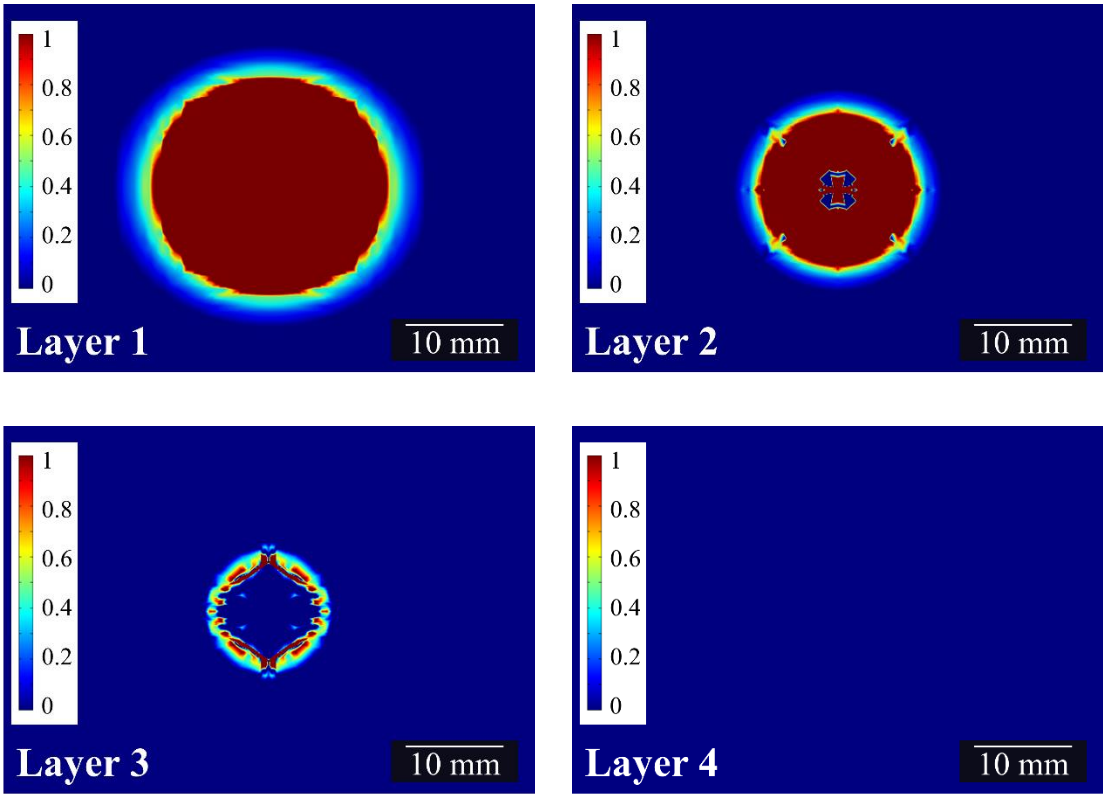

Figure 6-15. Predicted matrix decomposition damage in the underlying composite of an FFRP composite at 100 μs.

The thermal damage distribution of each interlayer in the CFRP composite and FFRP composite, excluding the FF layer, at 100 μs is shown in Figures. 6-14 and 6-15, respectively. When the simulated lightning strikes the center of the concentrated attachment point in the composites, Joule heating is generated, which initiates resin pyrolysis and carbon fiber sublimation in a circular distribution pattern. The damage then expands outward along the primary current conduction route in the carbon fiber direction. In the top six plies of the unprotected composite (Figure 6-14), the ablation damage is approximately 38 × 32, 33 × 29, 20 × 20, 15 × 15, 13 ×13, and 12 × 12 mm, respectively.

In the case of the FFRP composite, the predicted matrix decomposition size and intensity are lower than those of the unprotected composites in the same layer. Figure 6-15 shows that there is less thermal pyrolysis damage in the top three plies and no damage is observed in the fourth layer of the underlying CFRP composites. The damaged area in the top three underlying CFRP composites is approximately 32 × 28, 19 × 19, and 12 × 12 mm, respectively. The underlying carbon fiber/epoxy adjacent to the FF protection layer is possibly affected by higher heat transfer from the FF layer due to the higher maximum temperature. However, the FF layer could be ablated fast enough to reduce heat conduction due to increased electrical conductivity in the in-plane and thickness directions. Hence, the matrix decomposition in the top three interfaces of the underlying CFRP composites adjacent to the FF layer is about 24.90%. 62.59%, and 62.52% less than in the unprotected laminate, respectively. When lightning current is injected into the highly conductive LSP layer, the electrical current instantaneously conducts throughout the FF ply surface. Due to the increased electrical current, resistive heating induces a gradual temperature increase, which establishes localized heating effects. The mass-localized heat generation can cause extreme heat penetration of the thermal damage area and depth. The amount of electrical current decreases with depth while current penetrates to the underlying composite. Thus, the damage area and depth can be reduced by lower Joule heating. The effect of electrical conductivity enhancement is clearly a remarkable factor in the LSP system. The effective electric current distribution on the LSP surface mitigates heat transfer in the thickness direction and internal thermal damage development. Hence, the integration of a lightweight carbon-based LSP system (i.e., FF protection layer) in the outermost composite ply can substantially minimize thermal damage penetration in both the in-plane and out-of-plane directions and protect the underlying CFRP composite from high lightning current.

6.4. Summary

Lightning-induced damage of unprotected and FFRP composites was investigated by experimental and numerical analysis. A parametric study was performed to characterize the effect of electrical and thermal conductivities in the LSP layer that leads to thermal damage mitigation in the underlying CFRP composite. The electrical conductivity is the essential key in thermal damage development on the surface and through-thickness directions of the composite structure. However, the predicted thermal damage area slightly reduced with the increase of thermal conductivity in the in-plane and out-of-plane directions. Integrating the FF layer on the outermost layer of the CFRP composites significantly mitigated the matrix thermal damage region, especially in the thickness direction. This study clearly shows the importance of functional conductivities in the LSP layer that can successfully minimize matrix decomposition damage in the underlying composite. Thus, the carbon-based FF anti-lightning layer is an alternative to traditional metallic LSP systems.

CHAPTER 7

CONCLUSIONS AND FUTURE WORKS

7.1 Conclusions

The promising nanomaterials of CNTs and GNPs have excellent mechanical properties and electrical conductivities with high strength at least 100 times lighter than steel. In this study, several liquid precursors and catalysts were investigated to achieve the suitable shape and size of CNT. CNTs were successfully synthesized on the surfaces of Ni-coated woven carbon fibers at 550 °C using a floating catalyst-CVD process. The direct CNT growth on carbon fiber fabric served as a FF layer. This step was followed by the incorporation of GNPs onto FF, thereby offering the potential for significant electrical and mechanical property improvement. VARTM and wet lay-up techniques with autoclave curing were used to fabricate composite materials with the integration of a conductive LSP layer at the uppermost ply of the composite. It is evidently shown that composites fabricated by wet lay-up with autoclave curing provided higher mechanical and functional properties. The fuzzy fiber composites displayed increased electrical conductivity of around 120%, 400%, and 440% in the fiber, surface, and through-thickness directions, respectively. The improvement in surface direction is due to the formation of electrical percolation pathways in the intra- and interlaminar regions. It acts as a bridge offering faster electrons transportation through adjacent plies bridging the insulating gap between fibers in the uppermost ply. Moreover, the expanding number of electrical percolation pathways in the interlaminar regions can also improve electrical conductivity in the through-thickness direction. The thermal conductivity of the FFRP composite was also investigated by the laser flash method showing a relative improvement of 43% in the out-of-plane direction due to the enhancement of phonon transfer across adjacent fibers. The electrical conductivity was increased by more than 3 times in the fiber direction, 20 times in the surface direction, and 15 times in the thickness direction over reference laminates, due to the inclusion of GNPs at 0.2 wt%. However, no remarkable change of thermal conductivity in the fuzzy fiber with GNP integration.

The incorporation of GNPs into epoxy resin composites had also replenished porosities and voids fraction value in the epoxy matrix and enabled better chemical bonding formation. Hybrid GNPs-coated fuzzy fiber polymer composites had improved fillers-matrix interfacial interaction and strengthened polymer compact structural materials, resulted in remarkable compatibility and preferable stiffness of the matrix system due to the limitation of polymer motion of segmental chain and sufficient stress transfer. Therefore, the composite structures need much more energy to activate the segmental motion of chain mobility. Due to the high degree cross-linking structure and homogeneous dispersion, GNPs had the capacity to limit the motion of epoxy polymer molecular chain improving mechanical performances. Mechanical properties, including flexural, work of fracture, impact, and interlaminar shear stress properties were further enhanced. The integration of 0.1wt% GNPs onto fuzzy fiber composites provided better improvements in mechanical properties, including flexural strength (19%), work of fracture (32%), impact toughness (71%), and ILSS (45%) with high electrical conductivity. Results reveal that the simultaneous incorporation of GNPs and CNTs into composites offers an improvement in electrical conductivity without adversely affecting mechanical properties. These enhancements were much higher than those of reference composites, confirming that synergistic physical interactions can promote both efficient electron transport and load transfer by extending the crack propagation route. Therefore, the novel conductive carbon fiber proposed here could potentially minimize damage to composite materials and lead to more resilient materials.

A coupled thermal-electrical analysis model based on COMSOL was used to characterize thermal damage propagation modes in unprotected and FFRP composites induced by lightning strikes. The woven carbon fiber composite model was subjected to 20- and 40-kA peak currents with a 25/100 μs waveform. The matrix decomposition damage degree was defined in the normalized range between 0 and 1 or the temperature range of 300 °C (undamaged) to 500 °C (fully damaged). Lightning strike tests were conducted at 20 kA to characterize damage development. The predicted damage of the unprotected and FFRP numerical models was validated by the experimental post-lightning specimens by comparing the thermal damage size and appearance in the outermost surface to improve model accuracy. The characteristics of LSP systems were compared by enhancing electrical and thermal conductivities in either the in-plane or out-of-plane directions or both. The results indicate that electrical conductivity is the crucial parameter in mitigating lightning-induced thermal damage development on the surface and through-thickness directions. However, the enhancement of thermal conductivity in the in-plane and out-of-plane directions had a slight direct effect on the extent of the thermal damage area. Attaching FF ply on the surface of the CFRP composites drastically reduced delamination damage in the thickness direction and matrix pyrolysis damage region at the same ply compared with unprotected laminate. The top five interfaces were affected by thermal damage in the unprotected composite, whereas the FFRP limited the thermal damage to the three underlying CFRP plies adjacent to the FF ply. In the case of the damaged region in each surface layer, the size of the damage was around 38 × 32, 33 × 29, 20 × 20, 15 × 15, 13 ×13, and 12 × 12 mm in the top six plies of the unprotected composite, respectively. In the case of the FFRP composites, the size of the damage was 32 × 28, 19 × 19, and 12 × 12mm in the top three plies observed in the underlying CFRP composite. The size of the predicted matrix decomposition damage was lower than that of the unprotected composites in the same layer. This study presents evidence that the development of matrix decomposition damage in the underlying composite adjacent to the FF layer can be successfully reduced by integrating the LSP system. An FF layer, which is a highly conductive carbon-based structure to mitigate thermal damage of the underlying CFRP composite, serves as an effective lightweight anti-lightning strike structure for functional integration design.

7.2 Future works

1. Scalability of CNTs grown on carbon fiber using the floating catalyst-CVD method.

2. Considering other fabrication methods such as CNTs/Graphene 3D printing.

3. Lightning strike test (with different lightning current and waveforms) and EMI SE test will be tested on CFRP composites with different carbon-based LSP layers to understand the thermal response and shielding effectiveness with different LSP systems.

4. The mechanical test should be done on post-lightning damage samples to demonstrate and to compare the quality between the pre- and post-lightning damage samples.

5. A traditional C-scan technology was carried out for this study to examine the lightning-induced damage on the surface. It is suggested to use the latest CT-scan machine to increase the quality of the surface damage characterization and internal damage in the composite.

6. Improvement in the numerical analysis model can be done by implementing an internal expand pressure and acoustic shock effects.

REFERENCES

[1] Gouda P. S. S., Kulkarni R., Kurbet S. N., Jawali D. Effects of multi walled carbon nanotubes and graphene on the mechanical properties of hybrid polymer composites. Advanced Materials Letters. 2013;4(4):261-70.

[2] Pelin C., Ion D., Stefan A., Pelin G. Nanocomposites as advanced materials for aerospace industry. INCAS BULLETIN. 2012;4:57-72.

[3] Masuelli M. A. Introduction of fibre-reinforced polymers−polymers and composites: concepts, properties and processes. In: Masuelli M, editor. Fiber Reinforced Polymers - The Technology Applied for Concrete Repair. The Technology Applied for Concrete Repair: InTech; 2013.

[4] Mazumdar S. Composites Manufacturing. What will drive composites growth in 2015?: American Composites Manufacturers Association; 2015.

[5] ICIC Securities. Market Wrap. Lightweight composites: Vital cog in the CO2 emission reduction blueprint: ICICI Securities Ltd.; 2015. p. Proportion of composites in Airbus 350XWB and Boeing 787.

[6] Gardiner G. SAMPE Europe highlights: Composites face challenges in next commercial airframes. CompositesWorld: Composites Forecasts & Consulting LLC; 2014.

[7] Gibson R. F. A review of recent research on mechanics of multifunctional composite materials and structures. Composite Structures. 2010;92(12):2793-810.

[8] Katunin A., Krukiewicz K., Turczyn R., Sul P., Bilewicz M. Electrically conductive carbon fibre-reinforced composite for aircraft lightning strike protection. IOP Conference Series: Materials Science and Engineering. 2017;201(1):012008.

[9] Katunin A., Krukiewicz K., Turczyn R., Sul P., Łasica A., Catalanotti G., et al. Synthesis and testing of a conducting polymeric composite material for lightning strike protection applications. AIP Conference Proceedings. 2017;1809(1):020026.

[10] Katunin A. Lightning strike protection of aircraft composite structures: Analysis and comparative study. 2016;2016(8):49.

[11] Ebbesen T. W., Lezec H. J., Hiura H., Bennett J. W., Ghaemi H. F., Thio T. Electrical conductivity of individual carbon nanotubes. Nature. 1996;382(6586):54-6.

[12] S B., YK K., D. T. Unusually high thermal conductivity of carbon nanotubes. Phys Rev Lett 2000;84(20):4613-26.

[13] Cho J., Chen J. Y., Daniel I. M. Mechanical enhancement of carbon fiber/epoxy composites by graphite nanoplatelet reinforcement. Scripta Materialia. 2007;56(8):685-8.

[14] Wu H., Drzal L. T. Graphene nanoplatelet paper as a light-weight composite with excellent electrical and thermal conductivity and good gas barrier properties. Carbon. 2012;50(3):1135-45.

[15] Han J.-h., Zhang H., Chen M.-j., Wang D., Liu Q., Wu Q.-l., et al. The combination of carbon nanotube buckypaper and insulating adhesive for lightning strike protection of the carbon fiber/epoxy laminates. Carbon. 2015;94:101-13.

[16] Chu H., Xia Q., Zhang Z., Liu Y., Leng J. Sesame-cookie topography silver nanoparticles modified carbon nanotube paper for enhancing lightning strike protection. Carbon. 2019;143:204-14.

[17] Singh B. P., Choudhary V., Singh V. N., Mathur R. B. Growth of carbon nanotube filaments on carbon fiber cloth by catalytic chemical vapor deposition. Applied Nanoscience. 2014;4(8):997-1003.

[18] An Q., Rider A. N., Thostenson E. T. Electrophoretic deposition of carbon nanotubes onto carbon-fiber fabric for production of carbon/epoxy composites with improved mechanical properties. Carbon. 2012;50(11):4130-43.

[19] Du J.-H., Bai J., Cheng H.-M. The present status and key problems of carbon nanotube based polymer composites. Express Polymer Letters - EXPRESS POLYM LETT. 2007;1:253-73.

[20] Yamamoto N., Guzman de Villoria R., Wardle B. L. Electrical and thermal property enhancement of fiber-reinforced polymer laminate composites through controlled implementation of multi-walled carbon nanotubes. Composites Science and Technology. 2012;72(16):2009-15.

[21] Pozegic T. R., Hamerton I., Anguita J. V., Tang W., Ballocchi P., Jenkins P., et al. Low temperature growth of carbon nanotubes on carbon fibre to create a highly networked fuzzy fibre reinforced composite with superior electrical conductivity. Carbon. 2014;74:319-28.

[22] Radhakrishnan J. K., Pandian P. S., Padaki V. C., Bhusan H., Rao K. U. B., Xie J., et al. Growth of multiwalled carbon nanotube arrays by chemical vapour deposition over iron catalyst and the effect of growth parameters. Applied Surface Science. 2009;255(12):6325-34.

[23] Fang T.-H., Chang W.-J., Lu D.-M., Lien W.-C. Effects of gas composition on the growth of multi-walled carbon nanotube. Applied Surface Science. 2007;253(21):8749-53.

[24] Kunadian I., Andrews R., Pinar Mengüç M., Qian D. Multiwalled carbon nanotube deposition profiles within a CVD reactor: An experimental study. Chemical Engineering Science. 2009;64(7):1503-10.

[25] Qin W., Vautard F., Drzal L. T., Yu J. Mechanical and electrical properties of carbon fiber composites with incorporation of graphene nanoplatelets at the fiber–matrix interphase. Composites Part B: Engineering. 2015;69:335-41.

[26] De Greef N., Zhang L., Magrez A., Forró L., Locquet J.-P., Verpoest I., et al. Direct growth of carbon nanotubes on carbon fibers: Effect of the CVD parameters on the degradation of mechanical properties of carbon fibers. Diamond and Related Materials. 2015;51:39-48.

[27] Su C., Xue F., Li T., Xin Y., Wang M., Tang J., et al. Fabrication and multifunctional properties of polyimide based hierarchical composites with in situ grown carbon nanotubes. RSC Advances. 2017;7(47):29686-96.

[28] Pawlowski A. Can lightning bring down a plane? : CNN; 2010.

[29] Kuilla T., Bhadra S., Yao D., Kim N. H., Bose S., Lee J. H. Recent advances in graphene based polymer composites. Progress in Polymer Science. 2010;35(11):1350-75.

[30] Helmenstine A. M. Table of electrical resistivity and conductivity. Flow of Electric Current Through Materials: Thought Co.; 2017.

[31] Engineering Tool Box. Modulus of elasticity or Young's modulus - and tensile modulus for common materials. The Engineering Tool Box; 2016.

[32] Demczyka B. G., Wanga Y. M., Cumingsa J., Hetmana M., Hana W., Zettla A., et al. Direct mechanical measurement of the tensile strength and elastic modulus of multiwalled carbon nanotubes. ELSEVIER. 2002;334(1-2):173-8.

[33] Yu M.-F., Lourie O., Dyer M. J., Moloni K., Kelly T. F., Ruoff R. S. Strength and breaking mechanism of multiwalled carbon nanotubes under tensile load. Science. 2000;287(5453):637-40.

[34] Ma X., Scarpa F., Peng H.-X., Allegri G., Yuan J., Ciobanu R. Design of a hybrid carbon fibre/carbon nanotube composite for enhanced lightning strike resistance. Aerospace Science and Technology. 2015;47:367-77.

[35] Fuente J. d. L. Graphene. graphenea. 2015.

[36] DuPont. KEVLAR Aramid Fiber. 1992.

[37] Akovali G. Handbook of composite fabrication. Shawbury, United Kingdom: RARPA Technology LTD.; 2001.

[38] Golding W. L. Lightning strikes on commercial aircraft: How the airlines are coping. Journal of Aviation/Aerospace Education & Research. 2005;15(1):41-50.

[39] C. C. Goodloe. Lightning protection guidelines for aerospace vehicles George C. Marshall Space Hight Center: Marshall Space Flight Center, Alabama 35812. 1999. p. 1-37.

[40] SAE Report:AE4L-97-4, Aircraft lightning environment and related test waveforms standard. July 1997.

[41] MIL-STD-464C, Electromagnetic environmental effects requirements for systems department of defense interface standard. 2010.

[42] Wang Y., Zhupanska O. I. Lightning strike thermal damage model for glass fiber reinforced polymer matrix composites and its application to wind turbine blades. 2015.

[43] Cerra E. I. Lightweight copper/aluminum composites – Next generation conductors for the aerospace market. In: Proceedings of IWCS 2012, the 61th Annual International Cable & Connectivity Symposium. Conference, Conference 2012. p. 701-4.

[44] Islam M. S., Masoodi R., Rostami H. The effect of nanoparticles percentage on mechanical behavior of silica-epoxy nanocomposites. Journal of Nanoscience. 2013;2013 10.

[45] Palucka T., Bernadette B. V. Composites Overview. In: Hessenbruch A, editor. Second Generation (1960s): High performance composites in the post-Sputnik Era: Carbon and boron: History of recent science & technology. 2002.

[46] The Japan Carbon Fiber Manufacturers Association (JCMA), Materials. Type of carbon fiber products and their special features: Japan Chemical fibers association (FCFA). 2017.

[47] Performance composites, Carbon fiber composite design guide. Performance composites Inc. 2016.

[48] Matthews B. Composite materials analysis. General Dynamics2006. p. 1-40.

[49] Hull D., Clyne T. W. An introduction to composite materials (2nd edition): Cambridge Solid State Science Series. 2000.

[50] Baker A., Dutton S., Kelly D. Composite materials for aircraft structures (2nd edition). Virginia Polytechnic Institute and State University Blacksburg, Virginia: American Institute of Aeronautics and Astronautics. 2004.

[51] Abu Bakar I. A., Kramer O., Bordas S., Rabczuk T. Optimization of elastic properties and weaving patterns of woven composites. Composite Structures. 2013;100(Supplement C):575-91.

[52] Summerscales J. Composites design and manufacture. Reinforcement fabrics: Advanced Composites Manufacturing Centre. 2016.

[53] Lee S.-K., Byun J.-H., Hong S. H. Effect of fiber geometry on the elastic constants of the plain woven fabric reinforced aluminum matrix composites. Materials Science and Engineering: A. 2003;347(1):346-58.

[54] Gurit D. C. Woven fabrics. Net Composites Ltd. 2016.

[55] Ramsdale R. Composite molding processes. EngineersHandbook. 2006.

[56] Elkington M., Bloom D., Ward C., Chatzimichali A., Potter K. Hand layup: understanding the manual process. Advanced Manufacturing: Polymer & Composites Science. 2015;1(3):138-51.

[57] Berenberg B. Liquid composite molding achieves aerospace quality. High-Performance Composites: CompositesWorld. 2003.

[58] Core Molding Technologies, Resin transfer molding. Core Molding Technologies. 2016.

[59] Hoa S. V. Principles of the manufacturing of composite materials canada: DEStech Publications, Inc. 2009.

[60] Tan J. C., Cheetham A. K. Mechanical properties of hybrid inorganic-organic framework materials: establishing fundamental structure-property relationships. Chemical Society Reviews. 2011;40(2):1059-80.

[61] Kopeliovich D. Graphite. In: Kopeliovich D, editor. Graphite structure: substances & technologies. 2013.

[62] Hummers W. S., JR, Offeman R. E. Preparation of graphtitic oxide. Journal of the American Chemical Society. 1958;80(6):1339-.

[63] Castro N.A. G. F., Peres N. , Novoselov K., and Geim A. The electronic properties of graphene. Reviews of Modern Physics. 2009;81:109-62.

[64] Avouris P., Chen Z., Perebeinos V. Carbon-based electronics. Nature Nanotechnology. 2007;2:605.

[65] Lemme M. C. Current status of graphene transistors. Solid State Phenomena. 2010;156-158:499-509.

[66] Schulz M. J., Shanov V. N., Yin Z. Nanotube superfiber materials (1st Edition). UK: Elsevier. 2014.

[67] Dubois S., Zanolli Z., Declerck X., Charlier J.-C. Electronic properties and quantum transport in Graphene-based nanostructures. 2009.

[68] Geim A. K., Novoselov K. S. The rise of graphene. Nat Mater. 2007;6(3):183-91.

[69] Dreyer D. R., Park S., Bielawski C. W., Ruoff R. S. The chemistry of graphene oxide. Chemical Society Reviews. 2010;39(1):228-40.

[70] Kuila T., Bose S., Hog C. E., Uddin M. E., Khanra P., Kim N. H., et al. Preparation of functionalized graphene/ linear low density polyethylene composites by a solution mixing method. Carbon. 2011;49(3):1033-7.

[71] Kuila T., Bhadra S., Yao D., Kim N. H., Bose S., Lee J. H. Recent advances in graphene based polymer composites. Progress in Polymer Science. 2010;35(11):1350-75.

[72] Du J.-H., Cheng H.-M. The fabrication, properties, and uses of graphene/polymer composites. Macromolecular Chemistry and Physics. 2012;213(10-11):1060-77.

[73] Ganguli S., Roy, A.K. & Anderson, D.P. . Improved thermal conductivity for chemically functionalized exfoliated graphite/epoxy composites. Carbon. 2008;46(5):806-17.

[74] Yavari F., Rafiee M. A., Rafiee J., Yu Z. Z., Koratkar N. Dramatic increase in fatigue life in hierarchical graphene composites. ACS Applied Materials & Interfaces. 2010;2(10):2738-43.

[75] Ferreira Ávila A., Guimarães Zica de Oliveira Peixoto L., Silva Neto A., de Ávila Júnior J., Gabriela dos Reis Carvalho M. Bending investigation on carbon fiber/epoxy composites nano-modified by graphene. Journal of the Brazilian Society of Mechanical Sciences and Engineering. 2012;34(3):269-75.

[76] Baughman R. H., Zakhidov A. A., Heer W. A. d. Carbon nanotubes--The route toward applications. Science. 2002;297(787):787-92.

[77] Jorio A., Dresselhaus G., S Dresselhaus M. Carbon nanotubes: Advanced topics in the synthesis, structure, properties and applications: Springer. 2008.

[78] Zhang H., Wu B., Hu W., Liu Y. Separation and/or selective enrichment of single-walled carbon nanotubes based on their electronic properties. The Royal Society of Chemistry. 2011;40:1324-36.

[79] Rafiee R., Pourazizi R. Evaluating the influence of defects on the Young's modulus of carbon nanotubes using stochastic modeling. Materials Research. 2014;17(3):758-66

[80] Ando Y., Zhao X. Synthesis of carbon nanotubes by arc-discharge method. 2006.

[81] Journet C., Picher M., Jourdain V. Carbon nanotube synthesis: From large-scale production to atom-by-atom growth. 2012.

[82] AZO NANO. Carbon nanotubes, production methods for carbon nanotubes including arc discharge, laser, chemical vapor deposition and ball milling. Cheap Tubes Inc. 2006.

[83] Thompson D. Nanotechnology: Basic science and emerging technologies. Gold Bulletin. 2002;35(4):135-6.

[84] Chrzanowska J., Hoffman J., Małolepszy A., Mazurkiewicz M., Kowalewski T. A., Szymanski Z., et al. Synthesis of carbon nanotubes by the laser ablation method: Effect of laser wavelength. physica status solidi (b). 2015;252(8):1860-7.

[85] Kumar M. Carbon nanotube synthesis and growth mechanism. In: Yellampalli S, editor. Carbon Nanotubes - Synthesis, Characterization, Applications. Rijeka: InTech. 2011. p. Ch. 08.

[86] Azam M. A., Abdul Manaf N., Talib E., Bistamam M. S. A. Aligned carbon nanotube from catalytic chemical vapor deposition technique for energy storage device: A review. Ionics Springer Berlin Heidelberg. 2013. p. 1455-76.

[87] Lee C.-S., Hyun Y. Preparation and characterization of carbon nanofibers and its composites by chemical vapor deposition. In: Neralla S, editor. Chemical Vapor Deposition - Recent Advances and Applications in Optical, Solar Cells and Solid State Devices. Rijeka: InTech. 2016. p. Ch. 01.

[88] Seichepine F., Rothe J., Dudina A., Hierlemann A., Frey U. Dielectrophoresis-assisted integration of 1024 carbon nanotube sensors into a CMOS microsystem. advanced materials (Deerfield Beach, Fla). 2017;29(17).

[89] Rorro L., Schonenberger C. Physical properties of multiwall nanotubes. In: Dresselhaus MS, Smalley RE, Dresselhaus G, Avouris P, editors. Carbon Nanotubes: Synthesis, Structure, Properties, and Applications: Springer Berlin Heidelberg. 2001. p. 329-90.

[90] Schonenberger C. Electric properties of multiwall carbon nanotubes. In: Allegrini M, Garcia N, Marti O, editors. Nanometer Scale Science and Technology: IOS Press. 2001.

[91] Yamamoto T., Watanabe K., Hernandez E. R. Mechanical properites, thermal stability and heat transport in carbon nanotubes. In: Jorio A, Dresselhaus G, Dresselhaus MS, editors. Carbon Nanotubes: Advanced Topics in the Synthesis, Structure, Properties and Applications. Topics in Applied Physics: Springer Berlin Heidelberg. 2008. p. 165-94.

[92] Sparavigna A. C. Some notes on boltzmann and ladauer phonon thermal transport at nanoscale. International Journal of Sciences. 2014;3(12):24-7.

[93] Hepplestone S. P., Srivastava G. P. Low-temperature mean-free path of phonons in carbon nanotubes. Journal of Physics: Conference Series. 2007;92(1):012076.

[94] Maruyama S. A molecular dynamics simulation of heat conduction of a finite length single-walled carbon nanotube. Microscale Thermophysical Engineering. 2003;7(1):41-50.

[95] Pop E., Mann D., Wang Q., Goodson K., Dai H. Thermal conductance of an individual single-wall carbon nanotube above room temperature. Nano Letters. 2006;6(1):96-100.

[96] Rosa I. M. D., Sarasini F., Sarto M. S., Tamburrano A. EMC impact of advanced carbon fiber/carbon nanotube reinforced composites for next-generation aerospace applications. IEEE Transactions on Electromagnetic Compatibility. 2008;50(3):556-63.

[97] Gojny F. H., Wichmann M. H. G., Kopke U., Fiedler B., Schulte K. Carbon nanotube-reinforced epoxy-composites: enhanced stiffness and fracture toughness at low nanotube content. Composites Science and Technology. 2004;64(15):2363-71.

[98] Mingchao W., Cheng Y., Lin M. Graphene nanocomposites. In: Hu PN, editor. Composites and Their Properties: INTECH. 2012. p. 17-36.

[99] Laachachi A., Vivet A., Nouet G., Ben Doudou B., Poilâne C., Chen J., et al. A chemical method to graft carbon nanotubes onto a carbon fiber. Materials Letters. 2008;62(3):394-7.

[100] Islam M. S., Deng Y., Tong L., Faisal S. N., Roy A. K., Minett A. I., et al. Grafting carbon nanotubes directly onto carbon fibers for superior mechanical stability: Towards next generation aerospace composites and energy storage applications. Carbon. 2016;96:701-10.

[101] Wu Z., Meng L., Liu L., Jiang Z., Xing L., Jiang D., et al. Chemically grafting carbon nanotubes onto carbon fibers by poly(acryloyl chloride) for enhancing interfacial strength in carbon fiber/unsaturated polyester composites. Fibers and Polymers. 2014;15(3):659-63.

[102] Dey N. K., Hong E. M., Choi K. H., Kim Y. D., Lim J.-H., Lee K. H., et al. Growth of carbon nanotubes on carbon fiber by thermal CVD using ni nanoparticles as catalysts. Procedia Engineering. 2012;36:556-61.

[103] Mathur R. B., Chatterjee S., Singh B. P. Growth of carbon nanotubes on carbon fibre substrates to produce hybrid/phenolic composites with improved mechanical properties. Composites Science and Technology. 2008;68(7):1608-15.

[104] Sonoyama N., Ohshita M., Nijubu A., Nishikawa H., Yanase H., Hayashi J.-i., et al. Synthesis of carbon nanotubes on carbon fibers by means of two-step thermochemical vapor deposition. Carbon. 2006;44(9):1754-61.

[105] Thostenson E. T., Li W. Z., Wang D. Z., Ren Z. F., Chou T. W. Carbon nanotube/carbon fiber hybrid multiscale composites. Journal of Applied Physics. 2002;91(9):6034-7.

[106] Sharma S. P., Lakkad S. C. Effect of CNTs growth on carbon fibers on the tensile strength of CNTs grown carbon fiber-reinforced polymer matrix composites. Composites Part A: Applied Science and Manufacturing. 2011;42(1):8-15.

[107] Zhang Q., Liu J., Sager R., Dai L., Baur J. Hierarchical composites of carbon nanotubes on carbon fiber: Influence of growth condition on fiber tensile properties. Composites Science and Technology. 2009;69(5):594-601.

[108] Fujisawa K., Tojo T., Muramatsu H., Elías A. L., Vega-Díaz S. M., Tristán-López F., et al. Enhanced electrical conductivities of N-doped carbon nanotubes by controlled heat treatment. Nanoscale. 2011;3(10):4359-64.

[109] Laurent C., Flahaut E., Peigney A. The weight and density of carbon nanotubes versus the number of walls and diameter. Carbon. 2010;48(10):2994-6.

[110] Esconjauregui S., Xie R., Fouquet M., Cartwright R., Hardeman D., Yang J., et al. Measurement of area density of vertically aligned carbon nanotube forests by the weight-gain method. Journal of Applied Physics. 2013;113(14):144309.

[111] Pozegic T. R., Anguita J. V., Hamerton I., Jayawardena K. D. G. I., Chen J. S., Stolojan V., et al. Multi-Functional Carbon Fibre Composites using Carbon Nanotubes as an Alternative to Polymer Sizing. Scientific Reports. 2016;6:37334.

[112] Hu Z.-h., Dong S.-m., Hu J.-b., Wang Z., Lu B., Yang J.-s., et al. Synthesis of carbon nanotubes on carbon fibers by modified chemical vapor deposition. Carbon. 2013;52:624.

[113] Rong H., Han K., Li S., Tian Y., Muhuoyu. A novel method to graft carbon nanotube onto carbon fiber by the use of a binder. Journal of Applied Polymer Science. 2013;127(3):2033–7.

[114] Guo J., Lu C., An F. Effect of electrophoretically deposited carbon nanotubes on the interface of carbon fiber reinforced epoxy composite. Journal of Materials Science. 2012;47(6):2831-6.

[115] Al-Saleh M. H., Sundararaj U. A review of vapor grown carbon nanofiber/polymer conductive composites. Carbon. 2009;47(1):2-22.

[116] Choi J., Zhang Y. Single, double, multiwall carbon nanotube properties & applications. Aldrich Materials Science,Sigma-Aldrich Co LLC.

[117] Chang T. E., Kisliuk A., Rhodes S. M., Brittain W. J., Sokolov A. P. Conductivity and mechanical properties of well-dispersed single-wall carbon nanotube/polystyrene composite. Polymer. 2006;47(22):7740-6.

[118] Sandler J. K. W., Kirk J. E., Kinloch I. A., Shaffer M. S. P., Windle A. H. Ultra-low electrical percolation threshold in carbon-nanotube-epoxy composites. Polymer. 2003;44(19):5893-9.

[119] Thostenson E. T., Chou T.-W. Processing-structure-multi-functional property relationship in carbon nanotube/epoxy composites. Carbon. 2006;44(14):3022-9.

[120] Coelho P. H. d. S. L., Marchesin M. S., Morales A. R., Bartoli J. R. Electrical percolation, morphological and dispersion properties of MWCNT/PMMA nanocomposites. Materials Research. 2014;17:127-32.

[121] Marconnet A. M., Yamamoto N., Panzer M. A., Wardle B. L., Goodson K. E. Thermal conduction in aligned carbon nanotube–polymer nanocomposites with high packing density. ACS Nano. 2011;5(6):4818-25.

[122] Sun L., Warren G. L., O'Reilly J. Y., Everett W. N., Lee S. M., Davis D., et al. Mechanical properties of surface-functionalized SWCNT/epoxy composites. Carbon. 2008;46(2):320-8.

[123] Qian D., Dickey E. C., Andrews R., Rantell T. Load transfer and deformation mechanisms in carbon nanotube-polystyrene composites. Applied Physics Letters. 2000;76(20):2868-70.

[124] Hsieh T. H., Kinloch A. J., Taylor A. C., Kinloch I. A. The effect of carbon nanotubes on the fracture toughness and fatigue performance of a thermosetting epoxy polymer. Journal of Materials Science. 2011;46(23):7525.

[125] Sunil C. J., Vishwesh D. Enhancing interlaminar fracture characteristics of woven CFRP prepreg composites through CNT dispersion. Journal of Composite Materials. 2011;46(6):665-75.

[126] Gojny F. H., Wichmann M. H. G., Fiedler B., Schulte K. Influence of different carbon nanotubes on the mechanical properties of epoxy matrix composites – A comparative study. Composites Science and Technology. 2005;65(15):2300-13.

[127] Hernández-Pérez A., Avilés F., May-Pat A., Valadez-González A., Herrera-Franco P. J., Bartolo-Pérez P. Effective properties of multiwalled carbon nanotube/epoxy composites using two different tubes. Composites Science and Technology. 2008;68(6):1422-31.

[128] Tang L.-C., Wan Y.-J., Peng K., Pei Y.-B., Wu L.-B., Chen L.-M., et al. Fracture toughness and electrical conductivity of epoxy composites filled with carbon nanotubes and spherical particles. Composites Part A: Applied Science and Manufacturing. 2013;45(Supplement C):95-101.

[129] Bekyarova E., Thostenson E. T., Yu A., Kim H., Gao J., Tang J., et al. Multiscale carbon nanotube−carbon fiber reinforcement for advanced epoxy composites. Langmuir. 2007;23(7):3970-4.

[130] Kundalwal S. I., Ray M. C. Micromechanical analysis of fuzzy fiber reinforced composites. International Journal of Mechanics and Materials in Design. 2011;7(2):149-66.

[131] Garcia E. J., Wardle B. L., John Hart A., Yamamoto N. Fabrication and multifunctional properties of a hybrid laminate with aligned carbon nanotubes grown In Situ. Composites Science and Technology. 2008;68(9):2034-41.

[132] Yamamoto N., John Hart A., Garcia E. J., Wicks S. S., Duong H. M., Slocum A. H., et al. High-yield growth and morphology control of aligned carbon nanotubes on ceramic fibers for multifunctional enhancement of structural composites. Carbon. 2009;47(3):551-60.

[133] Boroujeni A. Y., Tehrani M., Nelson A. J., Al-Haik M. Hybrid carbon nanotube–carbon fiber composites with improved in-plane mechanical properties. Composites Part B: Engineering. 2014;66:475-83.

[134] Geng Y., Liu M. Y., Li J., Shi X. M., Kim J. K. Effects of surfactant treatment on mechanical and electrical properties of CNT/epoxy nanocomposites. Composites Part A: Applied Science and Manufacturing. 2008;39(12):1876-83.

[135] Veedu V. P., Cao A., Li X., Ma K., Soldano C., Kar S., et al. Multifunctional composites using reinforced laminae with carbon-nanotube forests. Nature Materials. 2006;5:457.

[136] H. C. Schniepp J.-L. L., M. J. McAllister, H. Sai, M. Herrera-Alonso, D. H. Adamson, R. K. Prud'homme, R. Car, D. A. Saville, I. A. Aksay. Functionalized single graphene sheets derived from splitting graphite oxide. the Journal of Physical Chemistry B. 2006;110:8535-9.

[137] Gudarzi M. M., Sharif F. Molecular level dispersion of graphene in polymer matrices using colloidal polymer and graphene. Journal of Colloid and Interface Science. 2012;366(1):44-50.

[138] Kruckenberg T. M., Hill V. A., Mazany A. M., Young E., Chiou S. Low density lightning strike protection for use in airplanes United States Rohr, Inc. 2015.

[139] ASTM D2344 / D2344M-16, Standard test method for short-beam strength of polymer matrix composite materials and their laminates. ASTM International, West Conshohocken, PA. 2016.

[140] ASTM D256-10, Standard Test Methods for Determining the Izod pendulum impact resistance of plastics. ASTM International, West Conshohocken, PA. 2018.

[141] Kobayashi T. Impact Testing. In: Buschow KHJ, Cahn RW, Flemings MC, Ilschner B, Kramer EJ, Mahajan S, et al., editors. Encyclopedia of materials: science and technology. Oxford: Elsevier. 2001. p. 4027-31.

[142] ASTM E1461-13, Standard test method for thermal diffusivity by the flash method. ASTM International, West Conshohocken, PA. 2013.

[143] Kim W.-S., Yun I.-H., Lee J.-J., Jung H.-T. Evaluation ofmechanical interlock effect on adhesion strength of polymer–metal interfaces using micro-patterned surface topography. International Journal of Adhesion & Adhesives. 2010;30(6):408-17.

[144] Noorhafanita N., Sahrim H. A., Chin H. C., Nay M. H. Mechanical and thermal properties of graphene oxide filled epoxy nanocomposites. Sains Malaysiana. 2014;43(4):603-9.

[145] Wen B., Cao M.-S., Hou Z.-L., Song W.-L., Zhang L., Lu M.-M., et al. Temperature dependent microwave attenuation behavior for carbon-nanotube/silica composites. Carbon. 2013;65:124-39.

[146] Gagné M., Therriault D. Lightning strike protection of composites. Progress in Aerospace Sciences. 2014;64:1-16.

[147] Im H. J., Jun G. H., Lee D. J., Ryu H. J., Hong S. H. Enhanced electromagnetic interference shielding behavior of graphene nanoplatelet/Ni/wax nanocomposites. Journal of Materials Chemistry C. 2017;5(26):6471-9.

[148] Wang X., Jiang Q., Xu W., Cai W., Inoue Y., Zhu Y. Effect of carbon nanotube length on thermal, electrical and mechanical properties of CNT/bismaleimide composites. Carbon. 2013;53:145-52.

[149] Sweers G., Birch B., Gokcen J. Lightning strikes: protection, inspection and repair. Aeromagazine. AERO: The Boeing Company. 2012. p. 19-28.

[150] Duongthipthewa A., Su Y., Zhou L. Carbon fibre composites with multi-nanofillers for lightning strike protection. In: Proceedings of The 21st International Conference on Composite Materials. Xi'an, China, Conference, Conference. 2017.

[151] Ogasawara T., Hirano Y., Yoshimura A. Coupled thermal–electrical analysis for carbon fiber/epoxy composites exposed to simulated lightning current. Composites Part A: Applied Science and Manufacturing. 2010;41(8):973-81.

[152] Muñoz R., Delgado S., González C., López-Romano B., Wang D.-Y., LLorca J. Modeling lightning impact thermo-mechanical damage on composite materials. Applied Composite Materials. 2014;21(1):149-64.

[153] Shulin L., Junjie Y., Xueling Y., Fei C., Xiaopeng S. Damage analysis for carbon fiber/epoxy composite exposed to simulated lightning current. Journal of Reinforced Plastics and Composites. 2016;35(15):1201-13.

[154] Yin J. J., Li S. L., Yao X. L., Chang F., Li L. K., Zhang X. H. Lightning strike ablation damage characteristic analysis for carbon fiber/epoxy composite laminate with fastener. Applied Composite Materials. 2016;23(4):821-37.

[155] Liu Z. Q., Yue Z. F., Wang F. S., Ji Y. Y. Combining analysis of coupled electrical-thermal and BLOW-OFF impulse effects on composite laminate induced by lightning strike. Applied Composite Materials. 2015;22(2):189-207.

[156] Katunin A., Krukiewicz K., Herega A., Catalanotti G. Concept of a conducting composite material for lightning strike protection. Advances in Materials Science. 2016;16(2):32.

[157] Lee J., Lacy Jr. T. E., Pittman Jr. C. U., Mazzola M. S. Thermal response of carbon fiber epoxy laminates with metallic and nonmetallic protection layers to simulated lightning currents. Polymer Composites. 2018;39(S4):E2149-E66.

[158] Khalil M., Abuelfoutouh N., Abdelal G., Murphy A. Numerical simulation of lightning strike direct effects on aircraft skin composite laminate international journal of architectural, Civil and Construction Sciences. 2018;12:173-86.

[159] Abdelal G., Murphy A. Nonlinear numerical modelling of lightning strike effect on composite panels with temperature dependent material properties. Composite Structures. 2014;109:268-78.

[160] Thostenson E. T., Ren Z., Chou T. W. Advances in the science and technology of carbon nanotubes and their composites: A review. Composites Science and Technology. 2001;61(13):1899-912.

[161] Chou T. W., Gao L., Thostenson E. T., Zhang Z., Byun J. H. An assessment of the science and technology of carbon nanotube-based fibers and composites. Composites Science and Technology. 2010;70(1):1-19.

[162] Qian H., Greenhalgh E. S., Shaffer M. S. P., Bismarck A. Carbon nanotube-based hierarchical composites: A review. Journal of Materials Chemistry. 2010;20(23):4751-62.

[163] Gantayat S., Prusty G., Rout D. R., Swain S. K. Expanded graphite as a filler for epoxy matrix composites to improve their thermal, mechanical and electrical properties. New Carbon Materials. 2015;30(5):432-7.

[164] Vadukumpully S., Paul J., Mahanta N., Valiyaveettil S. Flexible conductive graphene/poly(vinyl chloride) composite thin films with high mechanical strength and thermal stability. Carbon. 2011;49(1):198-205.

[165] Stankovich S., Dikin D. A., Dommett G. H. B., Kohlhaas K. M., Zimney E. J., Stach E. A., et al. Graphene-based composite materials. Nature. 2006;442(7100):282-6.

[166] Pal G., Kumar S. Multiscale modeling of effective electrical conductivity of short carbon fiber-carbon nanotube-polymer matrix hybrid composites. Materials & Design. 2016;89:129-36.

[167] Zhang H., Zhang G., Li J., Fan X., Jing Z., Li J., et al. Lightweight, multifunctional microcellular PMMA/Fe3O4@MWCNTs nanocomposite foams with efficient electromagnetic interference shielding. Composites Part A: Applied Science and Manufacturing. 2017;100:128-38.

[168] Soykasap O., Karakaya S., Colakoglu M. Simulation of lightning strike damage in carbon nanotube doped CFRP composites. Journal of Reinforced Plastics and Composites. 2015;35(6):504-15.

[169] Kumar V., Sharma S., Pathak A., Singh B. P., Dhakate S. R., Yokozeki T., et al. Interleaved MWCNT buckypaper between CFRP laminates to improve through-thickness electrical conductivity and reducing lightning strike damage. Composite Structures. 2019;210:581-9.

[170] Fu K., Ye L., Chang L., Yang C., Zhang Z. Modelling of lightning strike damage to CFRP composites with an advanced protection system. Part I: Thermal–electrical transition. Composite Structures. 2017;165:83-90.

[171] ASTM D7137 / D7137M-17, Standard test method for compressive residual strength properties of damaged polymer matrix composite plates. ASTM International, West Conshohocken, PA. 2017.

[172] SAE ARP 5412B, Aircraft lightning environment and related test waveforms. SAE International. 2013

[173] T300, Standard modulus carbon fiber. Toray Composite Materials America, Inc,: TORAY. 2018.

[174] Epoxy Resin ML-812A-LV. WAM safety data sheet: Wells Advanced Materials Co., Ltd. 2016.

[175] Hardener ML-812B-LV. WAM safety data sheet: Wells Advanced Materials Co., Ltd. 2016.

[176] Shoukai W., Deborah C. Electrical behavior of carbon fiber polymer-matrix composites in the through-thickness direction. Journal of Materials Science. 2000;35(1):91-100.

[177] Mirmira S., Jackson M., LS. F. Effective thermal conductivity and thermal contact conductance of graphite fiber composites. Journal of Thermophysics and Heat Transfer. 2001;15(1):18-26.

[178] Kundalwal S. I., Kumar R. S., Ray M. C. Effective thermal conductivity of a novel fuzzy fiber-reinforced composite containing wavy carbon nanotubes. Journal of Heat Transfer. 2015;137(012401).

[179] Pradere C., Batsale J. C., Goyhénèche J. M., Pailler R., Dilhaire S. Thermal properties of carbon fibers at very high temperature. Carbon. 2009;47(3):737-43.

[180] Pavlov T., Vlahovic L., Staicu D., Konings R. J. M., Wenman M. R., Uffelen P. V., et al. A new numerical method and modified apparatus for the simultaneous evaluation of thermo-physical properties above 1500K: A case study on isostatically pressed graphite. Thermochimica Acta. 2017;652:39-52.

[181] American Elements, Carbon nanotubes. The Advanced Materials Manufacturer.

[182] Raffray A. R., Najmabadi F., Tillack M. S., Wang X., Zaghloul M. Assessment of dry chamber wall configurations as preliminary step in defining key processes for chamber clearing code. University of California, San Diego. 2001.

[183] Oliveira V., Vilar R. Finite element simulation of pulsed laser ablation of titanium carbide. Applied Surface Science. 2007;253(19):7810-4.